IPP-Report

Max-Planck-Institut
für Plasmaphysik

Maya P. N.

Simulation Studies on Co-Deposited Hydrocarbon Films and Hydrogen Retention

IPP 17/23
2010

SIMULATION STUDIES ON CO-DEPOSITED HYDROCARBON FILMS AND HYDROGEN RETENTION

A THESIS SUBMITTED TO

DEVI AHILYA VISHWAVIDYALAYA, INDORE

for the award of the degree of

Doctor of Philosophy

in Physics

By

Maya P. N

April 2010

Institute for Plasma Research,
Bhat, Gandhinagar - 382 428,
Gujarat, INDIA.

PhD thesis entitled

SIMULATION STUDIES ON CO-DEPOSITED HYDROCARBON FILMS AND HYDROGEN RETENTION

Name of the student :	MAYA P. N
Submitted to :	Devi Ahilya Viswavidyalaya RNT Marg, Indore - 452001, Madhya Pradesh, India
Faculty :	Science
Subject :	Physics
Registration Date :	24-08-2006
Enrolment No. :	ISR/XI/Phy./07/444
Thesis Supervisor :	Dr. Shishir. P. Deshpande Associate Professor Institute for Plasma Research Bhat, Gandhinagar - 382 428 Gujarat, India
Thesis Co-Supervisor :	Dr. Brijesh Kumar School of Physics Vigyan Bhavan, Devi Ahilya Viswavidyalaya, Khandwa Road, Indore - 452001, Madhya Pradesh, India
Thesis Co-Supervisor :	Dr. Wolfgang Jacob Max-Planck Institute For Plasma Physics Boltzmann Strasse - 2, Garching, Germany - D 85748,
Thesis Co-Supervisor :	Dr. Udo von Toussaint Max-Planck Institute For Plasma Physics Boltzmann Strasse - 2, Garching, Germany - D 85748,
Place of Work :	Institute for Plasma Research Bhat, Gandhinagar - 382 428 Gujarat, India

Dedicated to

Achan and Amma

`for their encouragement, love and support`

Declaration

I hereby declare that the work presented in this thesis entitled **"SIMULATION STUDIES ON CO-DEPOSITED HYDROCARBON FILMS AND HYDROGEN RETENTION"** is original and has been done by me under the supervision of Dr. Shishir P Deshpande at Institute for Plasma Research, Bhat, Gandhinagar, 382428, India, approved by Research Degree Committee. I have worked for five years on the thesis with my supervisor.

I further declare that to the best of my knowledge the thesis does not contain any work which has been submitted for the award of any degree either in this University or any other University/Deemed University without prior citation.

....
(Signature of the Supervisor)
Dr. Shishir P Deshpande
Institute for Plasma Research,
Bhat, Gandhinagar - 382428,
Gujarat, India.

....
(Signature of the Candidate)
Maya P. N
Institute for Plasma Research,
Bhat, Gandhinagar - 382428,
Gujarat, India.

CERTIFICATE

This is to certify that the work entitled **"SIMULATION STUDIES ON CO-DEPOSITED HYDROCARBON FILMS AND HYDROGEN RETENTION"** is the original research work done by **Ms. Maya P. N.** under my (our) guidance and supervision for the award of the degree of **Doctor of Philosophy in Physics**, DEVI AHILYA VISWAVIDYALAYA, INDORE (M.P.), India. The candidate has worked for five years on her thesis. To the best of my (our) knowledge and belief the thesis:

1. embodies the work of the candidate herself;
2. has duly been completed;
3. fulfills the requirement of the Ordinance relating to the Ph.D. degree of the university;
4. is upto the standard both in respect of contents and language for being referred to the examiner.

....
(Sig. of Co-supervisor)
Prof. Brijesh Kumar
School of Physics
Devi Ahilya Vishwavidyalaya
Khandava Road, Indore,
M.P. India.

....
(Sig. of Co-supervisor)
Dr. W. Jacob
Max Planck Institute for
Plasma Physics,
Boltzmannstrasse 2,
Garching D-85741,Germany.

....
(Sig. of Co-supervisor)
Dr. Udo von Toussaint
Max Planck Institute for
Plasma Physics,
Boltzmannstrasse 2,
Garching D-85741,Germany.

....
(Sig. of Supervisor)
Dr. Shishir P Deshpande
Institute for Plasma Research
Bhat, Gandhinagar - 382428,
Gujarat,India.

....
(Forwarded by)
Prof. Ashutosh Mishra
Head, School of Physics
Devi Ahilya Vishwavidyalaya
Khandava Road, Indore,
M.P., India.

....
(Forwarded by)
Prof. P. K. Kaw
Director
Institute for Plasma Research
Bhat, Gandhinagar - 382428,
Gujarat, India.

Acknowledgments

From the course work days at IPR, Deshpande Sir inspired me to approach problems and tackle them in the true physical way, motivated me to approach him as my thesis supervisor. From zeroing down the topic for thesis work, I enjoyed complete freedom with him, to imagine, to think and to do fruitful research work. He has been a real teacher in the true sense and taught me the way to elucidate complex problems with simple models. I have, am sure checked his patience many times. Sir, thank you very much for the confidence you had in me which made me to complete this thesis. Sir, I take this opportunity to express my deepest gratitude for your wonderful guidance and all the values you have added in me, which made me a different person.

I would take this opportunity to express my heartfelt thanks to Prof. P.K. Kaw, the Director of our institute, for his belief in me and the support that I enjoyed from IPR throughout my tenure. I would like to express my thanks to DST-DAAD collaboration programme for the financial support for carrying out research at IPP Garching, Germany as a part of the thesis. I thank Max-Planck society for providing me the financial support for my extended stay in Germany.

I would like to express my gratitude to Dr. Manoj Warrier who has made his support available in a number of ways. The discussions with him were always valuable and they inspired me at various stages of the work.

Academic committee played a key role in shaping the thesis with yearly reviews and valuable suggestions from time to time. I express my sincere gratitude to the academic committee chairman Dr. R. Ganesh and the members of the committee Dr. Sudip Sengupta, Dr. Joydeep Ghosh and Dr. Prabal Chatopadhyay. I would like to thank the internal experts of my thesis Dr. R. Srinivasan and Dr. P.M. Raole for their suggestions at various stages of the work.

My sincere thanks to Dr. S. Mukherjee for teaching me the basics of experimental plasma physics and for being a constant support throughout the tenure. I would like to express my gratitude to all the faculty members who introduced the concepts of plasma physics and computational methods during the course work, Prof. Abhijit Sen, Prof. Amita Das, Prof. R. Singh, Dr. P. Vasu, Dr. D. Raju, Dr. Chenna Reddy, Prof. R. Jha, Dr. Nirmal Bisai, Dr. R. Srinivasan, Dr. Ajay Kumar and Dr. M. Kundu. I would like to thank Dr. V.P.

Anita and Dr. A.V. Ravi Kumar for their help and support during the period.

I thank Dr. Wolfgang Jacob for the valuable discussions and all other support during my stay at IPP, where I carried out part of my thesis work. I thank Dr. Udo von Toussaint for teaching me MD simulations and numerous data analysis techniques. The help and support from my colleagues at IPP made my stay an enjoyable experience. I thank Dr. Schwarz-Sellinger, Dr. Klaus Schmid and Thomas Dübeck for the useful discussions. I thank Christian Guggenberger and Silvio for helping me with the computer facilities from time to time. I would take this opportunity to thank Dr. Christian Hopf for all the support he has given during my stay at IPP as well as throughout my thesis. He has been a wonderful friend and the discussions with him helped in shaping the ideas at various stages of my learning curve. I take this opportunity to thank Prof. Kai Nordlund for providing the HCParCas code. I thank Dr. R. Schneider and Abha for the fruitful collaborative works. I would also like to thank Michael, Alessandro, Dilek, Sandeep, Shiva, Fabio, Smirnov, Vasile and Klaus for making my stay at IPP a wonderful experience.

This thesis would not have been possible without the help from a number of people from various sections of IPR. I am grateful to all of them for their valuable time and effort they have provided me. I thank Sutapa madam, Arvind, Hemant, Nilesh and Shailendra for helping me with computer facilities and Mrs. Pragnya Pathak, Mrs. A. Das, Ms. Smitha, Mr. Shravan and Mr. Saroj for supporting me with excellent library facilities. It is my pleasure to thank the Stores section for the material and equipment supports and administration for supporting in various ways and also for hostel facilities given during the thesis. My sincere thanks to accounts section for helping me out with account details during DST-DAAD collaborations and IPP Garching visits as well as for numerous other occasions.

My special thanks are reserved to Chandan, Shrishail and Swami for helping me out with TBM cluster and ITER-India workstations for performing massive computations towards the end of the thesis. I am grateful for Koshy, Anupama, Pintuda and Shiva for sending me research papers at any odd hour. I thank Christian, Sony, Sita, Deepak, Ashwin and Gayathri for the quick proof reading of the thesis. I would like to thank Anil, J.D. Patel, Nagendra and Mrs. A. Das from ITER-India for their timely assistance in presenting my thesis work in the final form.

The thesis could not have been such a memorable experience without the affection and support from my fellow scholars and friends at the hostel. The discussions and arguments *with them made the work a lot more enjoyable. My special thanks to all of you, Vikrant, Subhash, Kishor, Sunita, Sharad, Shekhar, Jugal, Satya, Sita, Deepak, Prabal, Kshitish, Ashwin, Ujjwal, Guru, Vikram, Sushil, Sanat, Pravesh, Ramu, Manjit, Sayak, Illias, Aditya, Soumen, Pintuda, Neeraj bhayya, Manasda, Rajneesh, Anand bhayya and Gayathri for all the fun we had together.*

Huge chunks of thanks to my friends Malu, Bhoomi, Prathibha, Linthish, Jinto, Sony, Praveen and Sijoy for their support and help throughout the thesis. Kishor, my special thanks for being with me since my college days.

My heartfelt thanks to Nita madam, Anand and Nayana for the homely and friendly atmosphere during the numerous extended interactive sessions with Sir. I thank madam for the care and support she offered throughout my work.

A single biggest credit of completing this thesis goes to my father and mother who have been a source of inspiration throughout my life. My father was always been supportive with his distinct ways and his belief in me continue to be the driving force and motivation. My heartfelt thanks to my mother for her immense support and patience during my long stays away from her. The thesis could not have been possible without the support of Kunchu ettan, Shailoppol, Krishnettan and Kutyedathy who always cared and supported me throughout the work.

Maya P.N.

Abstract

In this thesis we have modelled the fundamental processes leading to the growth and erosion of hydrocarbon films in the context of their hydrogen isotope retention in tokamaks. The process of erosion, re-deposition and subsequent erosion of the re-deposited material, combined with the transport in the gas phase leads to the formation of amorphous hydrocarbon films. The hydrocarbon radicals play a key role in this process. We have found that steric effects (mutual repulsion between H-atoms attached to neighboring carbon atoms) play a crucial role in deciding the structure and ultimately the retention.

First, we have investigated the re-erosion of a-C:H films due to the synergistic interaction of ions and thermal hydrogen. The ion-neutral synergism has been found to enhance the erosion yield as compared to a simple additive effect due to the physical sputtering (due to energetic ions) and the chemical erosion (due to thermal H atoms). The synergy is explained by the successive bond breaking due to energetic ions and passivation due to thermal H atoms. A new mechanism has been proposed based on this, namely, *Hydrogen Enhanced Physical Sputtering (HEPS)*, which explains the observed experimental results.

Second, we have studied the interaction of the methyl radicals (CH_3) with the hydrocarbon films. The sticking of CH_3 as a function of surface properties of the film (such as surface hydrogen content, number of dangling bonds *etc.*) are studied. The mechanism of sticking of thermal CH_3 radicals is found to be the direct incorporation at the dangling bond locations. The role of steric effects is also investigated and it has been found that the nearest neighbourhood strongly influences the sticking probability. The sticking probability is found to increase with the energy of the incident radicals.

The film growth has been modeled using a Monte Carlo code (Film Growth Monte Carlo, FGMC) with ballistic incorporation of methyl radicals. The shape and the orientation of the radicals have taken into account and the parameters such as porosity, roughness, H/C ratio and the structure of the film have been calculated. It has been found that, retention is the result of the synergistic interaction of atomic hydrogen and methyl rad-

icals. Atomic hydrogen creates the dangling bonds and methyl radicals get attached to those bond locations at which the steric repulsion is minimum.

The dynamics of hydrogen within the co-deposits has been carried out by a separate Kinetic Monte Carlo code. The dynamics of hydrogen within the film has been modelled as a sequence of adsorption-desorption processes which in turn depends on the migration energy of hydrogen. A method has been developed to calculate the migration energy, based on the potential energy surface analysis of the film. The migration energy distribution depends on the atomic arrangement of the film and shows considerable variation in the case of soft and intermediate density films. It has been found that the range of atomic hydrogen is limited to a few surface layers (~ 2 nm).

Finally, a multi-region multi-species analytical model has been developed for the growth of films with low H/C ratio. The model is based on the insights derived from MD and MC simulations and the idea that short polymeric chains grow, lock with each other and compactify. The reaction between various species has also incorporated in the model. It is interesting to note that, one can arrive at a more realistic (~ 1) H/C as observed in some of the tokamaks. The model brings out the importance of long-range steric effects in the structure formation. Constraints for achieving small H/C ratio is also brought out.

Publications in Refereed Journals

1. ***"Monte Carlo Modeling of Structure and Porosity of Codeposited Layers"*. P. N. Maya,** S. P. Deshpande and M. Warrier., *Contrib. Plasma Phys.* ***46,*** *No. 7-9, 757 – 762 (2006)*
2. *" **Dynamic Monte-Carlo Modeling of Hydrgen Diffusion in Codeposited Layers"***. A. Rai, **P. N. Maya**, R. Schneider, S. P. Deshpande and M. Warrier., *Journal of Nuclear Materials* ***363–365*** *, 1272–1276 (2007)*
3. ***"Synergistic Erosion Of Hydrocarbon Films: A Molecular Dynamics Study". P. N. Maya***, Udo von Toussaint and C. Hopf., *New Journal of Physics* ***10,*** *023002 (1-15) (2008)*
4. ***"Molecular Dynamics Modeling of Chemical Erosion of Hydrocarbon Films"***. Udo von Toussaint, **P. N. Maya** and C. Hopf*., Journal of Nuclear Materials,* ***386-388,*** *353--355(2009)*
5. ***"Hydrogen Enhanced Erosion of Amorphous Hydrocarbon Films"***. Udo von Toussaint, **P. N. Maya**, C. Hopf and M. Schleuter*., Physica Scripta,* ***T138,*** *014018 (1-4), (2009)*

Conference Presentations

International

1. **P.N. Maya,** S. P. Deshpande and Udo von Toussaint, *"Multiscale modeling of structure and porosity of hydrocarbon co-deposits"*, ***18th international conference on Plasma Surface Interactions in fusion devices (PSI-18),*** Toledo, Spain, 26-30 May 2008
2. Udo von Toussaint, **P. N. Maya** and C. Hopf, *"Chemical erosion of carbon films: A molecular dynamics study of synergistic co-bombardment effects"*, ***18th international conference on Plasma Surface Interactions in fusion devices (PSI-18),*** Toledo, Spain, 26-30 May 2008
3. **P. N. Maya**, "*Studies on the effect of ion bombardment in deciding the surface properties of amorphous hydrocarbon films*", ***8th Asia Pacific Theory Conference (APPTC)***, Gandhinagar, India, 11-13 December 2007
4. **P. N. Maya** and Udo von Toussaint, "*Molecular Dynamics study of the effect of low energy hydrogen bombardment on hydrocarbon co-deposits*", ***6th general assembly of Asia Plasma and Fusion Association (APFA)***, Gandhinagar, India, 3-5 December 2007
5. Udo von Toussaint and **P. N. Maya**, "*Molecular Dynamics modeling of chemical erosion of hydrocarbon films*", ***13th International Conference on Fusion Reactor Materials (ICFRM)***, Nice, France, 10-14 December 2007
6. **P. N. Maya** and Udo von Toussaint, "*MD simulation of erosion of hydrocarbon (a-C:H) layers due to low energy Ar bombardment*", ***11th international workshop on Plasma***

Facing Materials in Fusion Research (PFMC), Greifswald, Germany, 10-12 October 2006

National

1. **P. N. Maya,** Udo von Toussaint and S.P. Deshapane **"*Chemical Erosion of Carbon First Wall Structures*", *23trd Plasma Science and Society of India (PSSI) workshop*,** BARC, Mumbai**,** 10-13 December 2008
2. **P. N. Maya** and Udo von Toussaint, "*Molecular Dynamics modeling of the erosion of hydrocarbon films*", ***22nd Plasma Science and Society of India (PSSI) workshop***, Ahmedabad, India, 6-10 December 2007
3. **P. N. Maya** and S. P. Deshpande, "*On the role of atomic hydrogen in deciding the surface properties of plasma deposited hydrocarbon films*", ***22nd Plasma Science and Society of India (PSSI) workshop***, Ahmedabad, India, 6-10 December 2007
4. **P. N. Maya**, S. P. Deshpande and M. Warrier, "*Monte Carlo simulations of co-deposited hydrocarbon layers*", ***20th Plasma Science and Society of India (PSSI) workshop***, Cochin, India, 5-9 December 2005
5. **P.N. Maya**, S. P. Deshpande, M. Warrier and K. Nordlund, "*MD simulations of stereoscopic structure of sp2 and sp3 hybridization states in hydrocarbon films*", ***20th Plasma Science and Society of India (PSSI) workshop***, Cochin, India, 5-9 December 2005

Contents

List of Figures

List of Tables

Chapter 1

Introduction

The most promising way of achieving controlled thermonuclear fusion in the laboratory is by using the magnetic confinement scheme called a tokamak (Russian acronym for toroidal current and magnetic field). This is because the tokamaks have demonstrated very high energy confinement time compared to other schemes. In the past decade, there has been a dramatic improvement in the understanding the underlying physics of energy confinement and turbulence in tokamaks.

In a tokamak, hydrogen isotopes (deuterium and tritium) are used to create a hot and dense plasma so that the D–T fusion reactions take place (each reaction releases a neutron (14.1 MeV) and an α-particle (3.5 MeV)) [6]. Typically the required plasma temperature and densities are 20 KeV (232 million Kelvin) and 10^{20} m^{-3} respectively. In order to have an economically viable fusion reactor, the fusion power output must substantially exceed the externally injected input power. The condition for attaining this goal is given by Lawson criteria, which establishes the relationship between density, temperature and the energy confinement time [7]. A successful worldwide effort over the last fifty years has finally resulted in establishing an international partnership for building the ITER tokamak (International Thermonuclear Experimental Reactor) [8].

Basically, tokamak is like a magnetic bottle, where the fuel atoms are ionized to form ions and electrons. It has a toroidal geometry, with major radius 'R' and minor

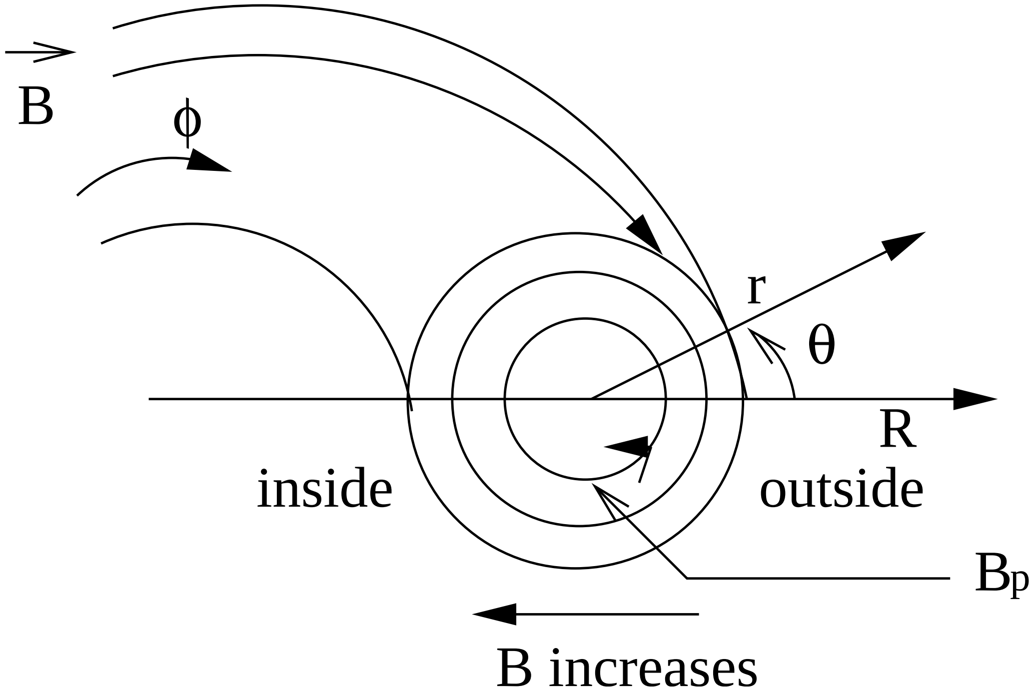

Figure 1.1: Schematic of typical tokamak cross-section with magnetic flux surfaces

radius 'a'. The magnetic field in the toroidal direction is generated by external coils. The plasma current in the toroidal direction generates the poloidal magnetic field. The net magnetic field is therefore, helical in shape. One can imagine the magnetic field lines to trace a 'magnetic surface' (a constant magnetic flux surface) which has a toroidal shape (see Fig. 1.1). Due to the strong magnetic field (typically a few Tesla), the Larmor radius of the particles is quite small ($\sim$ 3 mm for D^+ ions at 20 KeV, 3 T). Thus one can imagine that the particles stick to the magnetic field surfaces. As shown in the figure the surfaces are nested within each other and also represent constant-pressure surfaces. The innermost surface forms the hot central core of the tokamak [6].

The particles and heat from the core get transported across the magnetic surfaces until they reach the open surface called separatrix. In order to keep the central plasma hot and dense, particles and energy have to be replenished. Thus plasma fuelling and heating are crucial for achieving the desired confinement times.

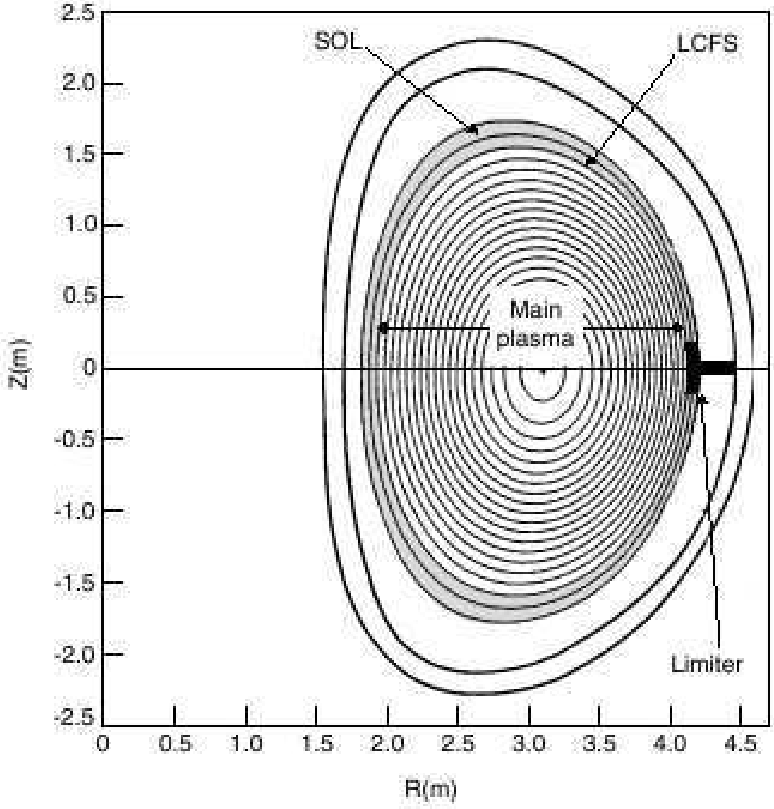

Figure 1.2: The schematic of poloidal cross-section of tokamak with limiter (JET) [1]

1.1 Tokamak Edge and Its Importance

In the core region, the magnetic field lines are closed upon themselves whereas in the edge region they are open. The surface separating the region of closed and open field lines is called the Last Closed Flux Surface (LCFS). In the region outside LCFS the plasma density and temperature have a sharp gradient in space, referred to as Scrape Off Layer (SOL). The plasma transport is dominant along the open field lines and this leads to its interaction with the Plasma-Facing Components (PFC). This results in various Plasma-Wall Interactions (PWI) [1,6].

In a tokamak, the wall components are protected from intense plasma interactions by material surfaces which tend to limit the size of the plasma. They are known as limiters. The typical tokamak plasma with limiter configuration is shown in Fig. 1.2 [1]. In the advanced tokamak configurations, the magnetic field lines are

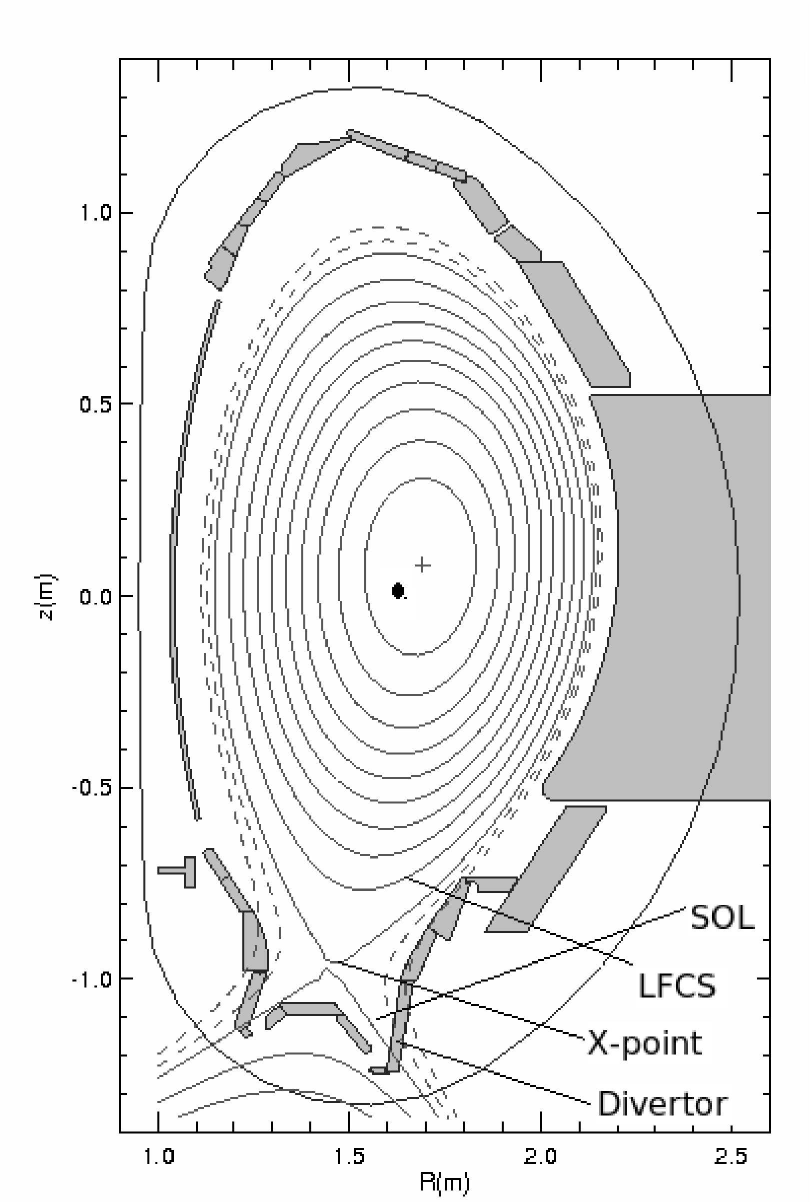

Figure 1.3: The schematic of poloidal cross-section with divertor (ASDEX). Cross represents the plasma center and the filled circle is the geometric center. The field lines are shown with plasma facing components

diverted with the help of additional current carrying coils (divertor coils) and the field lines intersect the material surfaces just outside the plasma boundary. Such configurations are known as divertors which allow operation with high heat-flux handling capability and much reduced impurities [1]. The schematic of a divertor plasma with the wall components is shown in Fig. 1.5. Thus, the intense plasma-wall interactions are focused to thin plasma-wetted areas on the limiter or divertor surfaces.

The interaction of the plasma with the wall materials results in their erosion and the eroded materials get partly pumped off and partly transported back into the plasma. The impurity atoms also get ionized but are not completely stripped off electrons. The bound electrons associated with the low energy ions present in the relatively cool edge-plasma cause energy loss through impurity line radiation. This results in the formation of a radiative layer in the edge and plays a crucial role in the energy balance of the core plasma. The studies on edge physics demonstrated that the edge plasma has a critical role in deciding the global confinement and stability of the tokamak. The studies on the stability of the edge plasma have revealed a picture of various instabilities and how they are connected to confinement, transport and disruptions (see for example, the studies on H-mode [1, 9], Edge Localized Modes (ELMs) [10] and the radiative instabilities such as MARFE *etc.* [11–13]).

The study of PWI was focused mainly to the impurity transport and the edge related phenomena for a long time. However, with the advent of steady state tokamaks, another issue which attracted immense attention is the erosion of the divertor-target material [14–16]. This affects the overall availability of the reactor. One of the most commonly used plasma facing component is carbon (graphite and carbon fiber composites) due to its high thermal shock resistance and low radiation losses due to low atomic number [14]. However, the interaction of the hydrogen plasma with the carbon based wall-materials cause their erosion. In the subsequent sections, we shall discuss the important plasma-wall interactions.

1.2 Plasma-Wall Interactions

The interaction of energetic ions from the plasma with the materials results in various momentum transfer processes via collision cascades, where the incident atom transfers its momentum to the target atoms. At the end of the cascade, the incident atoms get thermalized and can stay within the material in thermal equilibrium. This process is known as *implantation*. The energized, collided atoms can come out of the material resulting in various erosion processes [17]. Depending on the mechanisms, they are classified into *(a) physical sputtering, (b) chemical sputtering and (c) chemical erosion* [17–20].

Physical Sputtering is an elastic collision process, in which the momentum of the incident atom is either directly transferred to the sputtered atom or by indirect means, *i.e.*, by creating a primary knock-on atom followed by a collision cascade. Chemical erosion is defined as the process where the interaction between thermal species from gas phase interact with the surface atoms. This is one of the important mechanism of erosion of carbon materials by atomic hydrogen. Chemical sputtering is a process in which both momentum transfer and chemical effects together cause the erosion of the material.

Apart from affecting the lifetime of the wall, the hydrogen atoms diffuse into the bulk of the carbon (Graphite as well as CFC) material. This cause the retention of fuel isotopes in the bulk [5, 21–23].

The erosion of carbon PFC leads to a very important issue known as co-deposition which has a crucial role in the fuel retention and inventory [14, 24, 25]. The eroded materials along with the fuel isotopes deposit on the inner surfaces of the tokamak over several plasma shots. This is known as **hydrocarbon co-deposition** [14]. The co-deposits can retain fuel isotopes causing the issue of fuel retention and eventually add to the total fuel inventory [26]. Once, tritium is used as the fuel, it has serious implications regarding the continuous operation of the machine, due to the radioactivity of tritium and an upper limit on the maximum allowable fuel inventory. For example, the references [27] says about 350 gm of total fuel inventory in

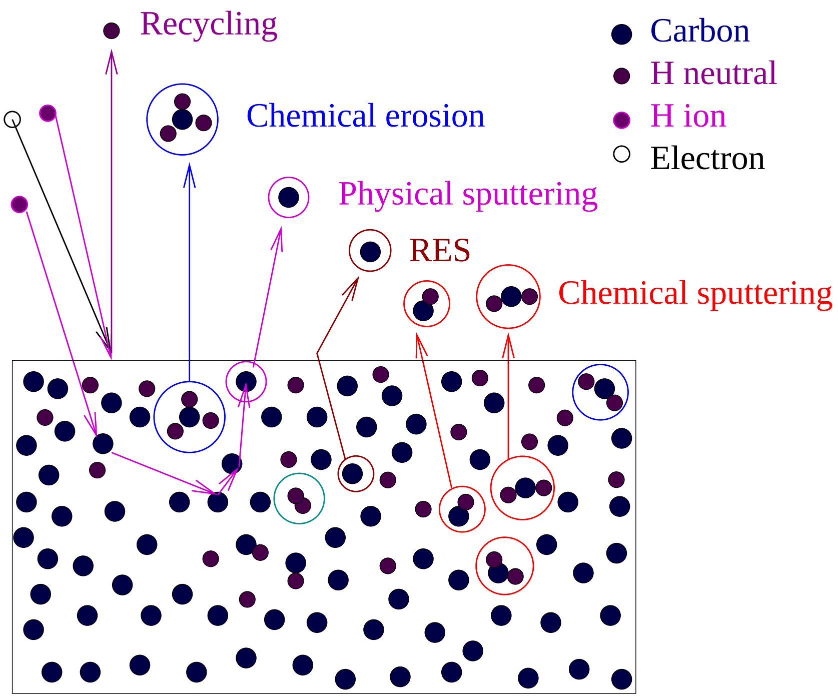

Figure 1.4: The schematic of various plasma-wall interaction processes

ITER, which means, after crossing this limit, the machine needs to be shutdown and de-tritiated for further operation.

1.2.1 Observations on Tokamak Co-deposition

Most of the tokamaks have reported co-deposition and their fuel retention [2, 3, 25, 28–42]. The typical cross-section of divertor is shown in Fig. 1.5. The regions where the plasma interacts directly with the wall components are called 'plasma-exposed' regions and the regions are shadowed from direct plasma contact are called 'plasma-shadowed' regions. The plasma-exposed regions include the divertor strike points and other divertor areas whereas regions such as pump ducts, baffle plates *etc.* are the plasma-shadowed regions. Co-deposition is observed in both plasma-exposed and plasma-shadowed regions.

The deposits formed in the plasma-exposed regions are termed as 'hard' and have been characterized by their hydrogen content, as 'H/C ratio' [2, 32]. This represents how many hydrogens per carbon exist in the deposits. For hard films this ratio is

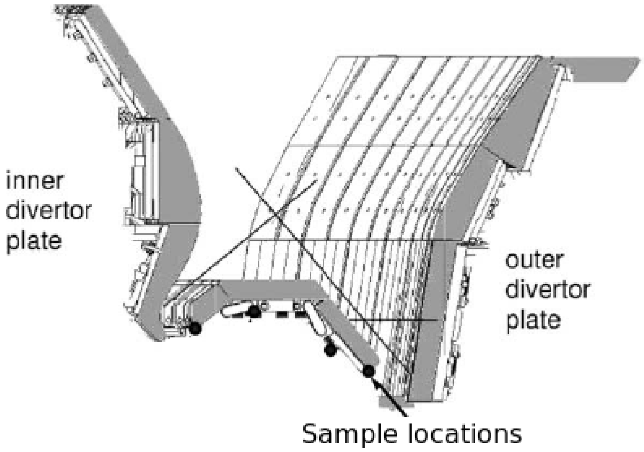

Figure 1.5: Divertor of ASDEX Upgrade tokamak. The filled circles indicate the locations where the samples were placed to study the deposition [2]

typically less than 0.4. The films formed in the plasma-shadowed regions are called 'soft' and porous and having H/C ratio more than 0.4 and reported values goes upto 1.4 [2, 43, 44]. The thickness of these films were upto several microns (μm) and the locations of their formation vary with tokamaks. The rate of growth of these films also varies with tokamak and the locations where the films have formed. The table (1.1) summarizes the observations in various tokamaks.

Table 1.1: The table of observations from various tokamaks (referred above). The exposure time of the tile varies with tokamaks

Tokamak	H/C ratio	Character	Locations	Thickness (μm)
JET	0.75–1.5	Soft	Inner Divertor Louvre	100
ASDEX	0.3, 1.4	Hard, Soft	Sub-divertor Pump ducts	20-40
TORE SUPRA	0.1	Hard	Toroidal Pump Limiter, Neutralizer	$\sim$ 200
JT-60U	0.1,0.85	Hard, Soft	Outer dome, Pump ducts	upto 100
TEXTOR	0.4	Hard	Gap between tiles	upto 70
DIII-D	0.3-0.5	Hard,Soft	Inner Divertor	20-30

A typical picture of co-deposits observed in TORESUPRA tokamak is shown in

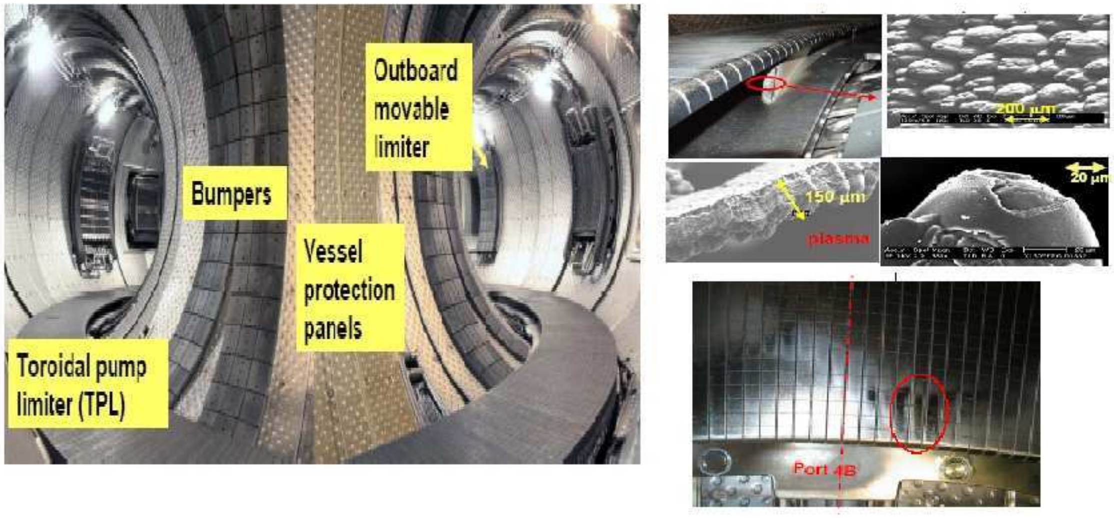

Figure 1.6: The co-deposits observed in Tore Supra tokamak along with the cross-section of the tokamak [3]. The deposits were located in the toroidal pump limiter and the neutralizer plates.

Fig. 1.6 [3]. From the analysis of co-deposition on various tokamak observations, following can be summarized:

1. Hydrocarbon co-deposits are amorphous hydrocarbon (a-C:H) films
2. The properties of these films vary with tokamaks
3. The structure, thickness and the hydrogen content vary with locations inside the tokamak
4. Retention depends on the structure of the film. Soft films found to retain large quantities of fuel (H/C ratio upto 1.4) compared to hard films (H/C ≤ 0.4)
5. The films are formed in the plasma-shadowed regions are found to be soft whereas the films formed in the plasma exposed regions are hard.

1.2.2 Status of Understanding

The process of erosion of the plasma-facing materials is the origin to understand the co-deposition. Because, it is this material which gets mixed up with the fuel isotopes and get transported to the plasma-shadowed remote regions of the tokamak. Thus, a slow and steady growth of amorphous hydrocarbon (a-C:H) films is possible in such regions. Such regions are typically *pump ducts, baffle plates etc.*, and play an important role in quantifying the total fuel inventory. The understanding of co-deposition involves quantification of different physical processes. They are: (a) erosion of the plasma facing materials, (b) transport of the eroded materials through the SOL plasma and (c) deposition of the transported material. Each of these area is vast and extensive studies were done in the past [20, 45–51]. In the subsequent sections we review the status of understanding of various related fields.

1.2.2.1 Erosion Studies

The erosion of the plasma facing components is of extreme importance not only for co-deposition but also regarding the life time of the tokamak wall. There have been numerous studies to understand the various processes of erosion of the wall material. Depending on the process involved in the erosion of the wall material, these processes are classified into (a) physical sputtering, (b) chemical sputtering and (c) chemical erosion.

1.2.2.1.1 Physical Sputtering Physical Sputtering is an elastic collision process, in which the momentum of the incident atom is either directly transferred to the sputtered atom or by indirect means, i.e., by creating a primary knock-on atom followed by a collision cascade. The sputtered particles originate within first few atomic layers, and the sputtering process occurs within a few picoseconds' time. There exists an energy threshold for this process and the kinetic energy distribution of the emitted particles is well above thermal energies. Physical sputtering is comparatively well understood and pioneered by W. Eckstein and R. Behrisch [17,33,52–54].

Another recently described erosion mechanism, termed *swift chemical sputtering*, has been identified by *Salonen et.al.*using molecular dynamics simulations [55]. In this process, incident ions with energies down to about 2 eV cause the kinetic emission of hydrocarbon radicals from a-C:H films. The process has been reported for both hydrogen and helium ions [56, 57] and is therefore considered by some as a special case of physical sputtering [58].

1.2.2.1.2 Chemical Erosion Chemical erosion is defined as the process where the interaction between thermal species from gas phase interact with the surface atoms. This is one of the important mechanism of erosion of carbon materials by atomic hydrogen. Chemical erosion of carbon by hydrogen is a thermally driven process which does not require any energetic species and has been studied using thermal hydrogen atom beams [19]. An incident hydrogen atom creates a radical site by abstracting a bound hydrogen from the surface. The radical site relaxes via the emission of a neighboring CH_3 radical. The molecule ejection is a thermally activated process with an energy barrier of 1.6 eV. Therefore, it happens only at higher surface temperatures.

1.2.2.1.3 Chemical Sputtering Winters and Coburn describes chemical sputtering as *"a process where ion bombardment causes or allows a chemical reaction to occur which produces a particle that is weakly bound to the surface and hence easily desorbed into the gas phase"*. However, no single definition of chemical sputtering exists in the literature. In a review article Jacob *et. al.*, give an overall picture of chemical sputtering, where they describe the erosion process depends on the momentum transfer and chemical reactivity of the impinging particles as chemical sputtering. In that article, the observations and features of chemical sputtering has been described as follows:

- The eroded particles are molecules formed out of different target and incident atomic combinations
- The sputtering yield is significantly higher than pure physical sputtering
- The threshold of erosion is much lower, which means the sputtering can be observed at lower incident energies
- The sputtering yield shows a pronounced temperature dependence

- The energy distribution of the released species are close to that of the target surface temperature

Fig. (1.4) shows the schematic of various erosion process happening on the surface and bulk of the plasma facing components.

1.2.2.2 Hydrocarbon Transport in the Plasma

The eroded material gets transported through the plasma, and there have been studies to understand the transport of carbon atoms and radicals through the plasma. In order to understand the transport of hydrocarbons in the tokamak, $^{13}CH_4$ experiments were conducted in TEXTOR, JET and DIII-D [31,45,47,49,51]. The $^{13}CH_4$ molecules were injected into the SOL and divertor regions of these tokamaks and the deposition profiles were analyzed using surface characterization techniques. The experiments in DIII-D showed that the highest concentration of ^{13}C was observed in the divertor in both L mode (Low confinement mode) and H mode (High confinement mode) discharges. DIII-D results during L mode show an abundance in carbon deposition in the inner divertor region which was operating in the detached divertor conditions. During the elmy H mode discharge, there observed huge deposition in the private flux region. In order to model the observed profile, onion-skin model was used. However, these models could predict only half of the deposited particles [31,49].

The experiments on JET and TEXTOR suggested that, a part of the carbon was transported over short distances and got directly re-deposited [45,47,51]. The long range carbon transport depends crucially on the plasma parameters and showed considerable difference in JET and TEXTOR tokamak. These studies showed that the carbon transport and re-deposition not only depend on the plasma parameters but also have sensitive dependence on the factors such as magnetic ripple and shape and orientation of the wall components *etc.* In JET, the long range transport was observed and which could be the reason for the abundant carbon deposition observed in the pump ducts and louvre. The sticking was modelled by assuming a sticking coefficient for the radicals. Whereas in TEXTOR, most of the carbon deposition were observed in the hot neutralizer plates in the form of hard a-C:H layers. This was modelled using Monte Carlo codes like ERO-TEXTOR and ERO-JET and in TEXTOR, most of the $^{13}CH_4$ were transported inside the Last Closed Flux Surface (LCFS) where it gets completely dissociated and get deposited on the neutralizer plates. The deposition efficiency of ions were much higher than that of neutral CH_3.

The observed hydrocarbon profile in the JET louvre and pump ducts of TEXTOR suggest the need of re-erosion of hydrocarbon films by the background plasma. For JET, the low T_e range (2–5 eV) in the inner divertor might have enhanced the formation of soft and polymer like films. These films get eroded by the background plasma due to synergistic effects by background hydrogen ions as discussed in Section (1.2.2.1). This results in the release of hydrocarbons into the plasma. Thus the eroded particles undergo sticking and further re-erosion and finally reaches the remote regions. Also, the low sticking radicals such as CH_3 can undergo relatively long range transport and also reaches the remote locations. However, the mechanisms of re-erosion of hydrocarbon films by background plasma is not clear.

1.2.2.3 Growth

The modeling of the deposition profiles in tokamaks were done by assuming a sticking coefficient of the radicals or atoms on the surface. However, the deposition of a-C:H films is more complicated than assuming a sticking coefficient as the growth is a result of various surface reactions happening on the surface. Hence the plasma-boundary conditions influence the growth of these films. These studies have however not addressed from a tokamak context.

The film growth is a non-equilibrium process and therefore, addressed by non-equilibrium models for growth in non-linear systems [59]. One of the oldest and widely used model for film growth is the ballistic deposition where the lattice is binned into unit sized bins and the incoming particles stuck upon the first contact they have with the surface. This model successfully explained the observed surface roughness of the films grown under vapour deposition [60]. The ballistic deposition shows correlation between different sites on the surface and this results in the saturation of the surface roughness which was measured in various experiments. The standard ballistic model considers spherical particles incident normal to the surface and the analytical solution of such a system is possible in 1D, leads to a class of scalings known as KPZ (Kardar-Parisi-Zhang) universality [59, 61, 62]. Another widely used surface growth model is Diffusion Limited Aggregation (DLA), where the incoming particle perform surface diffusion and aggregates themselves to form structures [63]. The roughness scalings observed in the growth of a-C:H layers reported consistent scalings with ballistic deposition. However, such models cannot simulate the growth from chemically interacting species having definite molecular structures such as methyl radicals.

From the plasma processing point of view hydrocarbon films are routinely deposited by Chemical Vapour Deposition (CVD). These studies mainly focused on the formation of hard films since their excellent mechanical properties and chemical inertness make them as protective coatings. These class of films are generally known as Diamond Like Carbon (DLC) films due to their high hardness and low hydrogen content. These experiments have shown that methyl radicals are the most abundant species present in the plasma formed in methane discharges. The correlation between different plasma parameters and the structure (hardness, hydrogen content and hybridization ratio) of the coatings formed were also investigated in such studies [64–69].

In order to gain more insight into the plasma-surface boundary phenomena, radical beam experiments were performed using CH_3 radicals and H atoms [70–73]. These experiments showed that the sticking of methyl radicals could be enhanced upto two orders of magnitude ($\sim 10^{-2}$) by the addition of thermal hydrogen. The film growth model takes into account the CH_3 sticking at the dangling bonds created by atomic hydrogen. Ion bombardment also creates dangling bonds within its range which act as the sites for CH_3 adsorption [74–77]. Rate equation models for the surface coverage of dangling bonds have been proposed based on this and by using the measured sticking coefficients, the sticking cross-sections of the radicals have been calculated [77]. However, these models are derived based on the macroscopic properties of the films at the steady-state conditions. Therefore, the detailed microscopic understanding of the surface mechanisms is missing in these models.

The microscopic mechanism of sticking of methyl radicals on hydrocarbon surfaces was investigated by computer simulations as well. The ion-induced chemisorption of CH_3 radicals was addressed by various authors by using different computational techniques. The ion-induced dangling bond generation is modelled by TRIM.SP calculations and the CH_3 radicals are assumed to be adsorbed on these locations. The latter was modelled by rate equations. Various types of Monte Carlo techniques were used to study the growth of DLC films in presence of atomic hydrogen and energetic CH_3 ions. These simulations proposed various reaction pathways for the incorporation of CH_3 radical to the lattice depending on the energetics. However, these models lack the microscopic nature of interpretation of the growth.

The ion-induced growth of a-C:H layers was simulated by *Miyagawa et.al.*, [78] in presence of CH_3^+ ions and CH_3 radicals using Dynamic Monte Carlo simulations and showed that sp^3 bonding in the subsurface is based on subplantation model proposed by *Robertson* [79]. The growth of diamond like films using methyl radicals and atomic hydrogen was simulated by *Battile et.al.*, using a set of parametrized surface reaction rates [80]. The growth rates and hydrogen concentration of the film were computed as a function of surface temperature. Time dependent MC simulations were also performed by *Dawnkaski et.al.,* for determining the effect of a variety of H and H_2 induced surface reactions on diamond surfaces [81, 82]. The reactions include H abstraction, H_2 desorption, H diffusion and the reverse of these reactions. These simulations proposed an alternate pathway for the CH_2 incorporation into the diamond lattice by the incorporation of a CH_3 radical at a π-bond location and the migration of one of the hydrogens into the dangling bond followed by a dimer opening step [83].

All the above models consider growth in the presence of energetic ions.

The detailed atomistic mechanism of sticking of methyl radicals on hydrocarbon surfaces were studied using Molecular Dynamics simulations. The reflection coefficient of hydrocarbon radicals (CH_2,CH_3 and CH_4) on hydrogenated carbon surfaces was studied for different incident energies and angles under edge plasma relevant conditions [84, 85]. It was found that the reflection coefficient of the radicals were sensitive to the hydrogen content of the radicals and it reduces with incident energy. The reaction mechanisms of hydrocarbon radicals on a-C:H films were studied by *Neyts* in the case of an expanding thermal plasma using MD simulations for higher hydrocarbons such as C_2, C_3 and cyclic and linear C_3H combinations [86–88]. The sticking coefficients were estimated as a function of the internal energy of the radical and the angle of incidence on various dangling bond locations with and without H flux [89]. MD simulations of CH_3 radicals on reconstructed diamond surfaces were performed by *Alfonso et. al.*, using Brenner potential for energies up to 1 eV with different angles of incidence [90]. They have found that the sticking coefficient increases with incident energy and decreases with angle of incidence. They also showed that the sticking coefficient reduces with surface hydrogen content. However, these studies did not address the local neighbourhood of the sticking sites.

The chemisorption of methyl radicals on specific dangling bond locations were studied by *Träskelin et.al.*, on the diamond surface using both classical MD (using Brenner potential) and tight binding approach. The sticking coefficient was estimated for four different types of surfaces having different dangling bond configurations and at various angles of incidence [91, 92]. They have found that in the case of isolated dangling bond the calculations using tight binding approach are in good agreement with the predictions of rate equation models.

In the case of amorphous surfaces, there exists a variety of neighbourhoods and the dangling bond distributions. The sticking coefficient and cross-sections on isolated dangling bonds is different than that on an amorphous surface.

1.3 Motivation

From the previous section, we can conclude that there is not enough information on the soft films (growth mechanisms, erosion *etc.*) which infact contributes strongly to the retention due to their high H/C ratio. It is also clear that there is no model to account for the real mechanism of growth, namely the incorporation of radicals in the regions not exposed directly to the plasma. One of the most important effects that naturally arises in the growth of soft films is the so-called **steric effect**, arising from the mutual repulsion between H atoms bonded to different carbon atoms. The effect of the steric repulsion in the growth is not addressed in any of the previous studies.

The erosion, the growth and the retention processes involve disparate time and space scales (from femto-seconds to several hours in time and from molecular dimensions to a few meters in space). This makes the study of retention a grand challenge multi-scale problem. In order to build such a model in future, the physics in the different scales needs to be linked carefully. In this thesis, we limit ourselves to the study of fundamental processes that lead to the formation of co-deposits, their erosion and the retention of hydrogen isotopes in them. In this context, the key questions we would like to answer are as follows:

1. What is the role of synergism of thermal and energetic species from the plasma in the erosion of co-deposited layers formed in the plasma-exposed regions?
2. What are the key processes of the co-deposition of the eroded particles under conditions relevant to the remote areas of the tokamak?
3. What is the role of steric effect in the growth of soft hydrocarbon films?
4. How do these processes influence the growth and the structure of the film?
5. How does the hydrogen dynamics within the co-deposit depend on its structure?
6. How does the structure relate to the ultimate hydrogen content of the deposits?

1.4 Scope of the Thesis

The present thesis tries to answer these questions by using various models (Molecular Dynamics, Monte Carlo, Kinetic Monte Carlo and analytical). The thesis is organized as follows:

- Chapter 2 is devoted to the description of various computational techniques that have been developed and used for the studies discussed in this thesis.
- Chapter 3 addresses question (1) above by presenting the studies on the synergistic erosion of hydrocarbon films using energetic argon ions and thermal H atoms.
- Questions (2) and (3) above are addressed in Chapter 4, where the fundamental processes leading to the growth of a-C:H layers are discussed.
- Chapter 5 addresses question (4), by using the insights from the previous chapter to build the Monte Carlo model of the film growth.
- In Chapter 6, question (5) is addressed using Kinetic Monte Carlo simulations.
- The last question is addressed in Chapter 7 using a simple analytical model based on hydrocarbon chains and their interactions.

1.5 Chapterwise Summary of the Thesis

Chapter 2: Computational Methods and Techniques

In Chapter 2, we discuss the techniques that have been used to study the problems discussed in the thesis. The basics of MD simulations are discussed in the first part, which is used to study the atomistic level understanding of growth and erosion of hydrocarbon films (using HydroCarbon Parallel Cascade, HCParCas code). The details of the equilibrium Monte Carlo code (Film Growth Monte Carlo-FGMC) is discussed, which was developed to study the growth and structure of co-deposits. Ballistic Deposition techniques is also presented which was developed to compare the surface properties of the co-deposits. Kinetic Monte Carlo simulations are discussed towards the end of the Chapter 2 which was used to study the hydrogen dynamics within the co-deposits.

Chapter 3: Modeling of Chemical Sputtering of Hydrocarbon Films

In Chapter 3, the synergistic erosion studies of a-C:H films using MD simulation is discussed. The hydrocarbon samples were bombarded by energetic Ar ions and thermal hydrogen atoms for different Ar energies and sample temperatures. The simulations report an enhanced erosion yield compared to a simple addition of physical sputtering (due to Ar ions) and chemical erosion (due to thermal H atoms) taken independently. A new mechanism, *Hydrogen Enhanced Physical Sputtering (HEPS)*, is proposed for explaining the enhanced erosion yield. This can be explained by the successive bond breaking by energetic Ar atoms and the passivation of the broken bonds by thermal hydrogen atoms. The steric repulsion arising from the H atoms prevents the re-attachment of the broken C–C bonds, which results in the emission of unsaturated energetic molecule from the film. The final erosion step is by ion bombardment. The role chemical and momentum transfer processes is clearly distinguished in the erosion. One of the key insight gained from the present study is the significance of the steric effects arising from H atoms of the sample. The mechanism is able to explain the energy dependence of synergistic erosion observed in ion-beam experiments.

Chapter 4: MD Studies on the Interaction of Methyl Radicals

In Chapter 4, MD simulation of the sticking of methyl (CH_3) radicals on a-C:H surfaces is discussed. Four different a-C:H surfaces (with different roughness, number of dangling bonds, hydrogen content *etc.*) were bombarded by CH_3 radicals. A new algorithm is developed for identifying the surface properties of amorphous films and is found to be capable of explaining the simulation data. The energy dependence of sticking is also studied. The important mechanism of incorporation of thermal radicals is the direct, ballistic incorporation. The sticking coefficient increases with the number of dangling bonds (between 1.3×10^{-3} to 5.86×10^{-2}). The energetic ion bombardment depletes the surface bound hydrogen and creates more dangling bonds. This explains the enhanced sticking coefficient observed in the ion-beam experiments [74]. The role of steric effect in the radical incorporation is brought out in the present analysis.

Chapter 5: Monte Carlo Modeling of Structure and Porosity of a-C:H Films

A Monte Carlo model for understanding the growth and structure of the film, which is discussed in Chapter 5. The code (Film Growth Monte Carlo, FGMC) takes into account the shape and orientation of CH_3 to build the structure. A parametric study is presented. The insights derived from the MD simulation allow us to narrow down to a realistic choice of parameters. Steric repulsion between H atoms on the surface is parametrized using a distace parameter called d_{crit}, such that, if the distance between H atoms is less than d_{crit}, the incorporation of the radical is rejected. The effect of shadowing in the site-selection is also incorporated. The steric repulsion is an important parameter in deciding the structure (atomic arrangement) and the microporosity of the films. The densities of such films are in a range of 1 gm/cc to 1.6 gm/cc which is typical of films formed without ion bombardment. The steric repulsion along with the shadowing effects cause the burial of dangling bonds deep within the film. Though the atomic hydrogen creates bonds within its penetration range, both these effects prevents the incorporation at certain locations. The 'buried' dangling bonds either get cross-linked or get hydrogenated by the diffusing hydrogen within the film. The H/C ratio of these films was close to 1.8, which is much higher than the observed values. This suggests the requirement of additional H elimination mechanisms for the growth of the films.

Chapter 6: KMC Simulations for H Dynamics

In order to study the dynamics of hydrogen within the co-deposited layers, Kinetic Monte Carlo simulations were performed. The dynamics of hydrogen within the film is modelled as a sequence of adsorption-desorption processes which in turn depends on the migration energy of hydrogen. We demonstrate a relatively simple method to calculate the migration energy, based on the potential energy surface analysis of the film. The migration energy distribution depends on the atomic arrangement of the film and shows considerable variation in the case of soft and intermediate density films. The range of atomic hydrogen is limited to a few surface layers ($\sim$ 2 nm) unlike graphite where the range is upto several microns, which is in agreement with the experimental observations.

Chapter 7: Analytical Multi-Layer Model for H Retention

In this chapter we discuss a multi-region multi-species analytical model for film growth. The model is based on the insights derived from MD and MC simulations and the idea that short polymeric chains grow, lock with each other and compactify. The reaction between various species is also incorporated in the model. It is interesting to note that, one can arrive at a more realistic ($\sim$ 1) H/C as observed in some of the tokamaks. The model brings out the importance of long-range steric effects in the structure formation. Constraints for achieving small H/C ratio is also brought out.

The Chapter 8 presents conclusions of the present thesis.

Chapter 2

Computational Methods and Techniques

In this chapter we discuss all the computational techniques that are used and developed for the computations presented in the thesis. They are:

- Molecular Dynamics (MD)
- Potential Energy Surface (PES) Analysis
- Monte Carlo (MC)
- Ballistic Deposition (BD)
- Kinetic Monte Carlo (KMC)

2.1 Molecular Dynamics

Molecular Dynamics simulations are used to study the mechanism of growth and erosion of hydrocarbon films. The brief overview of MD techniques and the specifics of the code is discussed in the subsequent sections.

In the MD simulations for an N particle system, following equations are solved

$$m_i \ddot{\vec{r}}_i = \sum_{i \neq j, j=1}^{N} -\nabla V_{ij} \tag{2.1}$$

where $\vec{r}_i$ is the position of the particle at any instant t and V_{ij} is the potential in which the atoms interact with each other known as *Interatomic Potential* (IP). Molecular dynamics aims to solve this equation for N atoms numerically [93, 94].

2.1.1 Interatomic Potentials (IP) - Brenner potential

The most important part of MD simulation is the choice of IP which decides the accuracy of interactions between particles. The most accurate description of the interatomic potential comes from the quantum mechanical description of atoms and molecules. Though the exact solution of a quantum system is available only for single electron systems like hydrogen atom, there exist a number of approximation techniques for describing the ground state of many-electron systems such as Density Functional Theory (DFT) [95, 96].

Though quantum mechanical calculations show considerable progress, for problems which involve large systems or require statistical averages these calculations are numerically intensive. One solution to this problem is to use a more generalized approach, where the physics is incorporated based on simple quantum mechanical arguments called *bond order*. Bond order is defined as *half the difference between number of bonding electrons and anti-bonding electrons in the molecular orbital.* It is often defined as the index of bond strength, *i.e.*, the more neighbours an atom has the weaker the bond to each neighbour will be. Potentials based on the concept of bond order are known as *bond order potentials* [97].

Because of the crucial role of bond order and its dependence on the local neighborhood, an environment dependent bond-order was explicitly included into the potential formalism for covalent solids like Si, Ge, C *etc.* by Abell *et. al.* [98] in the following form,

$$
\begin{aligned}
E = \sum_i E_i = \frac{1}{2} \sum_{i. \neq . j} V_{ij} \\
V_{ij} = f_C(r_{ij}) \left[a_{ij} f_R(r_{ij}) - b_{ij} f_A(r_{ij}) \right]
\end{aligned}
\tag{2.2}
$$

where, E is the total energy of the system, which is decomposed into a site energy E_i and a bond energy V_{ij} and r_{ij} is the distance between i and j atoms. The function f_R represents a repulsive pair potential and f_A represents attractive pair potential associated with bonding. The term f_C is a cut-off function to limit the range of potential since often potential is short ranged and this reduces the computational cost [97, 98].

The function b_{ij} is the feature of such potentials which represents the bond-order and is assumed to be monotonically decreasing function of the coordination of atoms i and j. The function a_{ij} consists of limiting terms of range of interaction to first neighbor shell of atoms. Such type of formalism is known as Abell-Tersoff type (also known as Reactive Empirical Bond Order(REBO) potentials where it is able to describe chemical reactions to some extent) [97]. This was extended for carbon and hydrocarbon systems by parametrizing the bond order term for a number of small hydrocarbon molecules, graphite as well as diamond by Brenner [99, 100]. This resulted in an empirical potential for hydrocarbon systems and which is used for the simulations discussed in this thesis. The potential has been implemented in Hydrocarbon Parallel Cascade (HCPARCAS) code maintained by K. Nordlund *et.al* [101].

The fit parameters used in the simulations are for Potential II given in [100]. The code was tested for bond lengths and bond angles [55, 101, 102]. The equilibrium parameters given in the paper [100] are compared with the values obtained from the code and are shown in Table 2.1.

The C–C potential profile and the C–C bond oscillations about the mean bond length is shown in Fig. 2.1.

Table 2.1: The comparison of equilibrium parameters obtained from HCPARCAS with the fit parameters of Brenner potential (Potential II table)

Parameter (Equilibrium)	Symbol	HCPARCAS Code	Fit data (Potential II) [100]
H–H distance	$\mathrm{R}_{HH}^{(e)}$	0.7356336 Å	0.74144 Å
H–H energy	$\mathrm{D}_{HH}^{(e)}$	4.750203 eV	4.7509 eV
C–C distance	$\mathrm{R}_{CC}^{(e)}$	1.3894 Å	1.39 Å
C–C energy	$\mathrm{D}_{CC}^{(e)}$	5.99998 eV	6 eV
C–H distance	$\mathrm{R}_{CH}^{(e)}$	1.119786 Å	1.1199 Å
C–H energy	$\mathrm{D}_{CH}^{(e)}$	3.642199 eV	3.6422 eV

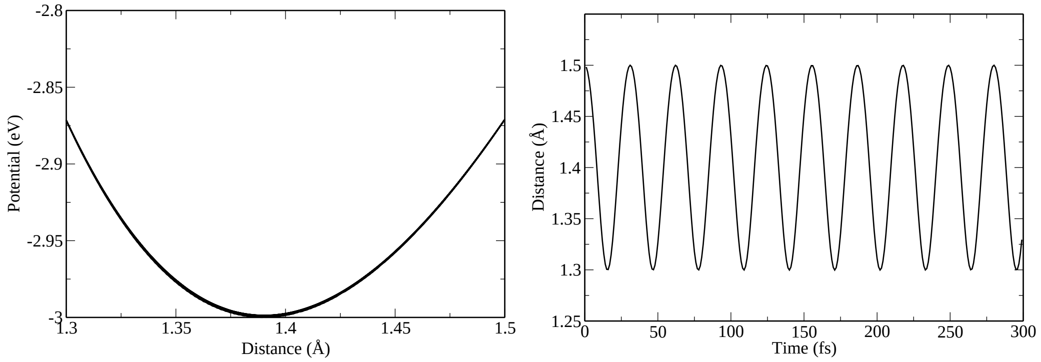

Figure 2.1: (left) C–C pair potential and (right) C–C bond oscillations about the mean position.

2.1.2 Boundary Conditions

In MD simulation, the number of atoms which can be simulated is limited between 1 and 10^9 depending up on the type of potential. In the case of Brenner potential, this number is typically around 10^3. The fraction of atoms which are closer to the boundaries will experience a different environment than that at the interior. If we consider a 1000 atom system, the number of atoms close to the wall is typically $(1000)^{\frac{2}{3}}$ and if we leave two such layers of atoms, then $\frac{1}{5}$ of the atoms are near the surface. In the case of real macroscopic systems, it will be one in 10^7 atoms. Therefore, the simulations will not be able to capture the essence of the bulk state of the system. However, this problem can be overcome by implementing periodic boundary conditions. This means, in 3D case, a cubic box (which is the basic cell in 3D) is repeated throughout the space to form an infinite lattice. For a detailed discussion of periodic boundary condition see Ref. [93].

Other boundary conditions used in MD simulations are 'free' or 'open' when simulating a small collection of atoms or a long chain of molecule. Such boundary conditions are used for simulating surfaces in MD simulations as well. In order to construct a sample with surface the typical boundary conditions would be periodic along X and Y directions (i.e., L_x and L_y are periodic) and free boundary along Z axis which is denoted as L_z. This is the typical boundary condition used for simulating hydrocarbon surfaces discussed in the thesis.

2.1.3 MD Algorithm

Once the potential is chosen, MD simulation consists of solving the classical equation of motion numerically. A simplified version of the algorithm is schematically shown in Fig. 2.2 [4].

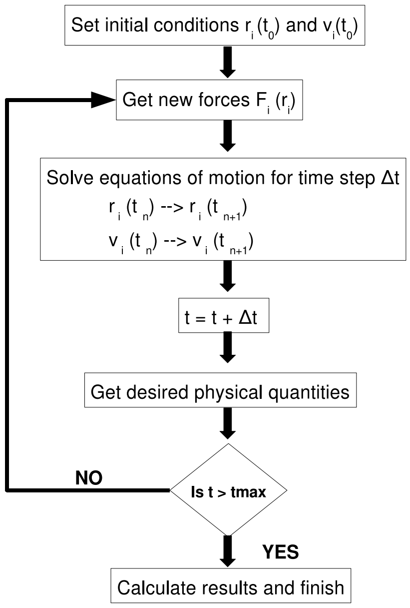

Figure 2.2: Schematic of MD algorithm [4]

Once the basic cell dimensions and boundary conditions are set, the simulation pattern follows more or less what is described by the figure 2.2. As we need to solve Newton's equations of motion, initial conditions of particle positions or velocities are to be specified at the beginning of the simulation. The initialization of positions depend on the kind of structure under consideration. For example, for amorphous hydrocarbon films, one starts with a random collection of carbon and hydrogen atoms. The randomness in the position is generated using random number generators, which is described in section (2.3). The initial velocities are sampled from a Maxwell-Boltzmann distribution function which is a Gaussian function with a suitable scaling factor. Thus the initial velocity distribution is a Gaussian corresponding to the desired temperature. The net momentum of the system is set to zero to prevent the entire cell starting to move.

$$\vec{P} = \sum_{i=1}^{N} m_i \vec{v}_i = 0 \tag{2.3}$$

Thus the system satisfies the condition described by equation (2.3). At any time t the distances r_{ij} and the forces F_{ij} between nearby atoms are calculated. From these the equation of motion can be solved to get the positions and the velocities. This is achieved by the numerical integration of equation of motion.

2.1.3.1 Numerical Integration

A standard method of solving ordinary differential equations is by finite difference approach. The general idea is that given the positions and velocities at time t, at a later time $t+\delta t$ the quantities are calculated with sufficient accuracy. The equations are solved on step-by-step basis and the choice of δt depends on the method of integration. The displacement over a time step δt is denoted as δr and this has to be much smaller than the distance between atoms to avoid the abrupt variations in the potential. There exist many such integration algorithms such as Vertlet, Leap Frog, Predictor-Corrector, Beeman *etc* [4, 93, 94, 103]. Predictor-Corrector (PC) method is used in the simulations discussed in the thesis.

The general scheme of predictor-corrector algorithm can be summarized as follows:

1. predict the positions, velocities, accelerations etc., at a time $t + \delta t$ using the current values of these quantities (at t)

2. evaluate the forces and hence the accelerations using the new positions

3. correct the predicted positions, velocities, accelerations etc., using the new accelerations

4. calculate the variables of interest such as energy, order parameters etc., for this time step before going to step (1).

In most of the cases, predictor gives an initial guess, no matter how accurate, since the successive corrector iterations rapidly converge into the correct solution. However, in MD simulations, the acceleration calculations are the most time consuming part and it is implicit in each corrector step, a large number of corrector iterations could be numerically expensive. Normally, one or two corrector steps are iterated and therefore, the closest accuracy of the predictor values are essential for the fast computation.

Once the time step advanced to $t + \delta t$, the macroscopic properties of interest such as temperature, pressure, response functions *etc.* can be calculated from the microscopic states like positions, velocities, individual kinetic and potential energies of the system at that time. At equilibrium the instantaneous kinetic and potential energy fluctuates around an average value. The instantaneous temperature is given by statistical mechanics as:

$$\frac{3}{2}kT = \frac{1}{2}m_i v_i^2. \tag{2.4}$$

In the equilibrium simulations of real systems, most of the measurements are done at constant temperature and/or pressure and therefore, the simulations are also needs to be done for constant pressure and/or temperature conditions which are implemented by temperature and pressure control algorithms.

2.1.3.2 Temperature and Pressure Control

In this thesis, we discuss the chemical erosion and the growth of hydrocarbon films by the bombardment of energetic as well as thermal atoms. Each of these bombardment event is a non-equilibrium process and therefore, the temperature of the system rises locally to a different value than the desired equilibrium temperature. Due to the periodic boundary conditions discussed in section (2.1.3), this excessive heat can not “escape” out of the system. Therefore, there needs to be mechanisms, which effectively brings down the temperature of the system back to the equilibrium value [104–106].

From equation (2.4), it can be seen that reducing velocities would reduce the temperature. The temperature can be effectively controlled by coupling to an external heat bath much similar to a canonical ensemble. In order to obtain a global coupling with minimal local disturbance, for a system with instantaneous temperature T under stochastic coupling, gives proportional scaling in velocity of the form $v = \lambda v$. The scaling factor λ can be written in the following form,

$$\lambda = \left[1 + \frac{\Delta t}{\tau_T}\left(\frac{T_0}{T} - 1\right)\right]^{\frac{1}{2}} \tag{2.5}$$

where, $\tau_T = (2\gamma)^{-1}$, is the coupling parameter and γ is the coupling constant. A small value of τ_T corresponds to a strong heat bath. The values of τ_T lies between 0.001 and 1. A similar kind of expression can be derived for the pressure control, with a proportional scaling in the coordinates of box length from l to μl. The scaling parameter μ is written as,

$$\mu = \left[1 - \frac{\Delta t}{\tau_p}(P_0 - P)\right]^{\frac{1}{3}} \tag{2.6}$$

where, τ_p is the time constant for the pressure control which should typically be greater than $100\Delta t$, P_0 is the desired pressure and P is the instantaneous pressure. β is the isothermal compressibility of the system. Such a scheme of velocity and pressure scalings are generally known as Berendsen scalings [104]. With large values of τ_T and τ_p such scalings gives realistic fluctuations in the system.

2.1.4 MD Units

The HCParCas code needs inputs of the positions of the atoms, velocities and the atom types along with the desired simulation box lengths. The units used in the simulations are scaled with respect to the box lengths and the time. If L_i is the length of the box in any direction of the sample, then the distances, velocities, accelerations, time and force are scaled as follows:

$$
\begin{aligned}
x^i_{scaled} &= \frac{x^i_{real}}{L_i} && (2.7)\\
v^i_{scaled} &= \frac{v^i_{real}}{L_i} * \delta && (2.8)\\
a^i_{scaled} &= \frac{a^i_{real}}{L_i} * \frac{\delta^2}{2!} && (2.9)\\
\delta &= 10.1085 * \sqrt{m} && (2.10)\\
F^i_{scaled} &= \frac{F^i_{real}}{L_i} && (2.11)
\end{aligned}
$$

where *real* represents the MKS units, *scaled* is in the scaled units, δ is the time unit and the m is the mass in amu. The simulation box is scaled between -0.5 to 0.5. The code uses adaptive time step and the maximum is 1 fs, which corresponds to 0.025 in the scaled units.

2.1.5 Post processing of MD Results

The solution of the equation of motion (2.1) gives the positions, velocities and acceleration of particles at any instant of time. The total kinetic energy, potential energy and the total energy of the system can be calculated by averaging over fixed time steps. Various macroscopic properties such as temperature, pressure, specific heat *etc.*, can also be derived from the data, depending on the types of simulations.

Specific post processors are developed to capture the microscopic details of films under various circumstances which are discussed in the corresponding chapters. The post processors were also developed for analyzing large volume MD data for estimating the statistics of various surface processes.

The inherent limitation of the time of simulation (maximum time upto a few ns) and the number of atoms (a few thousands of atoms) which can be used in MD simulations pause serious limitations in modeling the real time dynamics of systems. In order to overcome this, we have developed techniques based on potential energy surfaces (PES). Also, we have used kinetic and equilibrium Monte Carlo techniques, details of which are discussed below.

2.2 Potential Energy Surface (PES) Analysis

A new technique based on potential energy surface analysis was developed for estimating the Migration Energy of hydrogen atoms within amorphous hydrocarbon films. The technique involves the calculation of PES of H atoms within the a-C:H sample and the details are discussed in corresponding context in Chapter 4 and Chapter 6.

2.3 Monte Carlo (MC)

Monte Carlo methods are the techniques which use a sequence of random numbers to obtain statistical estimates of the parameters which we wish to model. We have used MC techniques to study the growth of hydrocarbon films from methyl (CH_3) radicals.

The central part of the MC simulations is the concept of random variables and distributions which is implemented using computer generated random numbers [103, 107–109]. A random variable is a variable that can take any value, which cannot be predicted in advance. Though the variable is unpredictable, the distribution of the variable may be known, which is the probability of a given value. The Probability

Density Function (PDF) $g(u)$ of random variable u is defined as,

$$g(u)du = P[u < u' < u + du] \tag{2.12}$$

where, the PDF gives the probability of finding a variable u' within du of a given value u. It is often defined an integrated PDF where, the definite integral of g from $-\infty$ to u is taken and the integral is normalized such that the values are from 0 to 1.

The random numbers are generated out of a uniform distribution where the probability of occurrence is same for all the values. The algorithm which we used to generate the random numbers is based on congruential generator. The random numbers u' are generated by,

$$u' = (IA * u' + IC) mod M \tag{2.13}$$

where the values are $IA = 843314861, IC = 453816693, M = 2^{31}$ and the period of occurrence is 4×10^{18}, which means within the period no two numbers are repeated. These types of generators are called pseudo random numbers and the sequence is defined by a small set of initial numbers.

Based on the Monte Carlo technique a 3D code was developed for simulating the growth of amorphous hydrocarbon films from thermal methyl radicals, known as Film Growth as Monte Carlo (FGMC). The code is taking into account the detailed atomistic features such as bond angle, bond length, configurations of the molecules *etc.*

2.3.1 Description of the code

The code assumes an initial sample size of $(nx \times ny \times nz)$ volume binned into 1 Å^3 cubes. The bin size is chosen in such a way that it is smaller than any bond lengths we use in the simulation (C–H bond length: 1.11 Å, C–C bond lengths: 1.54 Å for sp^3 configuration and 1.34 Å for sp^2). An electron-pair repulsion model which is computationally much cheaper to implement than the MC or MD relaxation techniques, is used to decide the stereoscopic orientations [110]. This helps to model details of molecular hydrocarbon deposits upto several nano-meters and allows to have sufficient thickness (mean height $\simeq$ a few times the linear sample dimension) of co-deposits to characterize the porosity and roughness of the films in terms of parameters affecting them.

2.3.1.1 Probabilities

The probabilities of various surface reactions during the growth is calculated either from MD simulations or from available experimental data. The events which are considered for the growth are (a) sticking of CH_3 in sp^3 (tetrahedral) configuration, (b) sticking as sp^2 (planar) configuration, (c) H abstraction by the incoming CH_3 and (d) null event where (a), (b) or (c) did not happen. An integrated PDF of all the probabilities was calculated and random numbers were used to sample the PDF.

2.3.1.2 Site Selection

The selection of a particular site for incorporation is decided by the shadowing that has. Let us consider a site to be the centre of a sphere, with standard spherical polar coordinate system having its z-direction as the direction of film growth. We consider an isotropic incidence of radicals and hence a site can be approached from any angle in the upper hemisphere ($0 \leq \theta \leq \pi/2$). Since, the incoming particles stick upon the first contact, surrounding structures which are taller than the site can intercept the particle, causing the shadowing effect. The concept of shadowing effect is shown in Fig. 2.3. The actual exposed area around a site is therefore solid-angle averaged.

Nearest neighbours can also completely shadow a given site, in which case, there is little point in calculating shadowing effects due to far away neighbours. Therefore the shadowing calculation has been splitted to two parts. Nearest neighbour coverage for a given site is calculated by considering occupancy of seventeen bins (each of 1 $Å^3$), formed by in-plane and top-layer of a $3 \times 3 \times 3$ $Å^3$ cube, with the site at

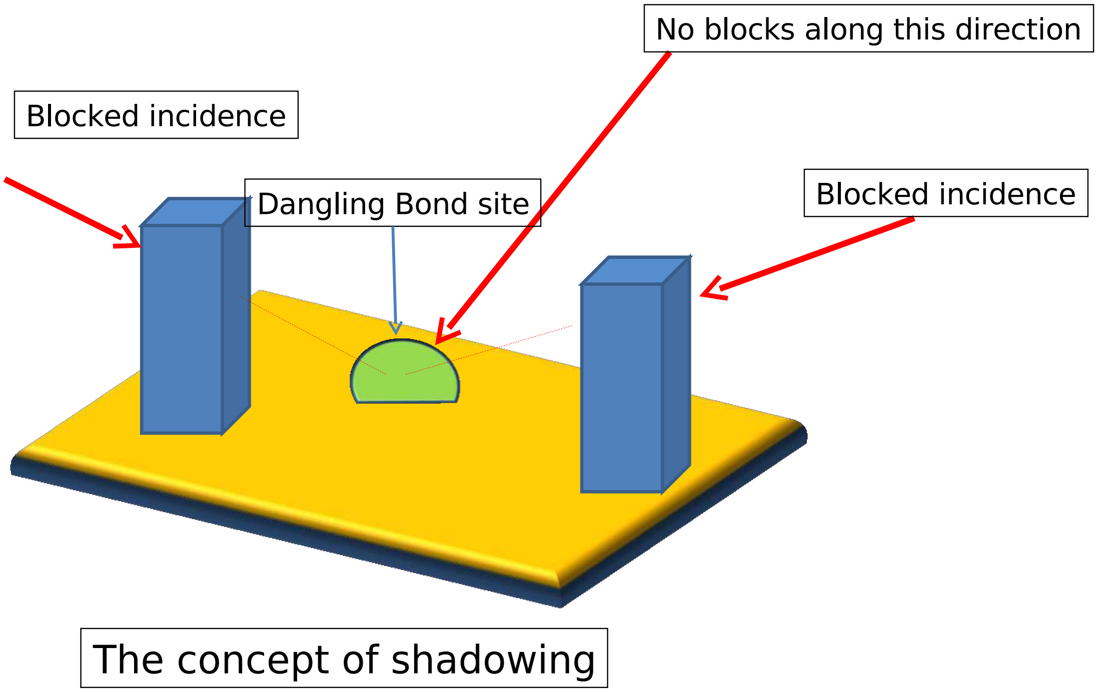

Figure 2.3: Schematic of the concept of shadowing

the center. Fraction of the area covered (f_{near}) is then given by (no. of occupied bins)/17. Far neighbour-coverage is calculated from the solid angle subtended by all columns of atoms (height measured relative to the site, 1 Å^2 cross-section) at the site. Overlapping shadows are removed and this sum is divided by 2π (the maximum solid angle exposure that a site can have) which we define as f_{far}. The probability of an i'th site being visited (p_i) is then given by $p_i = 1 - f_{near} - f_{far}$. The choice of sites to be updated is then decided by normalizing the cumulative probability of all sites to unity and selecting any site by random selection.

Though the incoming radicals are uniformly random over the surface, the sticking is not uniform as the probability of a site is being selected for incorporation is decided by the shadowing. Therefore, growth is the convolution of the incoming uniform random distribution and the surface distribution of dangling bonds.

2.3.1.3 Radical Incorporation

the sticking of methyl radicals to the surface can be considered as a ballistic process, where, the atoms stick upon 'first contact', when dropped randomly in chosen 'bins'. The radical incorporation to a dangling bond location is by exploring various equilibrium orientations it can have. This can be understood as follows: in a C_2H_6 molecule, along the C–C bond axis, the H atoms are arranged in such away that they form a staggered configuration. That is, the shortest angle between their projections along the C–C bond axis is 60 degrees for sp^3 configuration (see Fig 2.4 this angle ϕ_b in the simulations. For the sp^2 case $\phi_b = 0$ under ideal conditions, e.g., a graphene layer). Because of the non-crystalline nature, ideal values for ϕ_b will not be possible. Therefore, a site is first explored for bonding possibilities by considering different values of ϕ_b. For each value, the distance between newly arrived H atoms and those in the neighbourhood is calculated. If the H-H distance is greater than a critical value, d_{crit}, the bonding event is accepted. Introduction of parameter d_{crit} is like introducing 'steric-repulsion' as in the electron-pair repulsion model. The code also uses a distance d_{cut} as the cutoff distance for cross-linking. If the distance between two C atoms in the sample is equal to d_{cut}, those atoms are considered for cross-linking by inserting another C atom with 2 hydrogens between them. The incorporation is done only if the H atoms obey the steric repulsion criteria. The structure of the film formed is shown in Fig. 2.5.

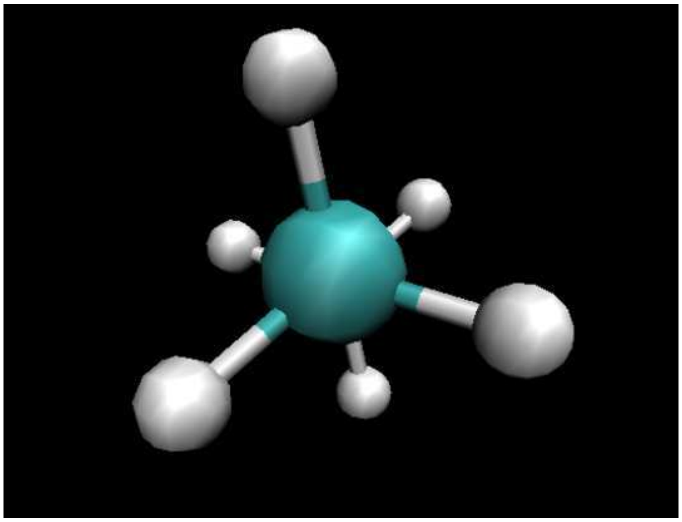

Figure 2.4: Staggered configuration of ethane molecule

2.3.1.4 Data Storage

The code uses highly vectorized algorithm and the details of atoms in the sample are stored in a dynamic array called 'W-matrix'. The entries of W-matrix are the bin index, atom type, bond type (sp^2 or sp^3), number of connections, X, Y and Z locations of atoms, θ, ϕ and phi_b values, and the bin indices of connected bins. The matrix contains these information of carbon, hydrogen and dangling bonds present in the system. The post processing of W-matrix gives all the necessary information need to characterize the film. The X, Y, Z coordinates can be plotted to obtain the picture of the film shown in Fig. 2.5. Another dynamically defined hypermatrix of size $nx \times ny$ is defined for defining the height of each bin (K_{max}) and from where average and height and surface roughness of the film is calculated. The roughness is defined as the mean square deviation of the height.

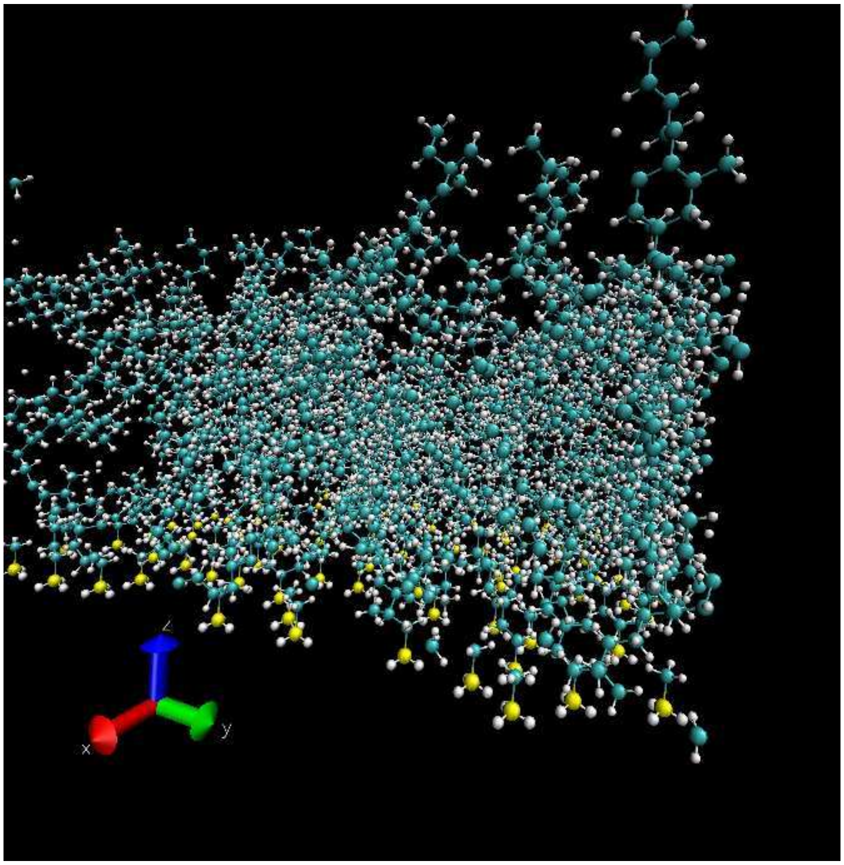

Figure 2.5: The film formed in FGMC

2.3.1.5 Inputs

The inputs of the code are:

- steric repulsion parameter d_{crit}
- initial surface roughness *hdepth*
- cut-off distance for cross-linking d_{cut}
- C–C single bond length *L3*
- C–C double bond length *L2*
- C–H bond length *LH*
- bin size *L*
- sample size along X, Y and Z direction *nx,ny and nz.* All these distances are specified in Å.
- pattern of initial dangling bond arrangement for ordered or disordered lattice *isep*
- initial radical density *rad*
- probabilities and cross-sections for various reactions (H abstraction, H addition, CH_3 addition, sp^2 to sp^3incorporation) P_{abs}, P_{add}, s_{ch3}, s_{add}, P_{sp23}
- flux of CH_3 and H j_{ch3} *and* j_h

In order to obtain the statistical credibility of calculated parameters, several trials have to be done. Let n_1 be the parameter which we calculate from the code out of N trials, then the fluctuations in the value of n_1 goes as $\frac{\Delta^* n_1}{n_1} = \frac{1}{\sqrt{N}}$. Therefore, as N increases the confidence in the value of the parameter also increases.

2.3.1.6 Outputs

The W-matrix is post processed to get all the output parameters. Since the matrix contains the information of all the occupied bins, the empty bins for a given sample size can be calculated. From this the porosity and void size distribution are calculated. The density, hydrogen content and the radial correlation function of the film are also calculated. The main outputs from the code are:

- density of the film
- porosity
- average height
- surface roughness
- hybridization ratio
- hydrogen content
- void size distribution
- dangling bond distribution within the sample

These quantities can be calculated as a function of the input parameters.

2.4 Ballistic Deposition (BD)

Ballistic deposition is one of the earliest model adopted for explaining the roughened interfaces in non-equilibrium process such as thin film growth. The basic idea of the model is that an atom (spherical particle) is randomly dropped in straight line far from the surface and stick upon the first contact. The first contact is decided by the maximum height of all the neighbouring bin. Fig. 2.6 shows the schematic of first contact principle [59, 63]. A set of routines were developed for simulating ballistic deposition in 2D and 3D cases with normal and isotropic incidence. The method is

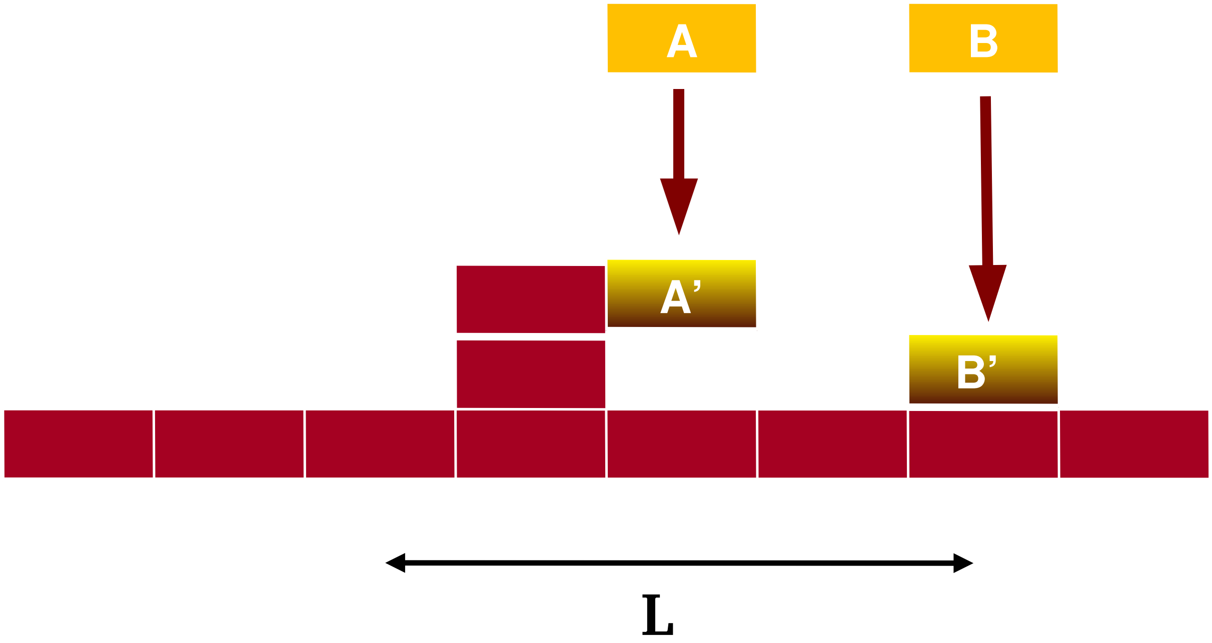

Figure 2.6: Schematic of ballistic deposition for L bins. The particle A will stick to location A' where as B will reach the bottom location B'.

capable of generating porous structures and a typical structure formed in 3D case is shown in Fig. 2.7.

The surface roughness of the film grown is calculated as the fluctuations in the mean height. The fluctuations are arising due to the first contact principle. This also leads to porosity of the film. The plot of surface roughness is shown in Fig. 2.8.

The ballistic deposition shows scaling laws as follows: let σ be the roughness of the surface, then in the saturated roughness, where, mean height of the film $H >> L$, the sample width scales as $\sigma_{sat} \sim L^{\alpha}$ and α is known as the roughness exponent [62]. If $H << L$, then the roughness scales as $\sigma_{growth} \sim H^{\beta}$, where β is the roughness exponent. Typical values of α and β for 3D ballistics are 0.25 and 0.5 respectively. These scalings of 3D ballistics model is compared with the exponents of FGMC code and the details are discussed in Chapter 5.

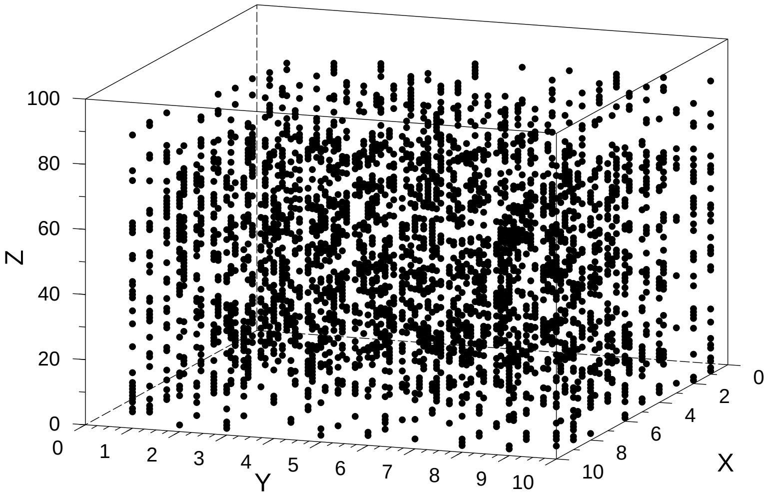

Figure 2.7: The ballistic deposit formed in 3D simulation with normal incidence of spherical particles. The width is 10 × 10 arb. unit. and mean height is 100

2.5 Kinetic Monte Carlo (KMC)

The evolution of dynamical processes in a system can be described by Master equation as in eqn. (2.14). This inherently assumes a Markovian process, where the probability of transition of a dynamical variable y at time t_{n-1} from a value y_{n-1} at a time t_n depends only on the value of y at $t-1$.

$$\frac{\partial P(\sigma_f,t)}{\partial t} = \sum_{\sigma_i} W(\sigma_i \to \sigma_f)P(\sigma_i,t) - \sum_{\sigma_f} W(\sigma_f \to \sigma_i)P(\sigma_f,t) \tag{2.14}$$

Here, σ_i and σ_f are the successive states of the system and $P(\sigma_f,t)$ is the probability of the system at σ_f and $W(\sigma_i \to \sigma_f)$ is the probability per unit time that the system undergoes a transition fro σ_i to σ_f [111–113].

At the steady state, the system obeys detailed balance condition and hence the individual transition probabilities balance each other. The KMC provides a numerical solution to the Master algorithm for both equilibrium as well as non-equilibrium cases with real time. KMC is accomplished on a time scale where no two events occur simultaneously. The task of KMC algorithm is to create a

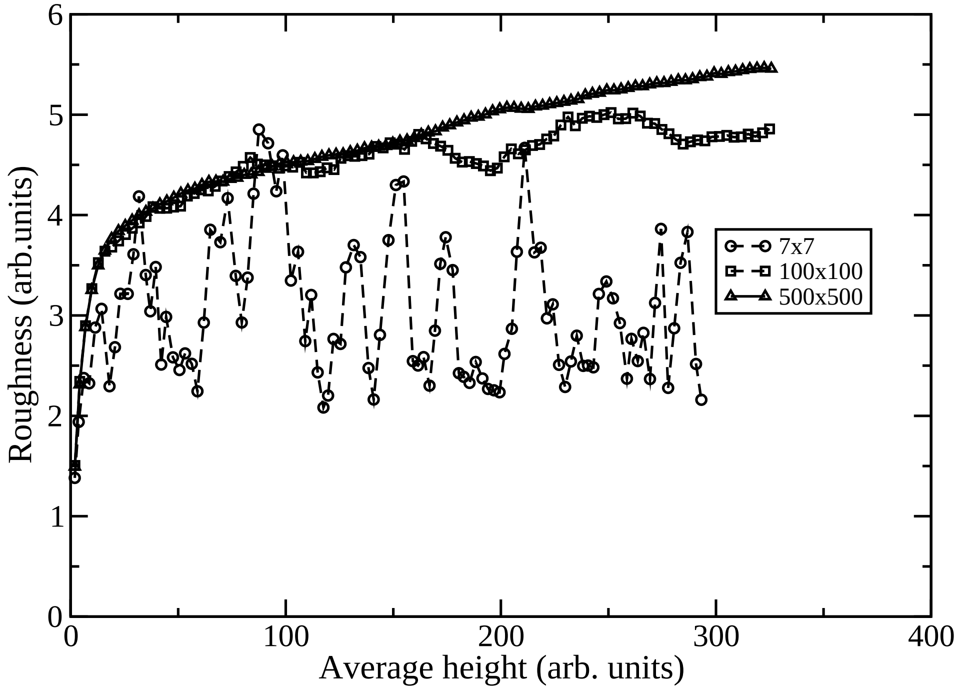

Figure 2.8: The surface roughness evolution in ballistic deposition process with normal incidence.

chronological sequence of events separated by intervent times. One of the most important assumption of KMC is that any transition which is possible at time t is again possible at time $t + \Delta t$, based on its rate and independent of the previous occurrences. This is by definition a Poisson process and the probabilities are given by Poisson distribution (eqn. (2.15)),

$$P(n) = \frac{(Rt)^n}{n!} e^{-Rt} \tag{2.15}$$

where R is the sum of the rates of n processes occurring in the system.

The time between two events (τ) in the Poisson distribution is $e^{-R\tau}$ and has a value between 0 and 1. Thus, the time interval can be written as,

$$\tau = \frac{-ln(U)}{R} \tag{2.16}$$

where, U is a uniform random number between 0 and 1.

In the thesis we use KMC simulations to study the dynamics of H atoms within the a-C:H films, which is a thermally activated process. The transport of hydrogen within the film is done as adsorption-desorption processes where the jump of an atom out of the potential well is characterized as Arrhenius-like process [5, 22]. The rate at which a particle jumps out of a potential well (ω) (as shown in Fig. 2.9) at any temperature T can be written as

$$\omega = \omega_0 e^{\frac{-E_m}{kT}}$$

where ω_0 is defined as the jump (transition) attempt frequency, typically has the value 10^{13} per second and E_m is the Migration Energy (ME) of the H atoms within the sample and k is the Boltzmann constant. For n_i species having ω^j jumps, the rates R can be written as follows.

$$R = \sum_{i=1}^{Nspecies} \sum_{j=1}^{Njumps} n_i \omega^j \tag{2.17}$$

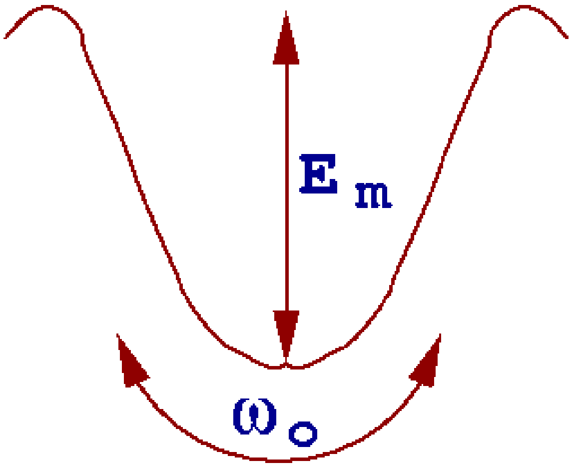

Figure 2.9: A schematic of migration energy [5].

The most crucial parameter which decides the frequency of jumps is the Migration Energy of the H atoms, E_m. The value of E_m depends on the local atomic arrangement the jumping H atoms encounters and therefore, is not a single value constant for amorphous films. Hence, one of the challenging problems of solving

KMC algorithm for H dynamics in amorphous films is to find the ME values. We have developed a method based on the PES analysis to calculate the E_m values of a-C:H films, details of which are discussed in Chapter 6.

Once ME values are known, KMC technique is to solve the Master equation using numerical methods and we have used Bortz-Kalos-Lebowiz (BKL) algorithm implemented in ReactsDiff code [22]. The BKL algorithm picks an event from the cumulative distribution of probabilities R in a random manner by using a uniform random number between 0 and 1 and the time is updated by an amount given in equation (2.16) [114].

To summarize, in this chapter we have discussed the numerical techniques that have been used for addressing the problems of the thesis. They are: (1) Molecular Dynamics, (2) PES analysis, (3) Monte Carlo, (4) ballistic deposition techniques and (5) Kinetic Monte Carlo techniques.

Chapter 3

Modeling of Chemical Sputtering

`In this chapter we discuss the chemical sputtering of hydrocarbon films using molecular dynamics simulations.`

3.1 Introduction

The erosion of the carbon based Plasma Facing Components (PFC) releases various carbon species into the edge plasma. The deposition of the eroded materials along with hydrogen isotopes results in the formation co-deposited hydrocarbon films in the regions adjacent to the erosion zones, which are further eroded by the plasma. The radicals/molecules thus formed can undergo long range transport and reach the remote regions of the tokamak such as *pump ducts, baffle plates etc.* Such a model was used to explain the deposition observed in the louvres of JET tokamak [45]. The kinetic energy of the hydrogen ions from the edge plasma is typically in the rang of 10 eV – 100 eV. At this energy range, both the kinetic energy and chemical reactivity of the hydrogen together can assist the erosion of these layers. Thus, the erosion yields are expected to be different than that observed in pure physical sputtering and chemical erosion.

In order to understand and distinguish the kinetic and chemical effects of hydrogen in the erosion of a-C:H films, experiments were performed in the past, where the kinetic and chemical effects are separated by using particle beams. The kinetic energy is supplied by chemically inert noble gas ions such as argon and chemical reactivity is provided by thermal atomic hydrogen beams [115, 116]. These experiments reported a dramatic increase in the erosion yield than what can be accounted for from a simple addition physical sputtering (due to Ar ions) and chemical erosion (due to thermal H atoms). The energetic ion creates dangling bonds within the film by bond breaking and the atomic hydrogen attaches to these dangling bonds. It is believed that this synergistic interaction of the energetic ions and the thermal hydrogen (bond breaking and attachment) leads to the enhanced erosion yields in such systems [116–119]. Similar enhancement in the yield was also reported by experiments using hydrogen ion beams of moderate energy ($\sim$ 100s of eV) [120,121].

The models for such enhanced erosion were based on the formation of saturated, thermal hydrocarbon molecules within the hydrocarbon films as a consequence of the successive bond breaking and passivation [117]. These molecules were believed to diffuse from deep within the bulk of the film. Such processes are generally termed as *chemical sputtering*, which indicates the role of both momentum transfer and chemical processes involved in the erosion [20]. However, in the presence of energetic ion bombardment along with the steric repulsion arising from the H atoms, the possibility of such saturated molecule formation seems impossible. Thus, we expect that the erosion happens as a consequence of the formation of the unsaturated energetic molecules aided by ion bombardment. Also, the existence of diffusion channels for molecules at lower substrate temperatures ($\leq$ 600 K) also needs to be understood from a fundamental point of view.

Therefore, to understand the atomistic level picture, we have performed Molecular Dynamics (MD) simulation by using energetic Ar ions (range of 25 eV – 200 eV) and thermal H atoms (0.5 eV). The simulations were carried out in four different cases to understand the effect of kinetic and chemical aspects involved in the erosion process. They are,

1. H/Ar dependence: to understand the role of atomic hydrogen in the erosion process.

2. Energy dependence: to understand the effect of incident energy of Ar ions, which reveals the role of momentum transfer processes [17].

3. Angle dependence: to further clarify the role of momentum transfer processes as they (physical sputtering) exhibit a pronounced angle dependence [17].

4. Temperature dependence: The chemically activated processes show temperature dependence as the activation barriers are reduced at higher temperatures [19].

The details of the study are discussed in the subsequent sections of this chapter. In Section (3.2) the basic simulation setups are described. This includes the method of sample creation and the bombardment simulations for various cases. In Section (3.3) the major results of the simulations are presented. The discussion of the results are given in Section (3.4). The mechanism of erosion is discussed in (3.4.1) and the conclusions are presented in Section (3.5).

3.2 Setting up Simulations

The simulations were performed using a MD code, Hydrocarbon Parallel Cascade (HCParCas version V3.22), which employs a fifth-order predictor-corrector Gear algorithm to calculate the positions and velocities of particles using adaptive time steps [101]. The interactions of Ar atoms with carbon and hydrogen were modeled using additive pair-potentials. The C–C and C–H interactions were modelled using Brenner potential [99,100]. The creation of the a-C:H sample and the bombardment simulations are discussed in the following sections.

3.2.1 Sample Creation

The a-C:H samples were created by annealing a collection of carbon and hydrogen atoms using the Brenner potential for about 70 ns. The details of sample preparation is given in Appendix A. The final sample consisted of 930 atoms in $14 \times 14 \times 28$

Å^3 volume with an H/(H+C) ratio of 0.38 and a density of 1.750 g/cm^3. This corresponds to a-C:H layers deposited from ethylene plasma discharges with typical parameters of H/(H+C)=0.39 and a density of 1.7 g/cm^3 [122]. The fractions of 3-fold and 4-fold coordinated carbon atoms were 60 % and 37 %, which is in good agreement with the experimental data for a-C:H films with properties intermediate between hard and soft [79]. The sample thus created is shown in Fig. 3.1. The original sample was heated or cooled upto the desired temperatures for making samples at different temperatures.

3.2.2 Bombardment Simulations

The bombarding atoms were initialized at a height of 7 Å above the surface, which is beyond the largest cutoff radius of 4.5 Å of all the potentials used in this simulation. The energetic argon atoms typically thermalized within the sample for about 0.5 ps after the impact, and thereafter the sample was relaxed for another 4.5 ps. Thus the total simulation time for Ar impact was for 5 ps. The hydrogen atoms of 0.5 eV were bombarded on the Ar bombarded surface in a cumulative manner. The angle of incidence for hydrogen atoms was chosen to be 45° to the surface normal as it represents a more general case of incident angle. The simulation time for a single H bombardment was 5 ps. The simulations were performed under 4 different parametric regimes to understand (a) H/Ar flux ratio dependence, (b) energy dependence, (c) angle of incidence and (d) temperature dependence. Ten sets of simulations were performed in all the cases and each set consists of 13 cumulative repetitions of the (1 Ar + different number of H atoms) cycle plus a final Ar impact.

3.2.2.1 H/Ar Flux Ratio Dependence

The aim of these simulations is to understand the role of H atoms in the erosion process. In order to achieve this, the original sample at 300 K was bombarded with 100 eV Ar atoms at 0° angle (along the surface normal) and at random locations on the surface. The number of H atoms varied between 0 (pure Ar bombardment)

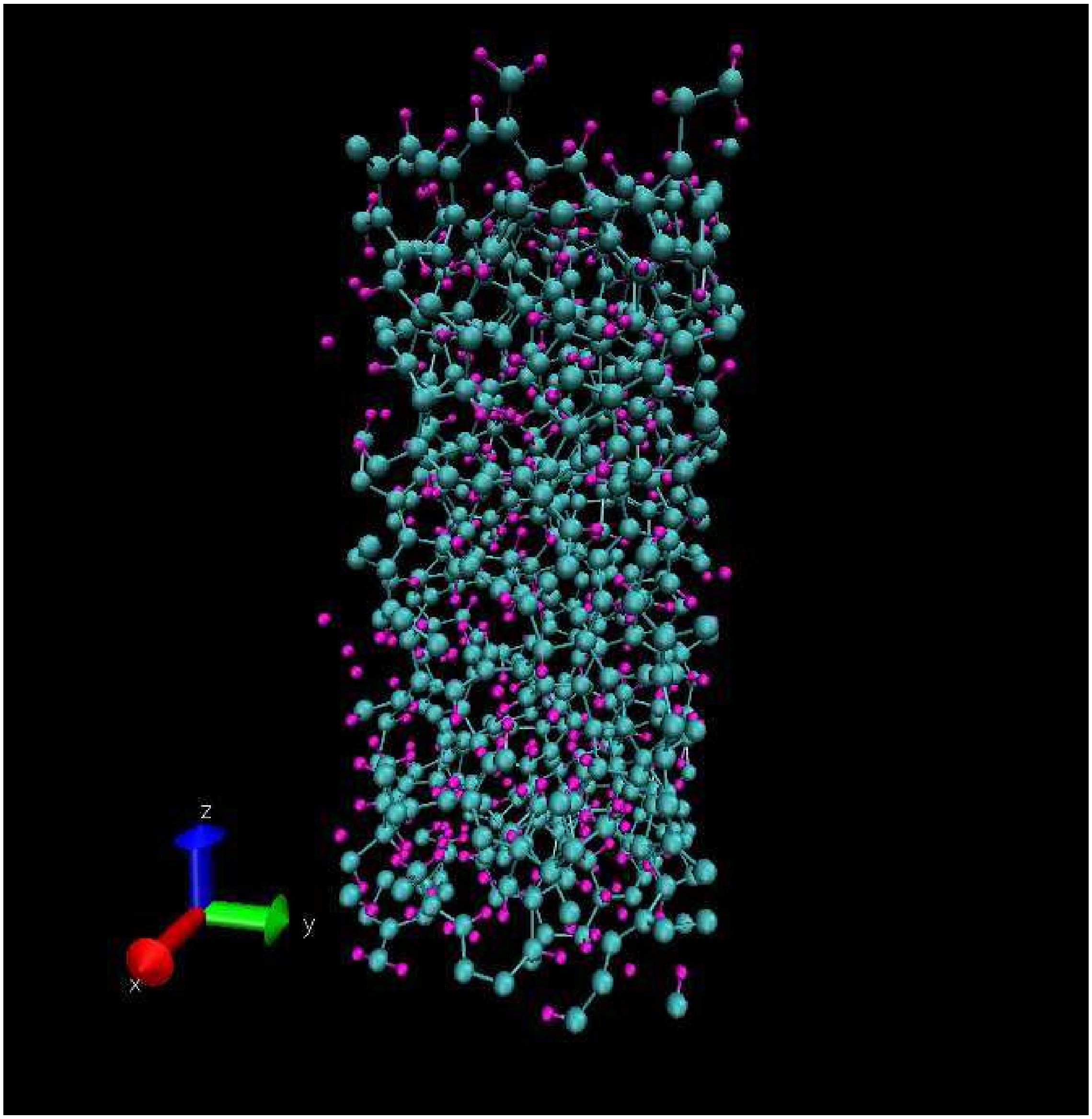

Figure 3.1: The sample generated by MD simulations (cyan for carbon and pink for hydrogen). Sample dimensions are 14x14x31.7Å^3

and 400. The total simulation time varied between 300 ps and 2500 ps depending on the number of H atoms. In the case of pure Ar bombardment (no H atoms were incident), the time between Ar atoms was kept 300 ps in order to compare with other simulations which will be discussed in the subsequent sections. For the rest of the simulations discussed in this chapter, the H/Ar ratio was kept at 50.

3.2.2.2 Energy Dependence

In these simulations, we have studied the energy dependence of erosion for a fixed H/Ar ratio of 50 at 300 K sample temperature. The energy of Ar atoms was varied between 25 eV and 200 eV. The upper limit of the energy is chosen in such a way that the range of incident Ar atoms will not exceed the sample size in Z-direction (28 Å in Z-direction). The incident Ar atoms were tracked for 5 ps to 20 ps depending on the incident energy. The simulation procedure was similar to that in the flux ratio dependent.

3.2.2.3 Angle Dependence

The angle dependent simulations were done at 300 K for 100 eV and 150 eV Ar energy with H/Ar ratio at 50. The angle of incidence of Ar atoms varied between 0° to 80° with respect to the surface normal at various surface locations. The simulations were similar to those of energy dependent case.

3.2.2.4 Temperature Dependence

The temperature dependent simulations were performed for a range of temperatures from 100 K to 800 K for the incident Ar energy of 100 eV at normal incidence at random surface locations. The simulation procedure was similar to that of the angle dependent case.

For comparison two additional sets of cumulative bombardment runs were also performed with only Ar atoms and with only H atoms for all the four cases described above. The time between successive impact events was kept the same as for the co-

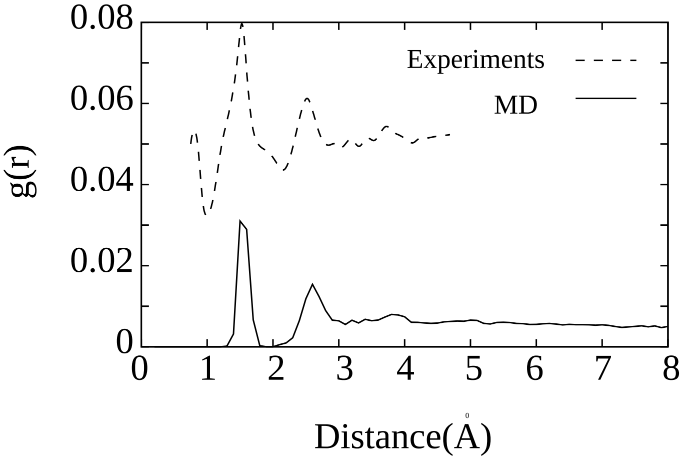

Figure 3.2: Radial distribution function derived from neutron scattering experiments compared with RDF of MD generated sample.

bombardment simulations.

3.3 Results

The amorphous nature of the sample was characterized by the radial density distribution function (RDF) of the carbon atoms computed for the carbon network by

$$g(r) = \frac{V}{4\pi r^2 N^2} \left\langle \sum_i \sum_{i \neq j} \delta(\vec{r} - \vec{r}_{ij}) \right\rangle , \tag{3.1}$$

where V is the volume, N is the number of particles in the system, and $\vec{r}_{ij}$ is the distance between particles i and j. The data are compared with neutron scattering experiments given in Ref. (in Ref. [123] figure 1, curve 3). The RDF gives the conditional probability of finding an interparticle distance of r. Thus $g(r)$ provides a measure of local spatial ordering (Fig. 3.2). The location of the peaks indicating the next-neighbour (1.5 Å) and second-next-neighbour (2.8Å) distances are in good agreement with the experimental data. The structure below 1 Å in the measurement is due to H_2 molecule contributions present in the experimental data since the experimental RDF is given by the superposition of contributions of all atom pairs (C–C, C–H, H–H). This is also the reason for the shoulder at 2 Å. RDF was computed after bombardment and the difference with the initial RDF lies within the statistical fluctuations. This confirms that the cumulative bombardment did not alter the structural integrity of the sample.

Table 3.1: Film properties before and after bombardment simulations of 300 K sample after 45° by 150 eV Ar atoms. The quantities in brackets are for the upper half (14 Å) of the sample. The displayed values are averaged over all 10 simulation sets. N_C and N_H are the numbers of C atoms and H atoms, respectively. The bond distribution gives the number of C–C coordination (for details see text).

Sample	N_C	N_H	$N_\mathrm{H}/N_\mathrm{C}$	Bond distribution			
				1C	2C	3C	4C
Initial	510	315 (177)	0.618 (0.616)	8	169	267	66
H alone	510	346 (208±1)	0.678 (0.725)	8	169	269	64
Ar alone	499±3	292±4 (154)	0.584 (0.559)	12±1	196±2	260±1	31±1
Ar|H	484±3	323±4 (190)	0.667 (0.715)	16±1	187±2	241±2	39±2

The key properties of the sample for 150 eV Ar bombardment at 45° angle of incidence are shown in Table 3.1. N_C and N_H are the numbers of 'active' carbon and hydrogen atoms respectively, i. e. all atoms except those fixed at the bottom 3 Å of the sample. The C–C coordination is the number of carbon atoms attached to any given carbon atom in the sample. From here onwards, this is referred as carbon coordination.

3.3.1 H/Ar Ratio Dependence

Table 3.2: The erosion yield as a function of H/Ar flux ratio for Ar energy of 100 eV and thermal H atoms

H/Ar Ratio	Erosion Yield
0	0.057 ± 0.035
5	0.21 ± 0.077
50	0.45 ± 0.0564
100	0.43 ± 0.11
400	0.44 ± 0.14

The erosion yield as a function of incident H to Ar flux ratio for 100 eV Ar bombardment at 300 K sample temperature is shown in Table 3.2. The yield showed a steady increase with flux ratio upto 50 and saturated afterwards. The yield for pure physical sputtering is 0.07 and 0.45 for the flux ratio values of 0 and 50 respectively. There was no significant increase in the erosion yield for H/Ar greater than 50. At this point further additions resulted in either reflection or replacement of the already added H atoms. This did not change the number of added H atoms to the sample.Further simulations revealed that the saturation level is approximately same for Ar energies of 100 eV and 150 eV. This is why all other simulations were performed for an H/Ar ratio of 50.

3.3.2 Energy Dependence

The energy dependence of the erosion yield of both Ar|H and Ar-Only simulations is shown in Fig. 3.3. The yield increased with incident Ar energy for both the cases and no erosion was observed in the H-only case. For energies less than 100 eV the difference in yield between pure physical sputtering and co-bombardment is less and with the increase in energy ($\geq$ 100 eV), the difference also found to be increasing. At 200 eV, the pure physical sputtering yield is 0.45 and the co-bombardment yield approaches 1.

3.3.3 Angle Dependence

The angular dependence of the yield for both Ar-only and Ar|H cases is shown in Fig. 3.4. Here also, no erosion was seen for pure H bombardment simulations. The sputtering yield dependence for Ar-only simulations roughly follow the well known sputter yield curves computed with binary collision codes like TRIM with a maximum around 70 degrees [17]. The corresponding MD simulations yielded less pronounced peaks due to the non-negligible influence of surface roughness, which enhances the erosion yield at any angle [124]. However, it can be seen that the erosion yield for Ar|H case is higher than the pure physical sputtering yield (Ar-only) for the whole range of angles.

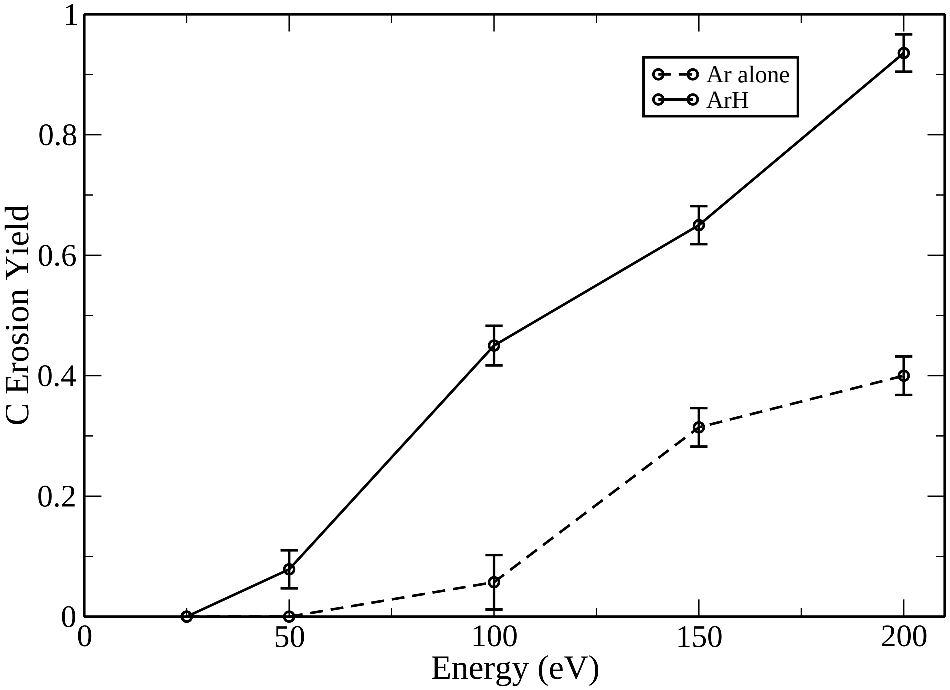

Figure 3.3: The erosion yield as a function of incident Ar energy for Ar|H and Ar only case. The hydrogen alone case does not show any erosion at 300 K.

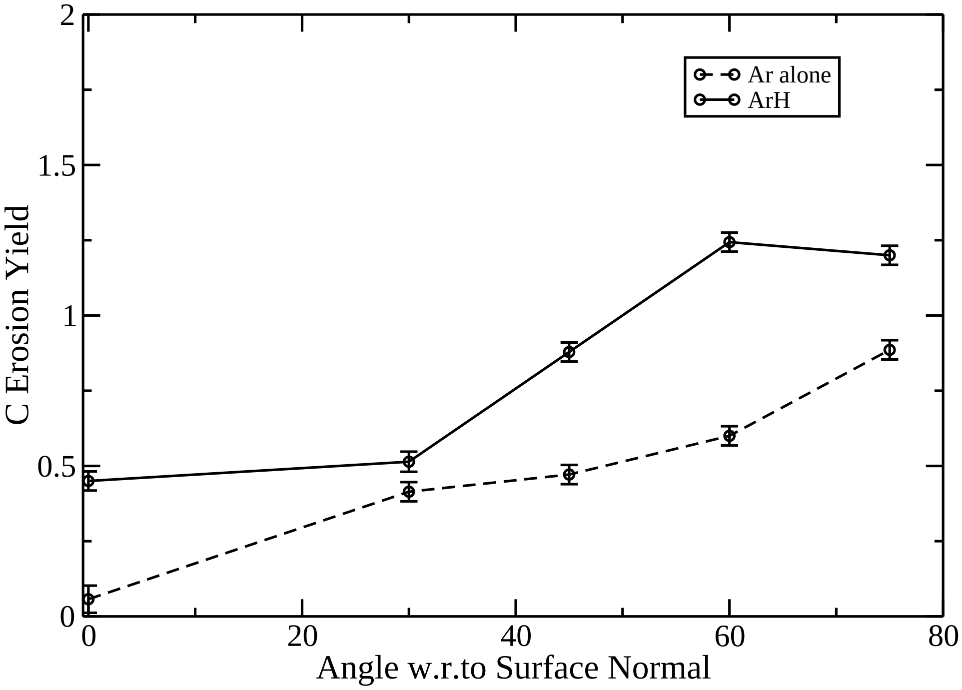

Figure 3.4: The angle of incidence of 100 eV Ar for both Ar|H and Ar only case.

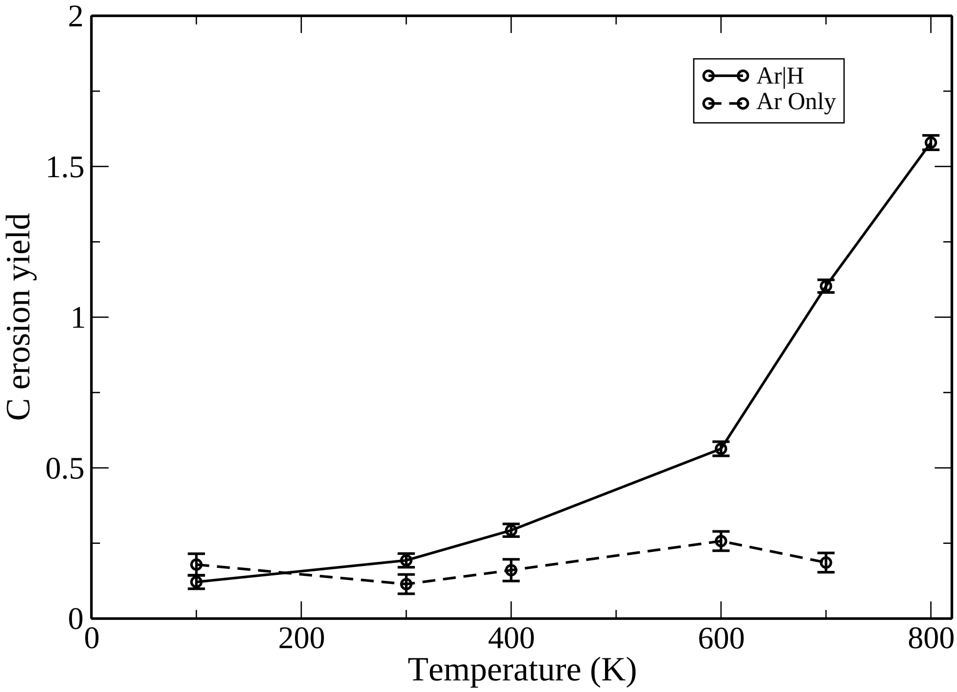

Figure 3.5: The temperature dependence of erosion yield in both Ar|H and Ar only case. There was no significant erosion in the case of H only simulations.

3.3.4 Temperature Dependence

The temperature dependence of the erosion yield is shown in Fig. 3.5. The erosion yield steadily increased with the sample temperature in the case of Ar|H simulations, whereas it was more or less constant in the Ar-only case. The absolute yield in the co-bombardment case is a factor of 3 higher for high temperatures ($\geq$ 600 K) than the pure physical sputtering case. No erosion of C atoms was observed in the H-only case.

3.4 Discussion

In all the simulations we have observed an enhanced erosion yield when additional hydrogen atoms were supplied. Thus, the mechanism of erosion should be different than pure physical sputtering and chemical erosion. In the subsequent section we discuss a mechanism for the enhanced erosion due to the energy synergism.

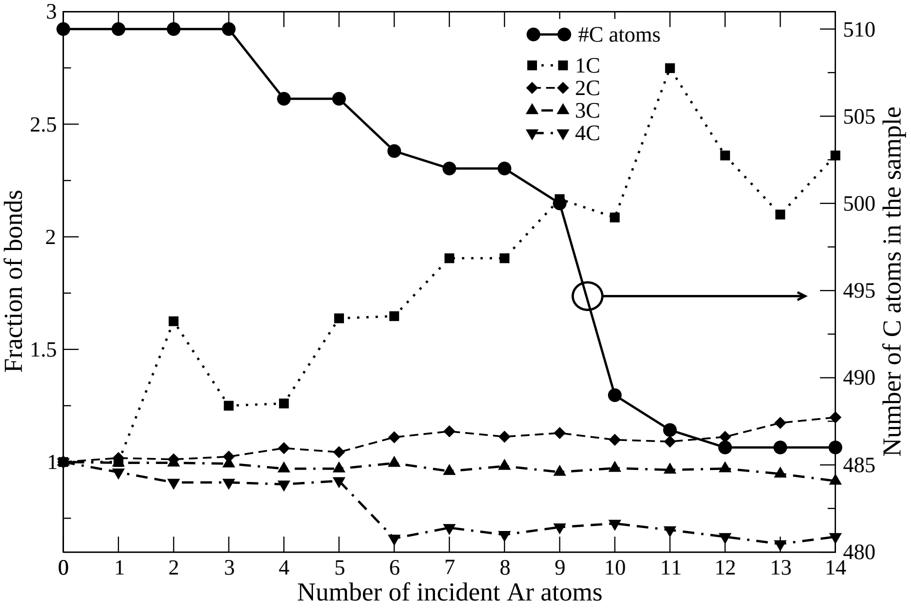

Figure 3.6: C–C coordination and number of carbon atoms in the sample as a function of the number of Ar impact events in the Ar|H case. The C–C coordination is normalized to the number of carbon atoms in the sample after each Ar impact and rescaled such that their initial values are 1.

3.4.1 Mechanism of Erosion

The process of erosion can be understood as follows: Ar atoms create open bonds within their penetration range (mean range ≈ 8Å) resulting in the formation of linear hydrocarbon chains. This can be confirmed from the bond distribution of carbon atoms within the sample (see Fig. 3.6). The fractions of singly and doubly coordinated atoms are increased at the expense of 3-fold and 4-fold coordinated atoms, which is a clear indication of bond breaking. The damage created is mostly confined to the top layers, as shown in the depth profile of the displaced atoms (Fig. 3.7), which is in good agreement with TRIM.SP calculations [17].

The open bonds thus formed on the top layers are passivated due to hydrogen bombardment in the case of the Ar|H simulations, resulting in hydrogen-rich upper layers. This can be seen from the H/C ratio of the top layers of the film which is given in Table (3.1) and Fig. 3.8 for both the Ar-alone and Ar|H cases.

The change in the surface structure of the film due to additional hydrogen after 12 Ar impacts can be seen from Fig. 3.9. In the case of pure Ar bombardment,

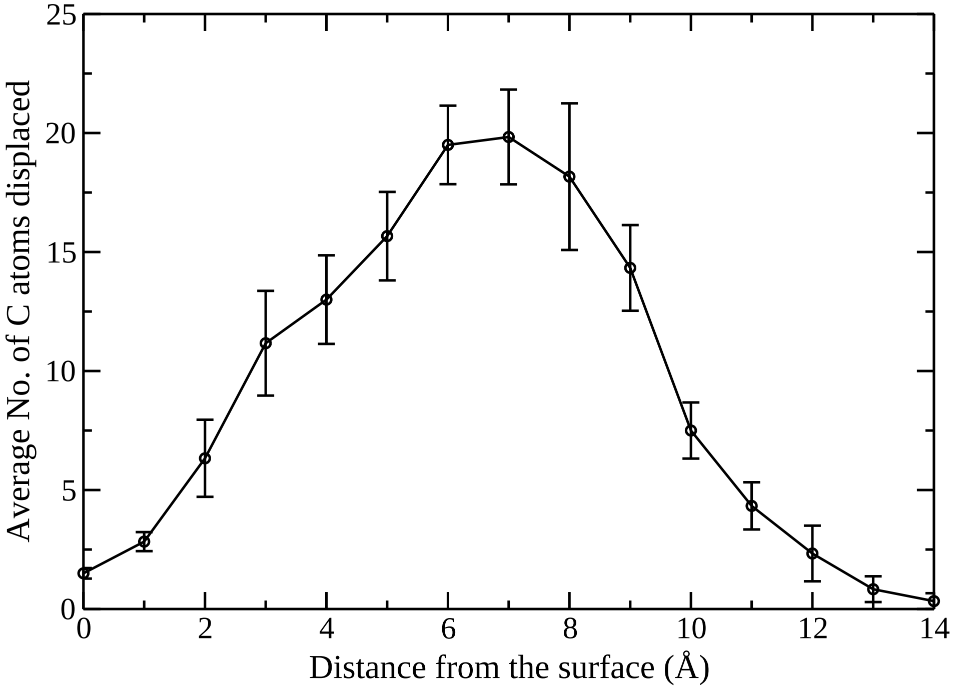

Figure 3.7: The depth profile of displaced C atoms due to 150 eV Ar bombardment per simulation set (14 Ar impacts).

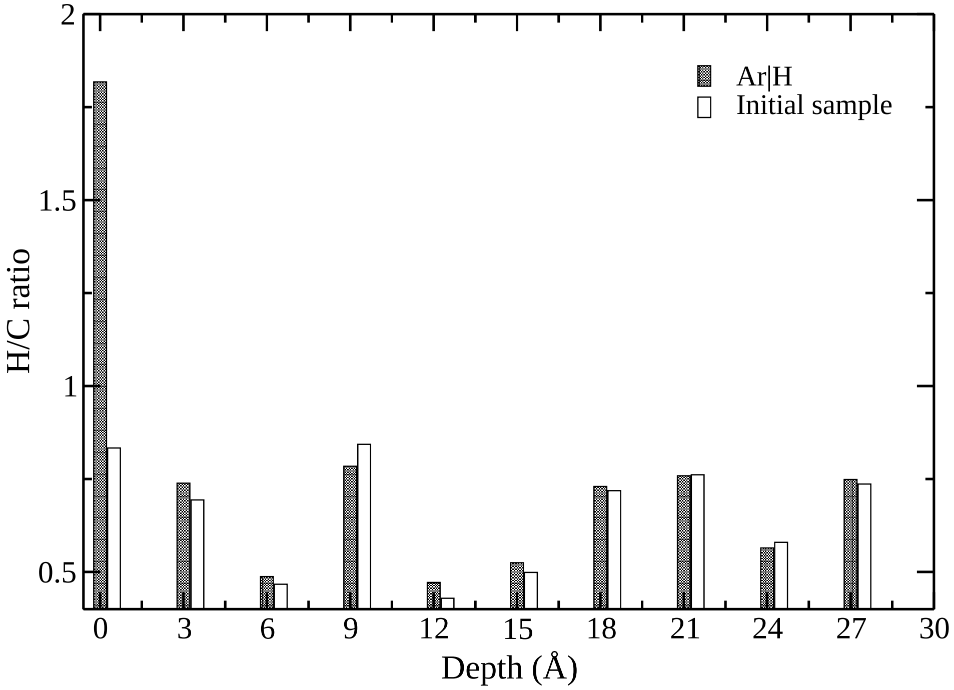

Figure 3.8: Average H/C ratio of the sample before and after one Ar|H simulation cycle.

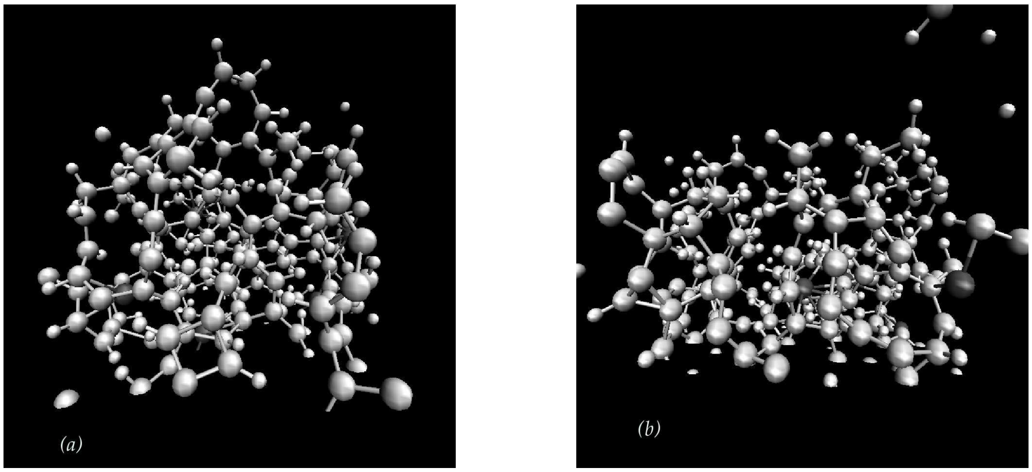

Figure 3.9: The surface structure after 12 Ar impacts: (a) Ar-only case, (b) Ar|H case. Representation of sample atoms: hydrogen by small light grey spheres, argon by dark grey spheres, carbon by light grey spheres.

long chains of carbon atoms get closed via re-attachment at some other open bond locations. However, the screening effect of hydrogen atoms in Ar|H case makes the closing of long hydrocarbon chains difficult even if there are available binding sites. Although this effect is hard to quantify it is clearly visible in the simulations. The steric repulsion arising between H atoms connected to different C atoms keeps the chains predominantly linear in the case of Ar|H simulations (see Fig. 3.6).

The subsequent Ar impacts cause further breaking of C–C bonds resulting in the detachment of unsaturated molecules from the sample. Thus we call this mechanism ***Hydrogen Enhanced Physical Sputtering (HEPS)***. The bond breaking happens either by direct bombardment or by the knock-on atoms. Since the top atoms of the linear carbon chains are covered with hydrogen in the Ar|H case, the broken molecule fails to re-attach to any other available bonding site. Hence, the unsaturated molecule comes out of the sample. The schematic of the erosion process is shown in Fig. (3.10).

The overall picture of erosion can be further understood from the depth profiles of bombarded argon and hydrogen within the sample. Fig. 3.11 shows the profiles of Ar and H along with the eroded carbon atoms from the sample. It can be seen that, most of the eroded carbon atoms were from the common range of both hydrogen and

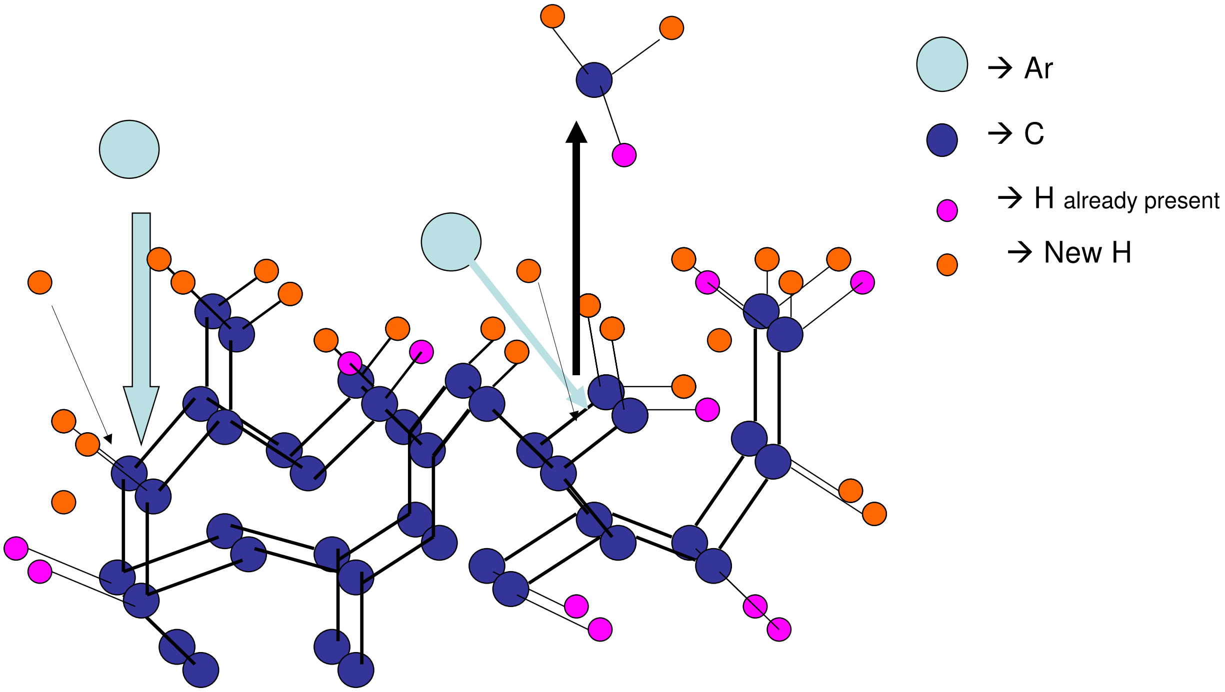

Figure 3.10: Schematic of mechanism of erosion: Hydrogen Enhanced Physical Sputtering (HEPS).

carbon atoms. This confirms the combined effect of bond breaking and passivation in the erosion process.

The unsaturated molecule emission can be confirmed from the analysis of the sputtered species. None of the emitted carbon atoms were CH_4 in either the Ar-alone or Ar|H simulations. The erosion histogram (Fig. 3.12) shows the fraction of different ejected hydrocarbon radicals normalized to the total number of events. Though, the fraction of radicals having more than 4 carbon atoms is low, the C_2 and C_3 molecules are eroded only if additional hydrogen is present. This is in agreement with the existing results for co-bombardment simulations performed with low energy noble gas ions and hydrogen atoms (5 eV and 10 eV) on a-C:H films [125].

The role of momentum transfer processes in the erosion can be clearly understood from the kinetic energy distribution of the eroded particles given in Fig. 3.13. It can be seen that the energy of the particles (0.5 eV to 2 eV) is well above the thermal range. The high energy tail in the Ar|H simulations is due to the more pronounced occurrence of the loosely bound carbon atoms.

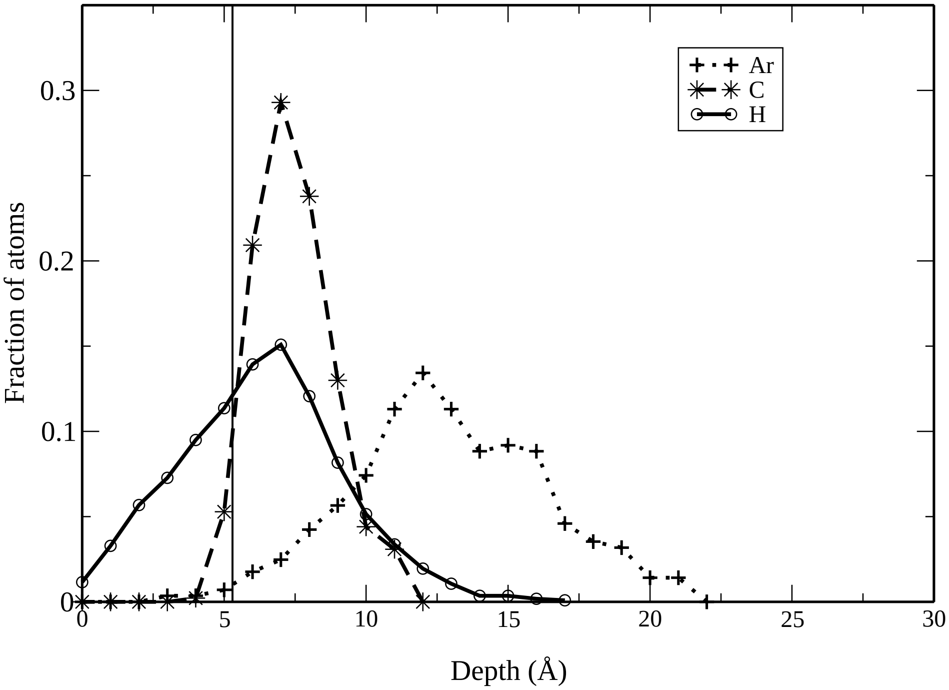

Figure 3.11: Distribution of implanted Ar and H projectiles and the origin of eroded C atoms within the sample in Ar|H simulations for 150 eV Ar energy. The vertical line indicates the initial surface.

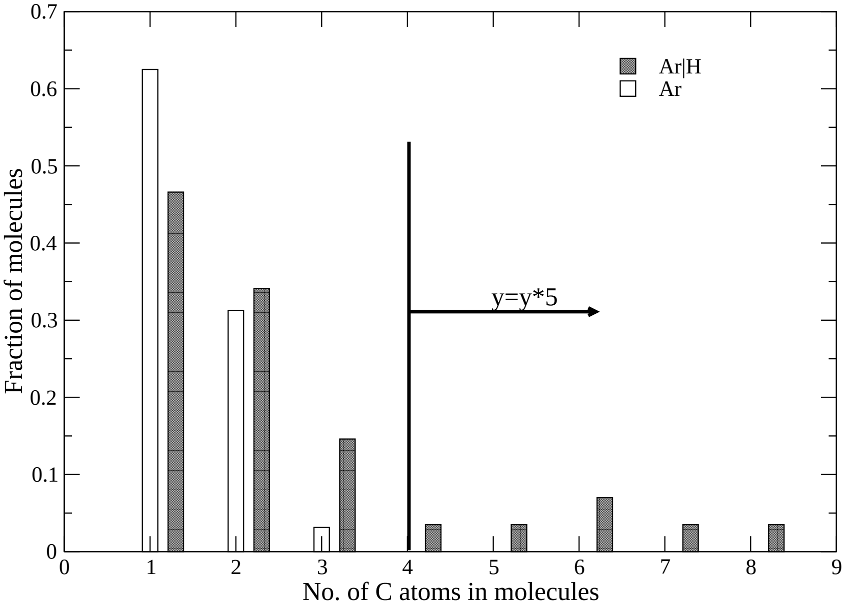

Figure 3.12: Distribution of the number of carbon atoms in the sputtered molecules in both Ar only and Ar|H case for 150 eV Ar bombardment at 45°angle of incidence w.r.to the surface normal at 300 K sample temperature. Beyond 4, the y values are multiplied by 5 to make it visible.

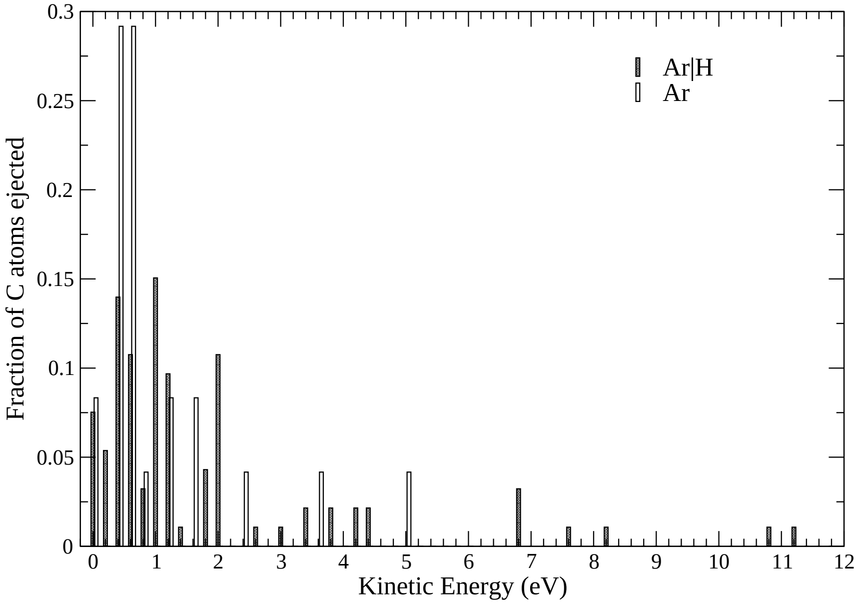

Figure 3.13: Energy distribution of the sputtered carbon atoms for 150 eV Ar bombardment at 300 K. The high energy tail in the Ar|H case indicates the increased fraction of less coordinated C atoms.

The typical time for molecule ejection is plotted in Fig. 3.14, which shows that the erosion is a fast process. All the molecules were ejected within 5 ps after the Ar impact. A closer inspection of the emission time reveals that most of the smaller hydrocarbons (C_1H_y) were ejected within 1 ps after the Ar bombardment. Most of the larger molecules were eroded at later times ($>$ 2.5ps), contributing to the high fraction of eroded carbon atoms in the case of Ar|H simulations. In the Ar-alone case, the absence of molecules with more than three C atoms (see Fig. 3.12) prevents the occurrence of any late emissions.

The role of momentum transfer processes is also supported by the angle dependence of the yield (3.4). It can be seen that the shape of the curve roughly follows the shape of pure physical erosion with an enhanced erosion yield for all angles.

The chemical and momentum transfer effects involved in the erosion process thus can be clearly distinguished. The ejection of C_xH_y radicals is entirely a momentum transfer effect. It is confirmed that the final step of erosion in the present scenario is the physical sputtering. This is also supported by the observations of *J. Marian et. al*, where the erosion of unsaturated radicals were reported from a-C:H layers

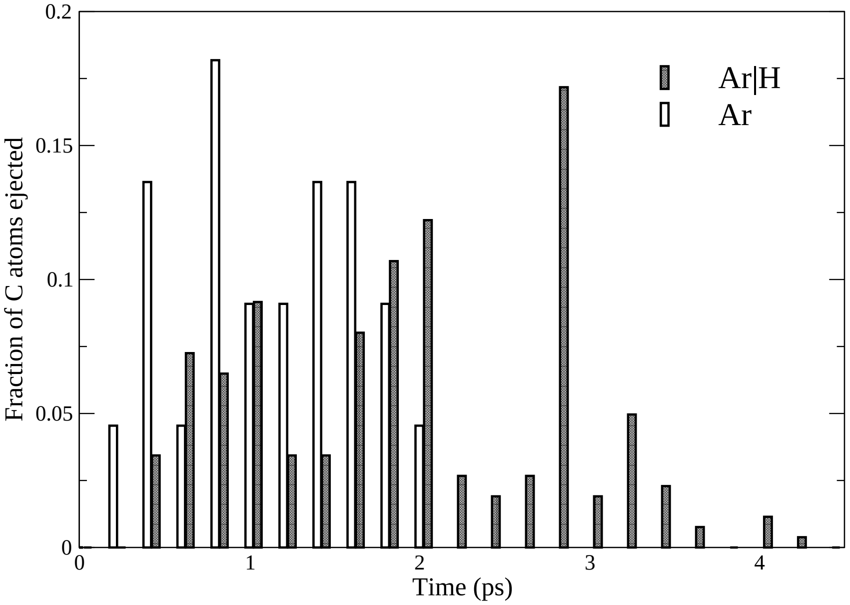

Figure 3.14: Histogram of the emission time of the eroded carbon atoms after 150 eV Ar impact at 300K. Most of the larger molecules were eroded at a later time (>2.5 ps) contributing a high fraction to the number of carbon atoms.

due to 100 eV deuterium ion bombardment [58].

However, the steric repulsion arises from the excess hydrogen on the surface in our simulations is purely chemical in origin and is responsible for the increased sputtering yield. This mechanism implies that the H/Ar-flux ratio is one of the key quantities. If the H/Ar-ratio is very low, the broken C–C bonds created by the energetic Ar atoms cannot be saturated and the additional steric effect is strongly suppressed. Therefore at low H/Ar-ratios the sputter yield should be close to the pure physical sputter yield. The presence of hydrogen results in the reduction of C–C co-ordination which effectively shifts the threshold energy for the sputtering to lower values. This increases the erosion yield. If the H/Ar-ratio is high enough to saturate the broken C-C bonds with hydrogen then a further increase should exhibit no effect on the sputter yield (see Table 3.2).

3.4.2 Energy Dependence of Erosion

The energy dependence of the erosion can be understood in the framework of the above discussed mechanism. The damage increases with the Ar energy and the

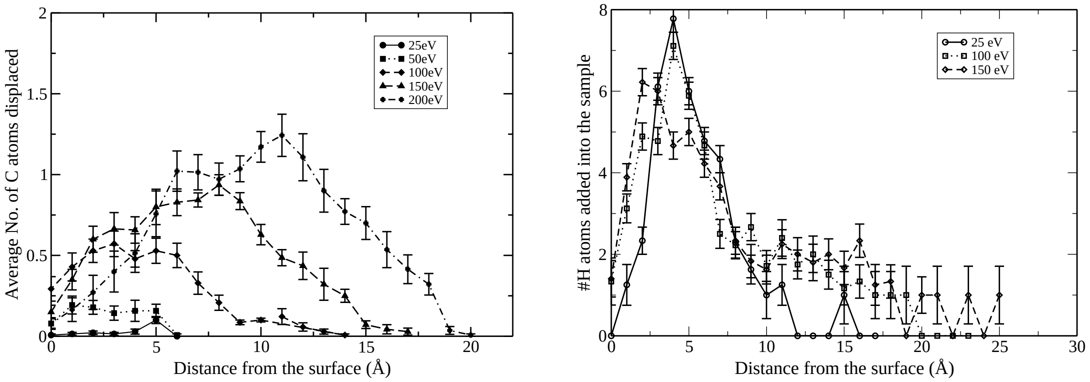

Figure 3.15: (left) Damage created in the sample as a function of incident Ar energy, (right) added H profile within the sample as a function of incident Ar energy

incident H atoms passivate the open bonds through out its penetration range. This results in a weakened C–C network and further Ar bombardment causes the erosion of unsaturated molecule from the film. This can be understood from Fig. 3.15, where the increase in the damage and the H penetration range increases with the Ar energy.

The time of erosion of molecules was within a few pico-seconds after Ar bombardment. The surface roughness of the sample was also found to increase with the energy of the bombarding atoms.

The comparison of the energy-dependent simulation results with experimental data is shown in Fig. 3.16. It can be seen that, at lower energies, the experimental yields are well above the simulated ones. The reason for the discrepancy could be two fold. At lower energies ($\leq$ 50 eV) the quantification of experimental parameters is not very accurate. Also, the surface roughness of the film after energetic bombardment could be high ($\sim$ nm) and this cannot be simulated in the small-sized MD samples. However, the simulation results qualitatively follow the shape of the experimental curve.

3.4.3 Temperature Dependence of Erosion

The changes in the properties of the film with temperature is shown in Table 3.3. This change can be attributed to the increase in C–C bond length with temperature.

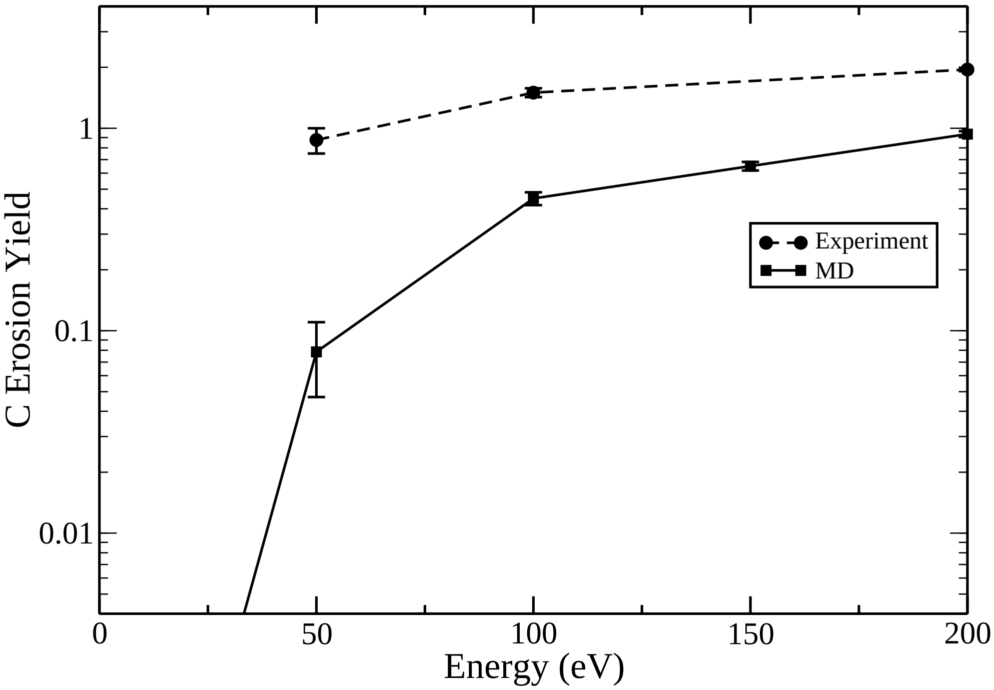

Figure 3.16: Comparison of MD results with experimental data for energy dependence.

Therefore, the calculation of the co-ordination with a fixed distance (for C–C, 2.0 Å and for C–H, 1.6 Å) shows a reduction in the number of atoms in the neighbourhood of a given C atom. This in fact shows 'weakened' C–C bonds.

Table 3.3: Sample properties as a function of temperature

T (K)	LxLyLz (Å^3)	N	ρ (gm/cc)	H/(H+C)	C coordination		
					4-fold	3-fold	2-fold
100	13.905x14.934x31.70	916	1.829	0.3755	36.0	61.7	2.1
300	13.905x14.934x31.70	916	1.829	0.3755	36.0	61.5	2.1
400	13.905x14.934x31.70	916	1.829	0.3755	35.8	62.1	1.9
500	13.905x14.934x31.70	916	1.829	0.3755	35.7	62.2	1.7
600	14.020x13.914x31.70	913	1.828	0.3735	32.2	65.9	1.2
700	14.020x13.914x31.705	913	1.828	0.3735	28.5	70.3	0.7
800	14.189x13.961x31.719	905	1.826	0.3679	25.2	73.4	0.9

The H-only simulations show that the hydrogen intake to the sample increases with the sample temperature (see Fig. 3.17). For temperatures less than 600 K, the H intake stays more or less constant and increases afterwards. The peaks of the depth profiles of the H distribution were near the surface for all the temperatures

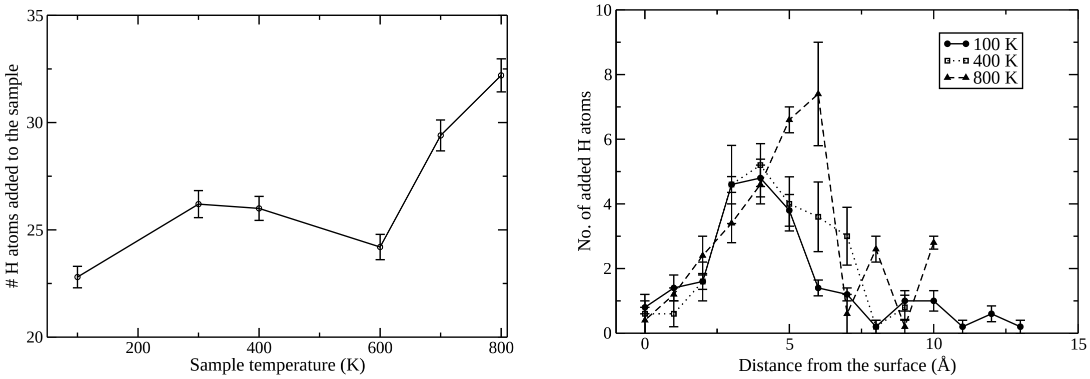

Figure 3.17: (left) The hydrogen intake to the sample as a function of the sample temperature, (right) added H profile within the sample as a function of sample temperature. Both the plots are for H-only simulations. The total number of incident H in all the cases were 650.

and the peak height at 800 K was approximately 1.5 times higher than that at 100 K. The tail of the distributions also stays more or less same for all the temperatures. Therefore, the increase in the number of added H atoms can be interpreted as the hydrogenation of the 'weakened' C–C bonds which becomes important from 600 K onwards (see Table 3.3).

The observed temperature dependence in the case of Ar|H simulations can be explained by the formation of a further weakened C–C network by bond breaking and passivation. This weakness is further amplified by the additionally added hydrogen. The subsequent Ar bombardment results in the molecule emission. However, the Ar-only simulations do not show any notable change in the erosion yield with the temperature. This can be explained as follows: with temperature, the thermal expansion of the film is small (0.019 Å in Z-direction at 800 K) and therefore, the change in the bond energy due to the change in the bond length is not significant compared to the bond breaking energy.

Even at 800 K the diffusion of H atoms into the sample was not pronounced. Considering the C–C bond energy (E) of 2 eV, the time required for breaking of C–C bonds takes on average 0.4 sec at 800 K ($t = \frac{1}{\omega}$ and $\omega = \omega_0 exp(-E/kt)$, $\omega_0 \sim 10^{13}/s$). The total simulation time was only upto 6 ns and therefore, no thermal chemical erosion is expected to be seen at these time scales.

The experiments of H induced chemical erosion of hydrocarbon films shows that the erosion yield enhances after 400 K and peaks around 650 K [19]. After 600 K, thermal erosion of H atoms increases and therefore sp^2 formation increases [19]. This reaction competes with hydrogenation and therefore depends on the flux of H atoms. At high MD fluxes of simulation ($\sim 10^{30}$ cm^{-2}s^{-1}), thermal H emission does not happen effectively and therefore the erosion peak is shifted towards higher and higher temperatures.

Thus the net erosion in the experimental scenario could be the combined contribution of HEPS and thermal chemical erosion. However, in MD simulations, there is no thermal chemical erosion, due to the limitation of the simulation time. The temperature dependence can be explained as a consequence of the amplification of the inherently weakened C–C network of the sample.

3.5 Conclusions

The synergistic erosion of hydrogenated carbon films was investigated using MD simulations, which resulted in an enhanced erosion yield compared to a simple addition of physical sputtering (due to Ar ions) and chemical erosion (due to thermal H atoms). The mechanism of erosion, *Hydrogen Enhanced Physical Sputtering (HEPS)*, can be described by the following steps:

- The energetic argon ions create dangling bonds within the penetration range.
- The abundant hydrogen atoms saturate most of the broken bonds in the first few atomic layers.
- The steric repulsion which arises from H atoms bound to neighboring C atoms in the top layer prevents the re-attachment of the broken C–C bonds.
- The final release of the hydrocarbon molecule is by a physical sputtering step due to the energetic Ar atoms.

As a consequence, a variety of unsaturated molecules are eroded from the film. The HEPS mechanism is a fast surface erosion process and the time scales are in the picoseconds range. Within the total time of 6 ns of the cumulative simulations no indication of diffusion of isolated saturated hydrocarbon molecules could be detected.

The energy dependence of HEPS showed an increase with incident Ar energy. This can be explained by the increase in the damage creation (and passivation) with the increase in the energy. The temperature dependence also showed an increase in the erosion yield which can be explained by the interplay between bond breaking and passivation on an already weakened C–C network. The comparison of the dependence on incident energy of the Ar atoms in the simulations and the experiments showed a good qualitative agreement.

Among the various species eroded, the high-C radicals (C>1) can get dissociated and ionized by the edge plasma in the tokamak. Also, they can undergo wall collisions. The sticking coefficient of high energetic radicals are high and therefore can get stuck to the near-erosion regions. This may explain the hard, hydrogen-less co-deposits observed in the plasma-exposed regions of the tokamak. The low sticking, low energetic radicals such as CH_3 can undergo long range transport and reach the plasma-shadowed remote regions. The sticking properties of both low energetic as well as high energetic radicals are investigated in the next chapter (Chapter 4).

Chapter 4

MD Studies on the Interaction of CH_3

`In this chapter we discuss the interaction of methyl radicals with amorphous hydrocarbon (a-C:H) films with the help of MD simulations.`

4.1 Introduction

In the previous chapter, we have shown that the chemical sputtering of a-C:H films can release a variety of hydrocarbon radicals into the plasma. These radicals get dissociated, ionized and transported through the plasma. During the transport, they collide with the inner walls of the tokamak and the species with high sticking coefficient such as C_2H, CH_2 *etc.*, are deposited adjacent to the erosion regions. The low sticking molecules such as CH_3 can undergo multiple wall-collisions and eventually get transported to far away locations from the active erosion regions [126]. Thus it becomes important to understand the sticking properties of CH_3 radical for modeling the growth of co-deposits in the plasma-shadowed regions.

The sticking of methyl radicals is also of importance in plasma processing experiments, where methane plasma is used for making uniform protective hard coatings such as Diamond Like Carbon (DLC) films. [64–68, 77, 127–134]. These experiments showed that methyl radicals are the most abundant species present in the plasma and the films are formed under energetic ion bombardment [68, 69]. On the other hand, the condition relevant to the plasma-shadowed regions of tokamak is mainly a vapour phase consisting of a mixture of thermal CH_3 radicals and hydrogen atoms and molecules. The films grown under such conditions are generally soft [77] and the mechanism of growth is different than the hard ones [71].

The mechanism of growth (sticking cross-section and its angle dependence) on flat, diamond surfaces was investigated by *Träskelin et.al.*, using MD simulations [91, 92]. However, the amorphous hydrocarbon (a-C:H) films are different in a number of ways: (a) a-C:H films have inherently rough surfaces, (b) the presence of a variety of atomic neighbourhoods and (c) the steric effects originating from the hydrogen atoms attached to the radicals. These factors add to the complexity of the system and hence the sticking coefficients and cross-sections are expected to be different than flat, diamond-like surface.

Thus, to understand the effect of (a), (b) and (c), we have carried out MD simulations of thermal CH_3 sticking (corresponding to 2000 K distribution) on a-C:H surfaces having four different (i) hydrogen content, (ii) number of dangling bonds and (iii) surface roughness. Though MD simulation has all the information about the system, the quantification of the number of dangling bonds is complicated due to the variety of atomic arrangements in a-C:H films. Therefore, a method based on Potential Energy Analysis (PEA) was developed to identify the dangling bonds.

Accordingly, the chapter is organized as follows: the simulations and analysis are discussed in Section (4.2). The PEA method is in Section (4.2.2). The results are given in Section (4.3) and the discussion is in Section (4.4). The energy dependent studies are given in Section (4.4.1) and the conclusions are given Section in (4.5).

4.2 Simulations and Analysis

4.2.1 Sample Creation

The simulations were carried out using HCParCas code [101] and the carbon–hydrogen interactions were modelled using Brenner potential [100]. Four types of samples were created in MD with different hydrogen content. They are: (1) MD generated initial sample, (2) hydrogenated sample, (3) hydrogen saturated sample and (4) Ar bombarded sample. The samples are so chosen such that they represent the limiting conditions of hydrogen content. The creation of the MD generated sample was similar to that described in Appendix A. The hydrogenated sample was made by bombarding hundred hydrogen atoms of 0.5 eV energy on the sample (1). The hydrogen saturated sample was created by continuing the bombardment upto 500 H atoms, within which the surface has reached the steady-state. The Ar bombarded sample was made by bombarding 14 Ar atoms on the sample (1). The number of Ar atoms are chosen in such a way that by keeping the structural integrity, the surface hydrogen content is considerably less than the H saturated surface. The density of all the samples were about 1.8 gm/cc and the temperature was kept at 300 K. The properties of the samples are given in Table 4.1.

Table 4.1: Sample properties

Sample	N_C	N_H	H/(H+C)	Surface H content
MD generated (initial)	572	341	0.373	0.495
H interacted	572	352	0.381	0.508
H saturated	572	365	0.390	0.583
Ar bombarded	572	338	0.371	0.495

The radial correlation of all the samples was evaluated using equation (3.1) and was found to be similar to (see Fig. 3.2) and thus the amorphous characteristics of the films was confirmed.

The surface structure, number of dangling bonds *etc.*, on the surfaces are calculated using Potential Energy Analysis (PEA) of the film, which is discussed in subsequent sections.

4.2.2 Potential Energy Analysis (PEA)

The method is based on the idea that the dangling bonds are the potentially attractive sites within the film. The proposed method has two parts: (a) calculation of the potential energy surface of the sample using hydrogen atom as the test particle and (b) elimination of certain sites according to the potential energy values of the neighbouring sites.

The reason for choosing H atoms is two fold: first, H atoms can only make sigma bonds with C atoms like CH_3 radicals, which is not the case for C atoms as they can have all the possible binding possibilities like sp^2 type, sp^3 type *etc.* Second, unlike CH_3 radicals, there is no orientation preferences [135] for H atoms and this makes calculations relatively simple.

The samples were binned in X, Y and Z directions and each location was defined by a unique bin index. The bin sizes varied between 0.1 Å to 1 Å and it was found that upto 0.5 Å binning, the potential energy variation is not drastic. The sample atoms were at fixed locations ('frozen') while taking the measurements. This assumption is valid as the displacement of sample atoms is not significant for thermal CH_3 bombardment. However, this does not hold for energetic radicals as the energetic radicals can alter the structure by damage creation. The test atom was kept at each bin locations (corners of the bin) and the potential energy due to the neighbouring atoms (many body interaction) was calculated. Thus, a 3D matrix of potential energy values were obtained.

The attractive potential (negative potential values) locations thus obtained may not necessarily be the binding sites for a CH_3 radical due to its larger size. Considering the steric effects it is possible to see that the sticking will happen only at those locations where the molecule can find a stable configuration (see Fig. 4.4). This immediately leads to the condition that, adjacent to a given attractive site, there must have an attractive neighbourhood at least upto next-to-next neighbours.

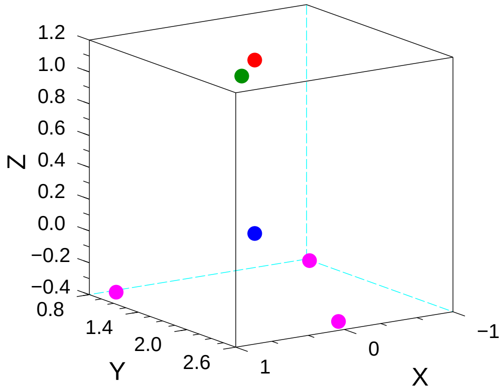

Figure 4.1: The identified dangling bond location on a methane molecule with topmost H atom removed. Blue: carbon, pink: hydrogen, red: 4^{th} H atom of methane, green: predicted dangling bond location by the algorithm

A scheme based on this concept was developed and compared with the simulation results.

The locations where potential energy is strongly attractive (PE $\leq$ -1.0 eV) is considered as the initial sites. This cut-off is chosen because C–C bond has energy $\sim$ 2 eV and therefore the incident radical has a high probability to get bound at such locations. For each such bin, if the potential energy of the top locations are repulsive then the site is rejected. Most of the resulting sites resided within a depth of 10 Å.

4.2.2.1 Testing of Algorithm

The above algorithm was tested with surfaces and molecules having known dangling bond locations. The algorithm was tested for three distinct cases. In the first case, it was tested for a methane molecule and the algorithm yielded no dangling bonds. A methyl radical in tetrahedral configuration was chosen in the second case by removing the top most H atom from the CH_4 radical. This resulted in a strongly attractive site at the fourth location of the molecule, which is shown in Fig. 4.1.

The identified dangling bond location was at a distance of 0.143 Å from the actual location. This is due to the finite size binning of the film of 0.5 Å. Thus there is an inherent uncertainty of the bin size in the location of the dangling bond. In the third case, the same molecule was inverted such that the removed hydrogen location is in the bottom. The algorithm yielded no possible binding location. This is because the C atom was exactly above the removed H atom location, which yielded a repulsive site.

4.2.2.2 Definition of the Surface

There exists no unique method for defining the surface of the amorphous film due to the inherent roughness in the atomic scale. Thus we define the surface of the film based on the potential energy, in such a way that for each X-Y coordinate, there exists a top most Z coordinate, where the absolute value of PE $\leq 10^{-5}$ eV.

The surface structures for three different films is shown in Fig. 4.2. The mean height of all the surfaces is 30.650±0.139 Å. The roughness of the surface is defined as the mean square deviation of the height and ion bombardment found to increase the roughness due to the reduced co-ordination of the C atoms (see Fig. 3.6 in Chapter 3). The properties of the surface along with the number of dangling bonds for different cases is given in Table 4.2.

Table 4.2: The surface properties for different cases.

Sample	Hydrogen content		N_{db}	Surface roughness (Å)	A (Å^2)
	H/(H+C)	H/C			
Ar bombarded	0.391	0.643	32	1.64	638.0
Initial	0.495	0.981	15	1.03	471.5
H interacted	0.508	1.03	11	1.07	507.9
H saturated	0.583	1.4	8	0.89	469.5

.

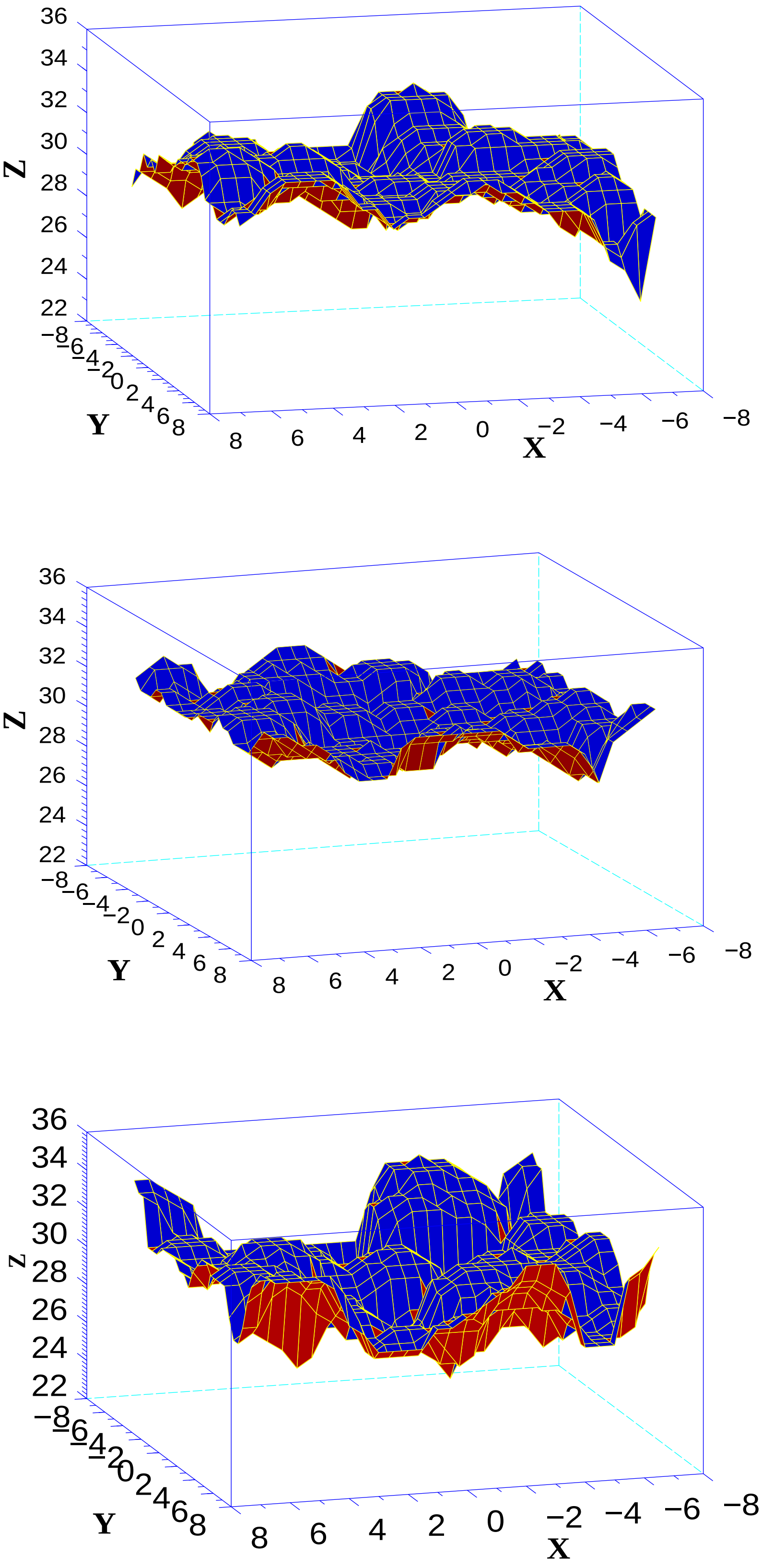

Figure 4.2: The surface structures of (top) initial sample at 300 K, (middle) hydrogen saturated sample and (bottom) Ar bombarded sample

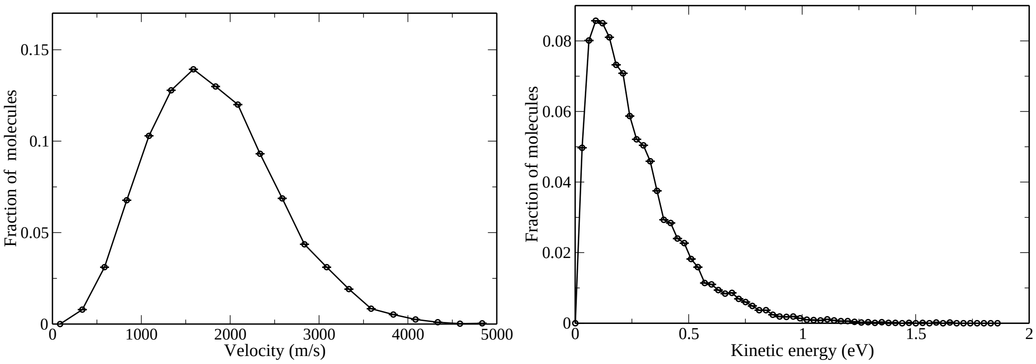

Figure 4.3: Velocity and kinetic energy distribution of methyl radicals corresponding to 2000 K

4.2.3 Bombardment Simulations

The a-C:H surfaces were bombarded by CH_3 radicals at normal incidence. The incident energy was sampled from the velocity distribution corresponding to 2000 K (thermal) as shown in Fig. 4.3.

The CH_3 radicals were created by specifying the coordinates of C and H atoms in sp^2 (planar) configuration and then relaxed afterwards for about 0.5 ps. The velocity of the molecule was specified by both a) velocity of the centre of mass (CM) of the molecule and b) velocity about the center of of mass. Ten thousand non-cumulative bombardment events were performed in all the simulations on a flat area of 144 $Å^2$ (avoiding the temperature scaling region of 2 Å at the edges in X and Y directions) indicates that each square angstrom receives typically about 69 radicals. This gives reasonably good statistics for the estimation of reaction events at the surface sites. The sample temperature was brought down to 300 K after every bombardment. The simulation was for 10 ps.

4.3 Results

We noticed mainly three types of reactions: (a) direct sticking of the radical on the surface, (b) abstraction of the bound hydrogen from the surface and (c) reflection. We also observe rare events of breaking of thermal CH_3 on the surface and followed by the reflection of CH_2 radical. The hydrogen atom from the broken CH_3 was incorporated into the sample. The sticking coefficient (η) is defined as the ratio of number of radicals incorporated (chemisorptions) to the total number of incident radicals. Table 4.3 shows the various surface reactions as function of the hydrogen content of the top layers of the film. It can be seen that most of the radicals reflected from the surface in all the cases.

Table 4.3: Surface reactions as a function of the hydrogen content of the films

Sample	H content	Events (out of 10,000)			Average Sticking coefficient
		Reflection	H abs.	Sticking	
Ar bombarded	0.391	9413	1	586	$5.86\times10^{-2} \pm 4\times10^{-4}$
MD generated (initial)	0.495	9855	14	131	$1.3\times10^{-2} \pm 9\times10^{-4}$
H interacted	0.508	9891	17	92	$9.2\times10^{-3} \pm 1\times10^{-3}$
H saturated	0.583	9980	7	13	$1.3\times10^{-3} \pm 2.8\times10^{-3}$

The sticking coefficient (η) was found to increase with the decrease in the hydrogen content of the surface. In the case of Ar bombarded surface, it is 5.86×10^{-2} which is close to the reported values on ion bombarded surfaces ($> 10^{-2}$) [74,76,136] which drops down to 1.3×10^{-3} for H saturated surface.

The number H abstraction events are found to be less for thermal radicals. In the case of Ar bombarded sample, the initial hydrogen content (0.391) was already less which explains the very low (only one) H abstraction. The number of H abstractions increases with the surface hydrogen content. However, for H saturated surface, the steric repulsion from the abundant surface bound H atoms prevents the incoming radicals from reaching the surface and consequently H abstraction drops down drastically. This also accounts for the highest number of reflections.

The snapshot of CH_3 sticking is shown in Fig. 4.4. It can be seen that the incident radical performs rotations during incorporation until all the three H atoms of CH_3 are at a distance from the surface bound atoms. We call this as the steric repulsion distance (d_{crit}) and was found to be typically around 1.6 Å.

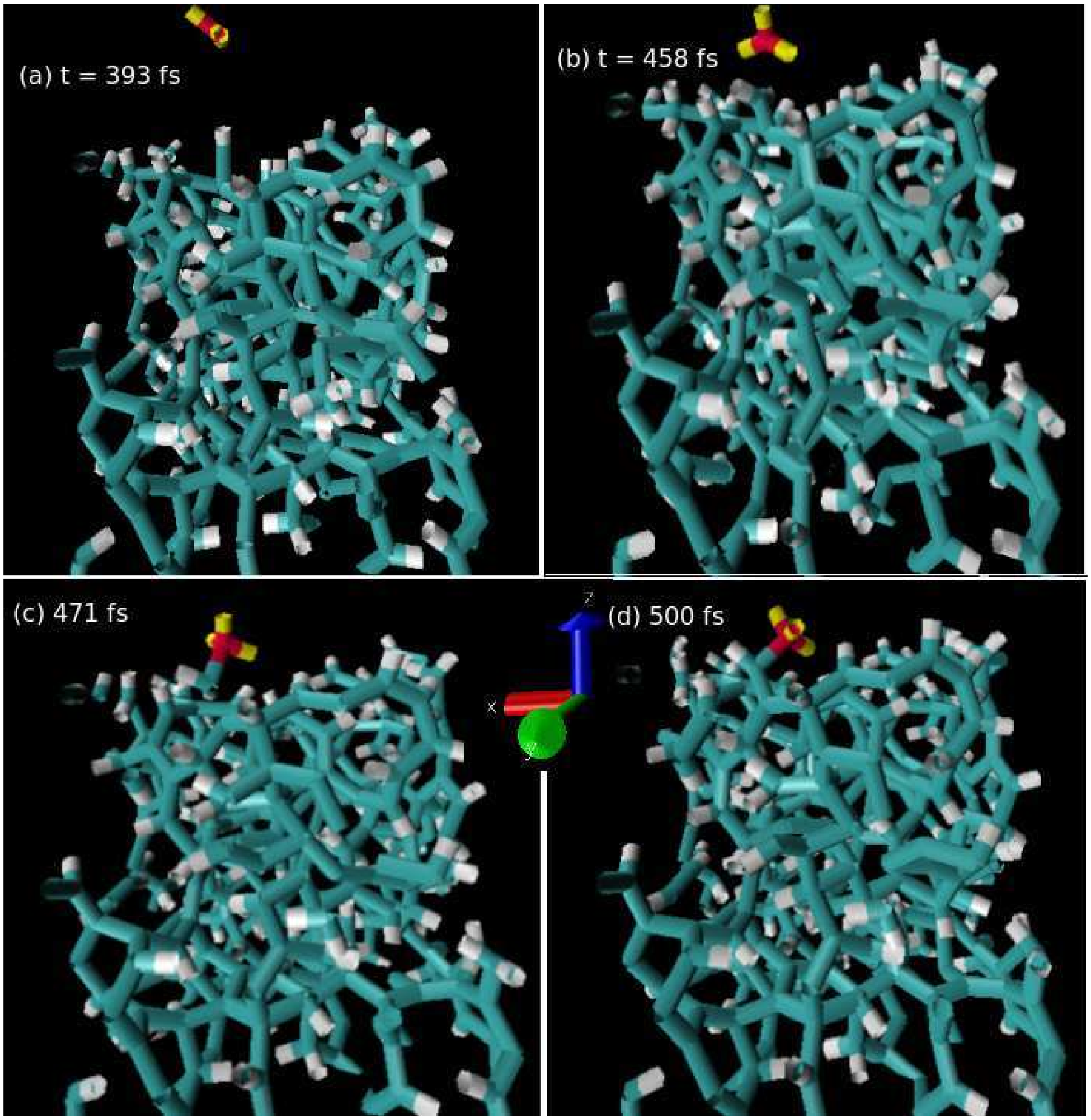

Figure 4.4: Snapshots of CH_3 sticking on a dangling bond on initial sample at 300 K. The CH_3 radicals were sampled from 2000 K distribution. The cyan and white shows the hydrocarbon film network, Red: C atom, yellow: H atoms as a part of the incident CH_3 radical.

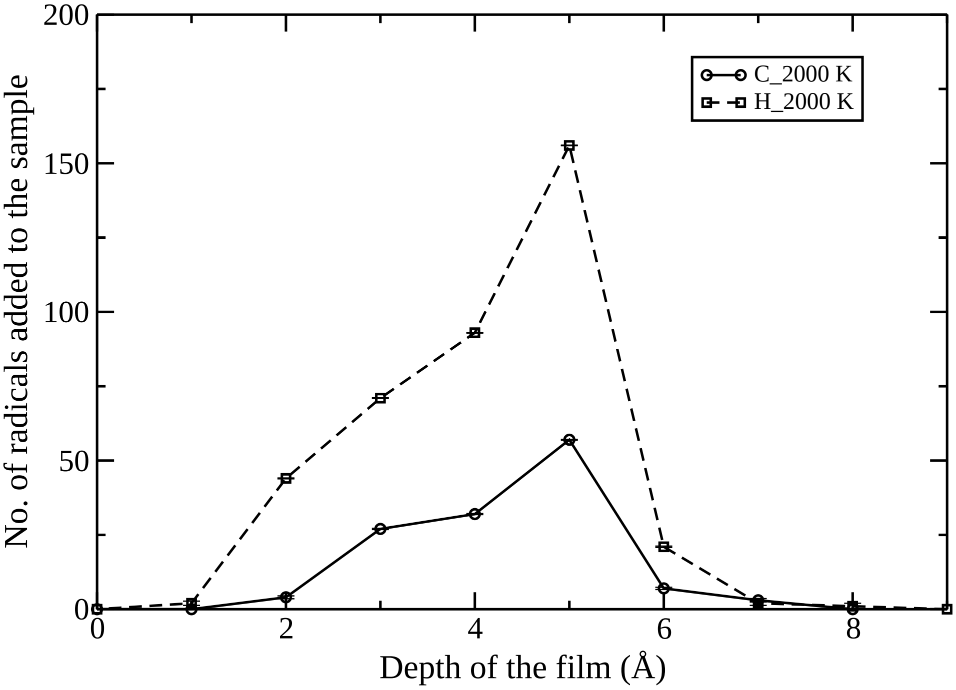

Figure 4.5: Depth profile of CH_3 radicals stuck on the initial surface at 300 K. The CH_3 radicals were sampled from thermal (2000 K) distribution.

The depth profile of the incorporated radicals on the initial surface is shown in Fig. 4.5. It can be seen that most of the radicals stuck within a maximum depth of 4 Å from the topmost atom location.

4.4 Discussion

The direct sticking on the surface dangling bonds was found to be the mechanism of growth of a-C:H films from thermal CH_3 radicals. No evidence of surface diffusion was seen and therefore, sticking can be considered as ballistic incorporation. The sticking coefficient has a striking dependence on the surface hydrogen content.

The number of chemisorbed radicals are found to increase linearly with the number of dangling bonds as described in Fig. 4.6. Infact, the ratio of filled dangling bonds to the total is about 0.375 in all the cases, which explains the linear nature of the trend.

Let N_{db} be the number of dangling bonds on a flat surface of area A_0 and σ_0 be

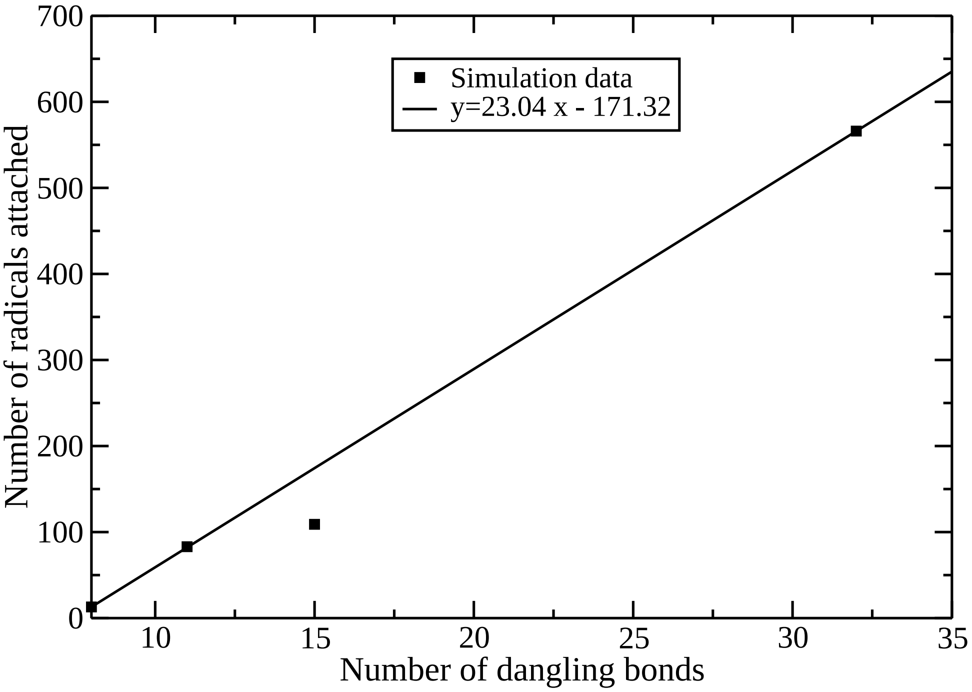

Figure 4.6: The sticking coefficient of CH_3 radicals as a function of the number of identified dangling bonds on the surface.

the cross-section then the sticking coefficient η can be defined as follows.

$$\eta = \frac{N_{db}\sigma_0}{A_0} \tag{4.1}$$

Taking the reported values of sticking cross-section of an isolated dangling bond (12 Å^2) [91], on a flat surface of area 144 Å^2, the fraction $\frac{\sigma_0}{A_0}$ is 8.3×10^{-2}. From the slope of the curve m (see Fig. 4.6), the same quantity can be derived as,

$$\eta = \frac{m}{N_{inc}} N_{db} \tag{4.2}$$

where N_{inc} is the number of incident radicals.
Comparing equations (4.1) and (4.2), $\frac{\sigma_0}{A_0} = \frac{m}{N_{inc}} = 2.03 \times 10^{-3}$.

The reduction in the quantity $(\frac{\sigma_0}{A_0})$ is due to both the steric contribution and the surface roughness, where roughness increases the surface area. The surface area scales linearly with the roughness (see Fig. 4.7). Let σ_{db}^i be the cross-section of i^{th}

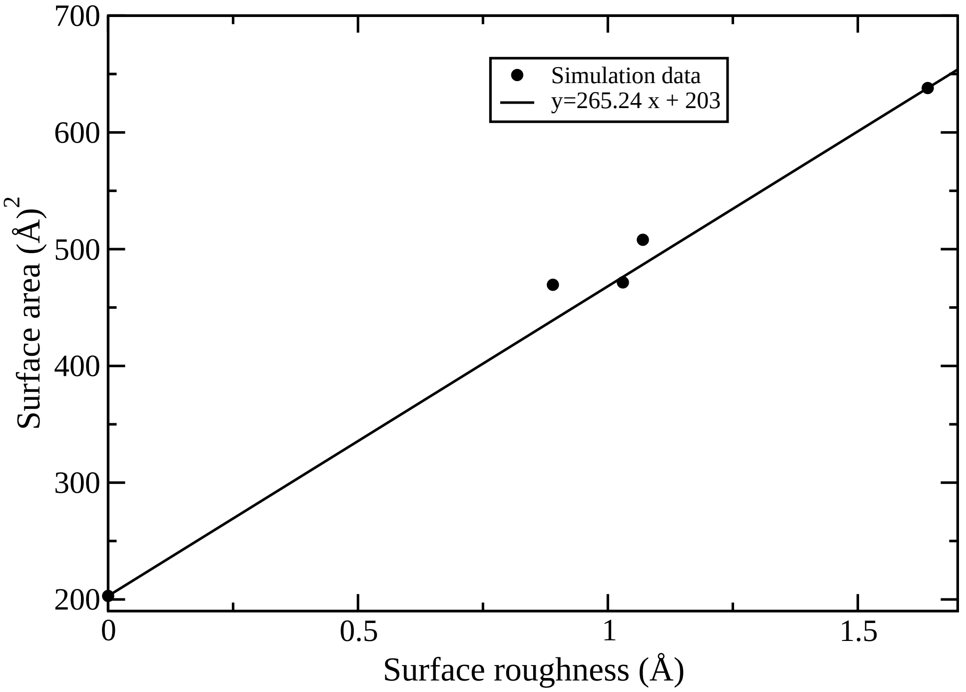

Figure 4.7: The variation of the surface area with the roughness of the surface, for sample dimension of 14 × 14.5 Å^2.

dangling bond with steric and roughness contributions, then

$$\sigma^i_{db} = \sigma_0(1 - \epsilon^i) \tag{4.3}$$

where, ϵ^i is the contribution of steric as well as roughness effects on each dangling bond which we call as screening factor. It is calculated from the number of radicals stuck on each dangling bond location. Considering 1 Å radius for a dangling bond on the surface, the cross-section π Å^2 will typically receive 216 radicals (69 per Å^2 area). Normalizing the number of radicals incorporated at each bond with 216 is the accessibility a site has, which is $(1 - \epsilon^i)$. The screening factor ϵ^i for each site is shown in Fig. 4.8. It can be seen that the sticking reduces with the screening factor.

The fractional contribution of individual dangling bonds to the total sticking coefficient of the surface is plotted in Fig. 4.9. The quantity was calculated as follows. Let N_{stuck} be the number of radicals chemisorbed on any surface amongst N_{db} dangling bonds, then for any dangling bond i, the number of radicals attached will be η_i, the 'fractional sticking coefficient', which can be written as, $\eta_i = \frac{N^i_{stuck}}{N_{stuck}}$.

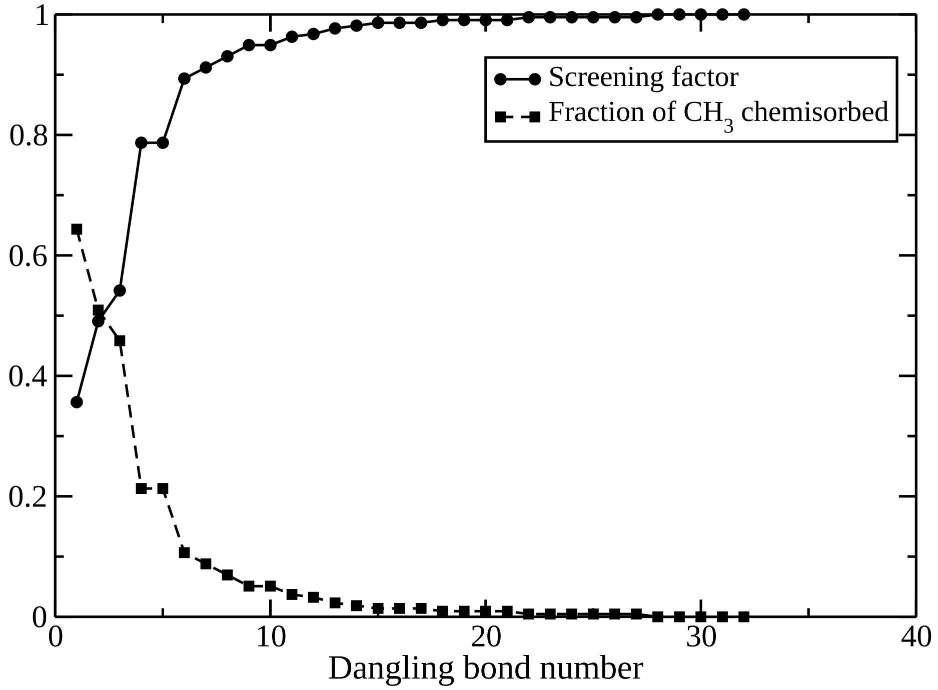

Figure 4.8: The screening factor and the number of radicals chemisorbed on dangling bonds

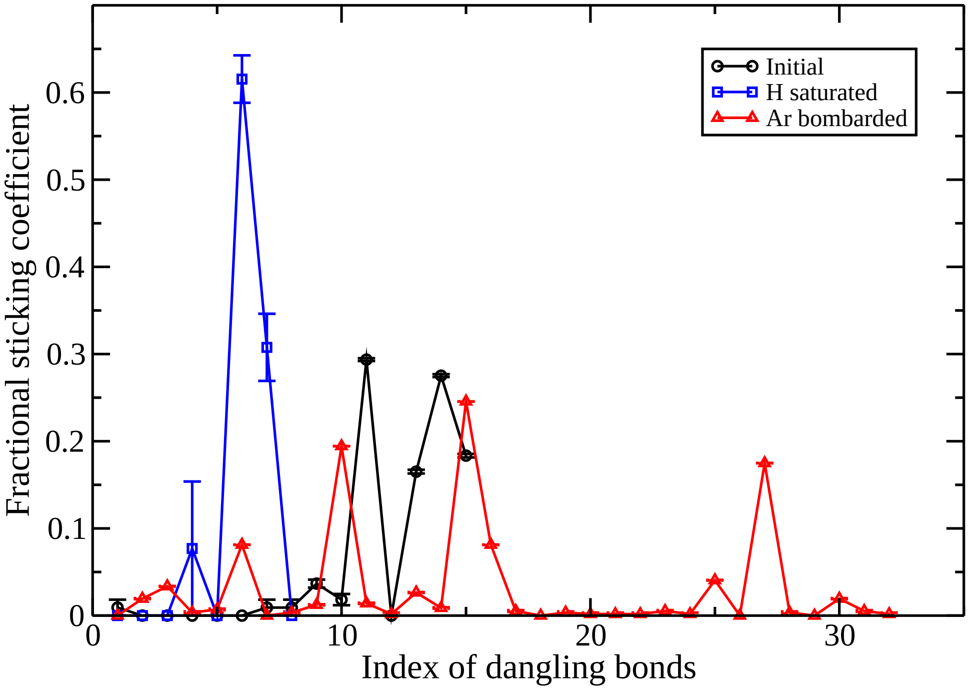

Figure 4.9: Fractional contribution of individual binding sites to the total sticking

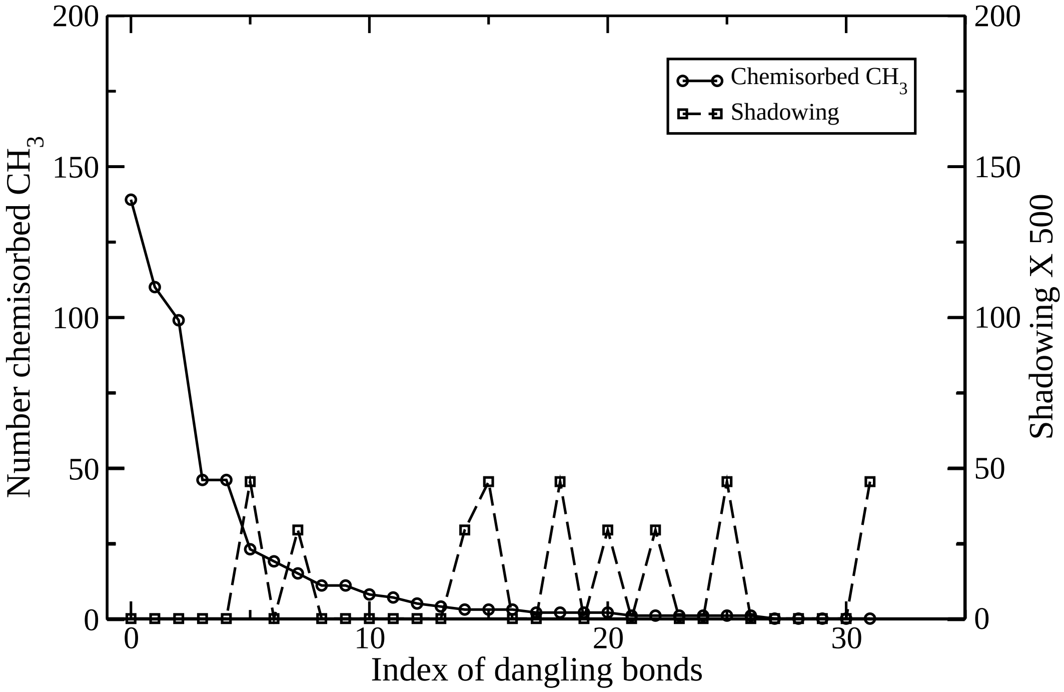

Figure 4.10: The contribution of near neighbour shadowing in the sticking of radicals for argon bombarded surface.

From the figure we can see that only certain dangling bonds are selected for the radical incorporation. In order to understand this, we have calculated the near and far-neighbour-shadowing of each site. The details of the shadowing calculation is discussed in Section (2.3.1.2 of Chapter 2). The correlation between the number of radicals chemisorbed and the shadowing of the sites is shown in Fig. 4.10 for Ar-bombarded surface. Most of the incorporation happened at the dangling bonds with no-shadowing. This indicates the importance of the local neighbourhood (from near-shadowing calculation) in the radical sticking. However, sticking was observed on sites where shadowing was non-zero. This can be because of the local re-arrangement of atoms while the radical approaches the surface, which is not captured in the present analysis. However, the number of such incorporation events were less.

The distribution of the dangling bonds for Ar bombarded surface is shown in Fig. 4.11. The broad distribution indicates a higher number of available dangling bonds in the near surface region. It can be seen that, though the dangling bond distribution extends deep into the film, the radical chemisorption is restricted to the

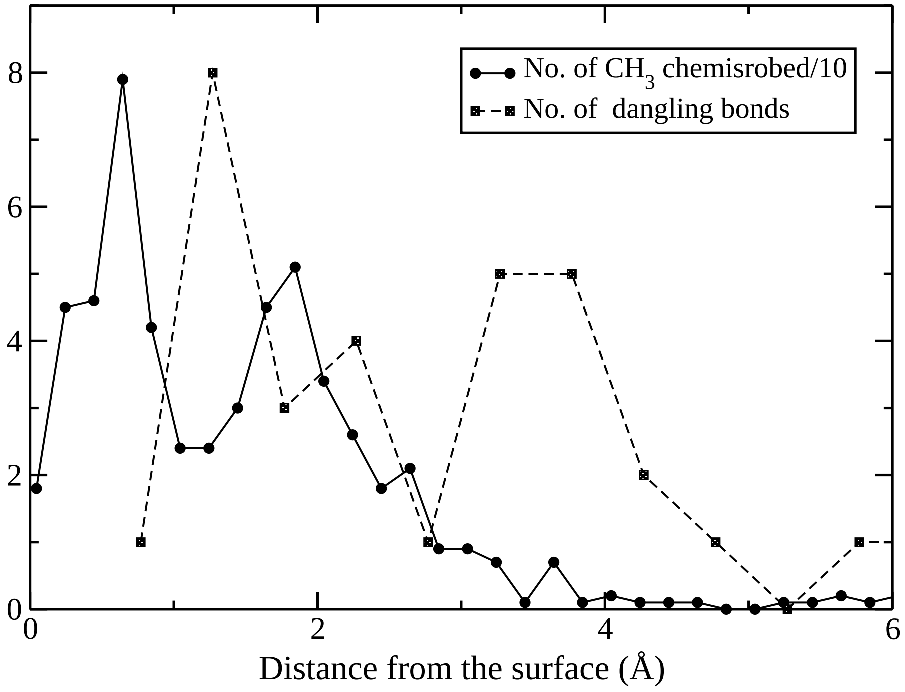

Figure 4.11: Distribution of identified dangling bonds and the chemisorbed CH_3 radicals in the case of Ar bombarded sample.

near-surface region. Along with Fig. 4.10, it can be seen that the dangling bonds on the near-surface regions are having relatively less steric contribution (less near-neighbour shadowing). Thus the radical sticking is restricted to the near surface region. The range of the CH_3 radical is found to about 2 Å from the surface, which is in agreement with the reported experimental results (0.12 nm) [77].

The comparison of dangling bond distribution for both initial as well as Ar bombarded sample is given in Fig. 4.12. It can be seen that the energetic argon bombardment resulted in the enhancement of surface dangling bonds by the depletion of surface bonded H atoms. These sites were used for the chemisorption of the radicals (Table 4.3). This explains the enhanced sticking observed in the ion-assisted growth process [76]. However, it can be seen that, the number of dangling bonds in the near surface regions (less than 4 Å) is important for the chemisorption of the thermal radicals. The steric repulsion of the hydrogen saturated surface prevents the diffusion of the radicals into the bulk of the film.

We have seen that (see Table 4.2) the surface roughness of the film increases

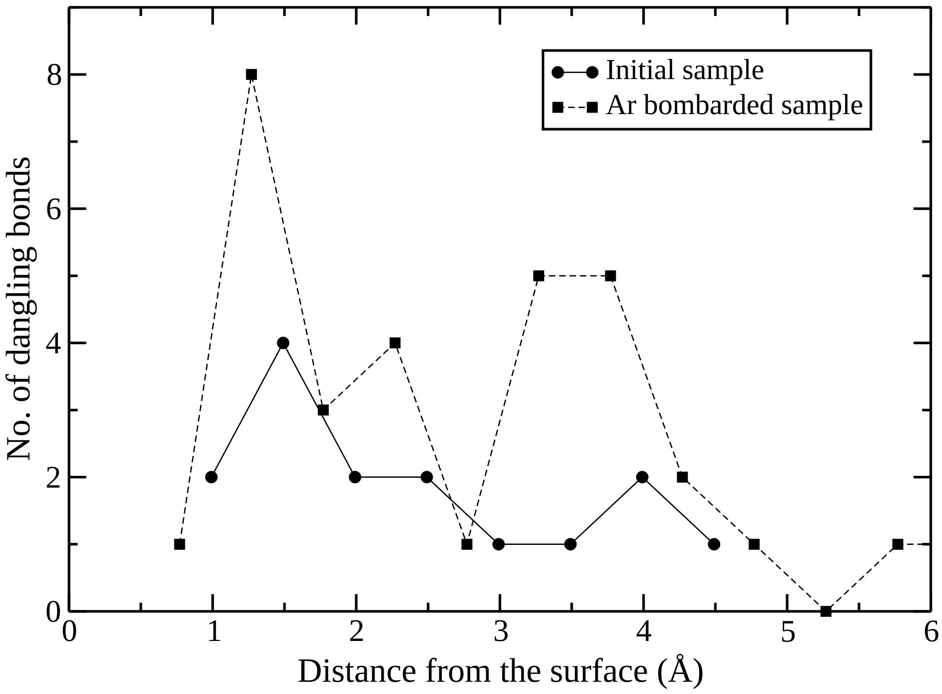

Figure 4.12: Distribution of identified dangling bonds for initial sample and Ar bombarded sample

with ion bombardment. The change in area can also contribute to the sticking on individual dangling bonds. In equation (4.3) the screening factor takes into the contribution from both steric effect and surface roughness. However, it is possible to separate these effects analytically. Let us consider a surface with N_{lump} protrusions, then the area of the surface is increased by a factor $\sum_j^{N_{lump}} \frac{\pi w_j h_j}{A_0}$, where w_j is the width of each lump of surface which either pops out of (or dips in) the mean level and h_j is the height. If we consider a surface with a cylindrical protrusion of height h and diameter w, then the addition to the surface area is equal to πwh. The area of the roughend surface (A) can be expressed as $A = A_0 \left(1 + \sum_j^{N_{lump}} \frac{\pi w_j h_j}{A_0}\right)$. The contribution from steric effects can be written as, $\sum_i^{N_{db}} \epsilon^i_{steric}$, where ϵ^i_{steric} is the contribution from pure steric effects on each dangling bond on the surface, excluding the surface area contribution.

The average sticking coefficient of the surface therefore can be written by modi-

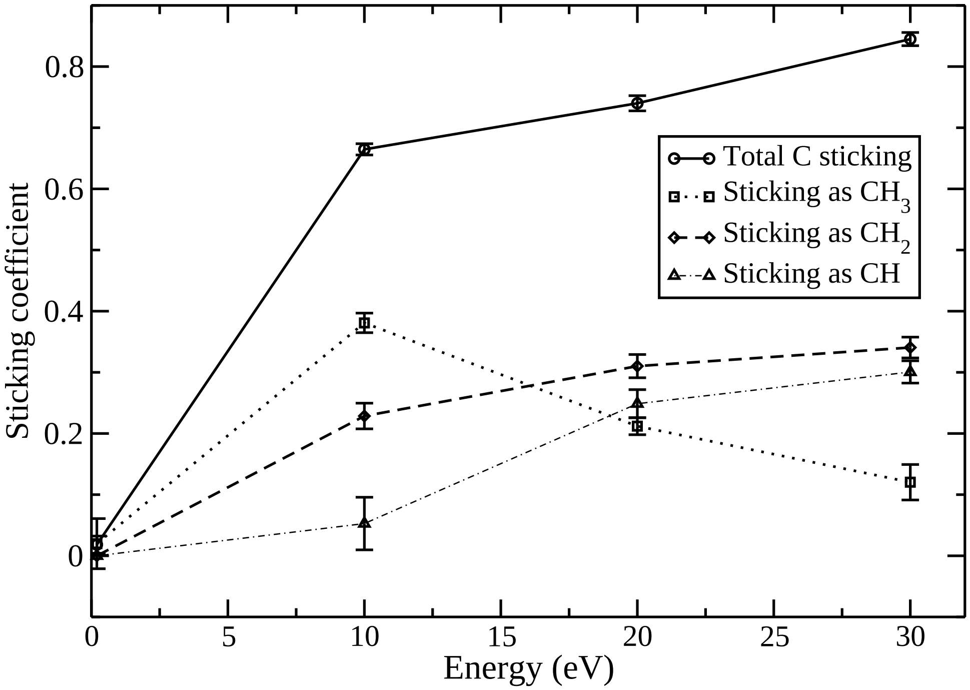

Figure 4.13: Sticking coefficient of methyl radicals as a function of incident energy.

fying the equation (4.1) as follows.

$$\eta = N_{db} \left(\frac{\sigma_0}{A_0}\right) \frac{1 - \sum_i^{N_{db}} \epsilon^i_{steric}}{1 + \sum_j^{N_{lump}} \frac{\pi w_j h_j}{A_0}} \tag{4.4}$$

In the case of an isolated dangling bonds on a flat surface, both $\sum_i^{N_{db}} \epsilon^i_{steric}$ and $\sum_j^{N_{lump}} \frac{\pi w_j h_j}{A_0}$ becomes zero and the equation (4.4) reduces to (4.1). In reality, it is difficult to separate both these effects and what we measure is the combined effect of both for the given surface (the sum of screening effect: $\sum_i^{N_{db}} \epsilon^i$).

4.4.1 Energy Dependence

In order to understand the energy dependence of CH_3 sticking we have carried out simulations at 10 eV, 20 eV and 30 eV incident energies of CH_3 radicals at 300 K sample temperature. The MD generated initial sample was used for the study. The important results from the study are presented below.

The energy dependence of the sticking of methyl radicals is shown in Fig. 4.13.

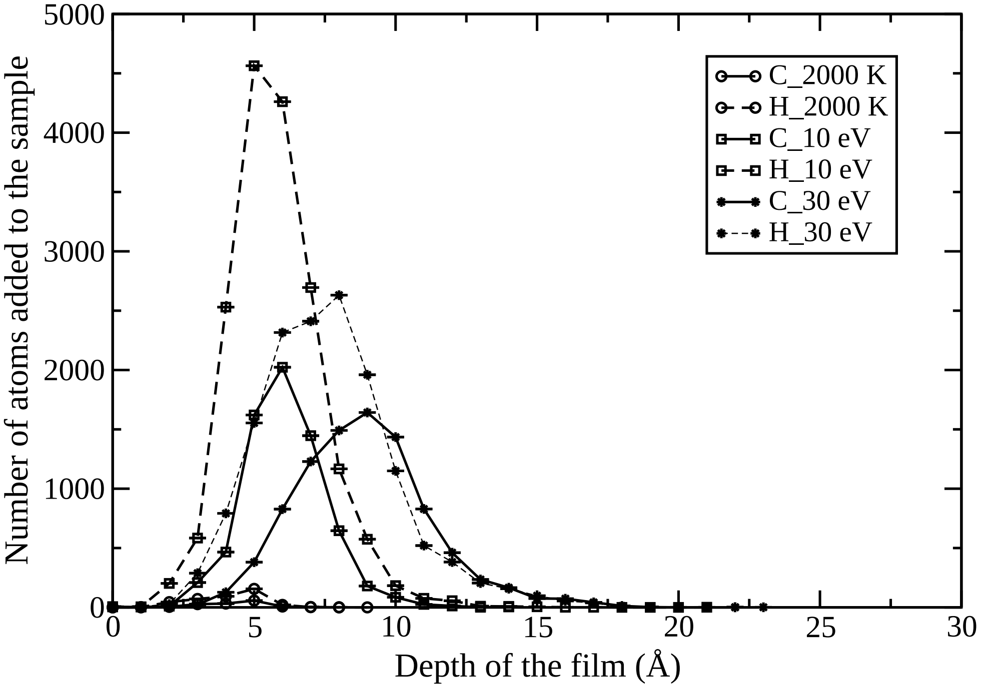

Figure 4.14: Depth profile of methyl radicals as a function of incident energy for 300 K sample temperature

It can be seen that the sticking coefficient increases with the incident energy and tending to saturate at higher energies. The radicals were found to break up on the surface and there is a reduction in the number of hydrogen atoms added per carbon atoms (H/C is 3 for 2000 K and 1.61 for 30 eV). The depth of incorporation was found to increase with the incident energy as shown in Fig. 4.14.

With the incident energy, the radicals are able to overcome the steric repulsion. This results in the increase in the sticking coefficient. However, in the case of energetic CH_3, the incorporation of C atoms into the sample is by various means (see Fig. 4.13). The incident methyl radical breaks up into different fragments on the surface, and the intake of C into the sample is in the form of various CH_y s where, $0 \leq y \leq 3$ (see Fig. 4.13). This resulted in the incorporation of hydrogenless radicals into the sample. This result is in agreement with the trends shown in the simulations of *Huang et. al.* [137].

The observed depth profile of the radicals with energy, (Fig. 4.14) can be understood by the stopping of carbon and hydrogen atoms by the surface atoms. As a consequence of the impact of radicals, the surface atoms are getting displaced and also creating knock-on atoms within the sample. This reduces the energy of the projectile and limits its range within the film.

4.5 Conclusions

Methyl radical chemisorption on a-C:H surface was studied using MD simulations for both thermal as well as energetic radicals at 300 K sample temperature. A new algorithm is developed for identifying the surface properties (such as roughness, number of dangling bonds *etc.*) of amorphous films and it is found to be capable of explaining the simulation data. The important conclusions from the study are as follows.

The major mechanism of sticking of thermal radicals is the direct, ballistic incorporation at the dangling bond locations. The sticking coefficient increases with the number of dangling bonds (between 1.3×10^{-3} to 5.86×10^{-2}). The energetic ion bombardment depletes the surface bound hydrogen and thereby creates more dangling bonds. This explains the enhanced sticking coefficient observed in the ion-beam experiments [74].

The sticking coefficient found to show a linear dependence with the number of dangling bonds which can be understood from the fact that, even if the total number of dangling bond increases, the ratio of occupied to unoccupied dangling bonds remain same. This can be explained from the interplay between steric effects and surface roughness. Surface area also found to show a linear relationship with the roughness of the film. The steric repulsion and surface roughness together cause a screening effect, which reduces the sticking cross-section. The contribution of screening effect is calculated using simple analytical method.

With the increase in the incident energy, the sticking cross-section increases, as the incident radical have energy to overcome the steric repulsion. The breaking of radicals on the surface increases and this resulted in the incorporation of hydrogen-less-radicals (CH_2,CH,C) into the sample.

As we have discussed in the previous chapter, the chemical erosion releases a variety of energetic hydrocarbons into the plasma. We have seen that the high energy species are capable of overcoming steric repulsion. They break on the surface and hydrogen-less radicals are incorporated to the growing film. This results in the formation of less-hydrogenated films, which is typically observed in the plasma-exposed regions of tokamaks.

We have also seen that the low energetic ones have less sticking coefficient. Therefore, they can undergo long range transport and reach the remote regions, where they form a-C:H films. The steric effects play a major role in the formation of such films and they also contribute to the structure of the film. This aspect is discussed in the next chapter with the help of Monte Carlo simulations.

Chapter 5

MC Modeling of Structure and Porosity

`In this chapter, the modeling of the growth of hydrocarbon films using Monte Carlo simulations is discussed.`

5.1 Introduction

In the previous chapter we have shown that the sticking of methyl radicals on hydrocarbon surfaces depends strongly on the hydrogen neighbourhood of the dangling bonds on the surface. We have also shown that the sticking of radicals occurs in such a way that the steric repulsion between H-atoms is minimized. Therefore, the molecules perform rotations on the surface to find a favorable energy configuration. However, MD study is limited to a few hundreds of atoms over a few tens of angstroms for about several nano-seconds. The actual film growth on the other hand consists of much larger dimensions of space and time (over several micro-meters for about several hours). The resulting structure of the film could be quite different due to the complex surface reactions during the growth and such processes are inaccessible using MD.

In extreme contrast to this atomistic picture, some of the existing models for co-deposited layer growth in fusion devices have studied the growth rate considering the interactions like hydrogen abstraction, surface coverage of radical sites and incoming fluxes of various species using a zero-dimensional particle balance [77, 136, 138]. Micro-structural information cannot be obtained from such models. The Monte Carlo (MC) techniques used in the past, in the context of diamond-like-carbon (DLC) formation, is most suited for our purpose [80, 81, 139–143], where, a probabilistic outcome of an atomic interaction is considered, rather than the detailed dynamics.

These studies, however, were for the cases where there was a continuous presence of plasma in contact with the film, with H atoms and energetic ions incident on the film actively taking part in its formation and stabilization. Since we are looking at the phenomenon of film formation in remote locations of the tokamak, the so-called 'stitching effect' of energetic ions [75, 76, 79, 133, 143] is absent in the amorphous hydrocarbon (a-C:H) network formation. In this effect, the actual network of bonds becomes final only below a certain depth from the surface, after the disturbance in surface atoms after the impact, has been stabilized. The stitching refers to the rejoining of initially broken bonds and an alteration in hybridization states. For the co-deposited films in the remote regions of fusion devices, one can expect only a vapor-phase mixture of neutrals (with some energy, accounting for the Frank-Condon dissociation reactions) and methyl radicals.

The principal mechanism of the growth under such conditions is the creation of dangling bonds by hydrogen abstraction and the attachment of CH_3 radicals at these dangling bond locations. One of the major ingredient which distinguishes it from the available growth models is the shape and structure of the molecule, from where the structure of the film can be derived directly. The steric effect arising out of the mutual repulsion between H-atoms is taken care by using the steric repulsion distance calculated from MD simulations. The details of the model are discussed in Section (5.2). The validation of the model is discussed in Section (5.3). The simulations are discussed in Section (5.4) and results are presented in Section (5.5). Discussion of the results is in Section (5.6). The conclusions from the study is presented in Section (5.7).

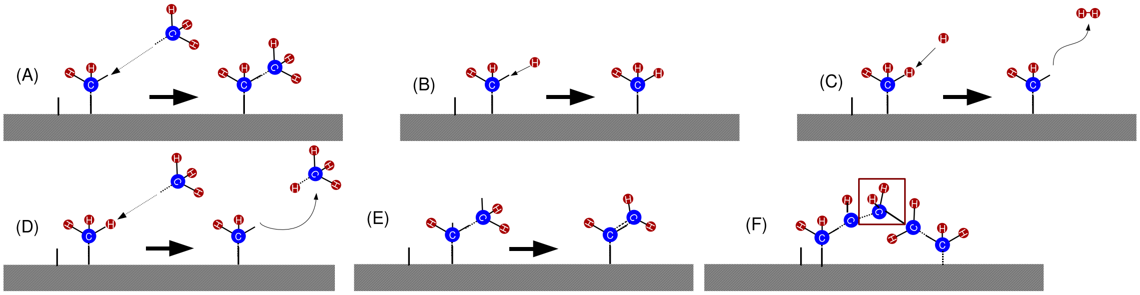

Figure 5.1: Schematic of various reactions implemented in the code: (A) sticking of CH_3 on a dangling bond location, (B) H addition to a dangling bond location (C) H abstraction by incident H atom, (D), H abstraction by CH_3 (E) sp^2 type cross-linking, (F) non-sp^2 type cross-linking

5.2 Model Description

To simulate the co-deposit formation at remote locations, a surface is imagined (having some initial population of dangling bonds) to be in contact with a vapour phase consisting of fuel-gas neutral atoms and molecules having a mixture of methyl (CH_3) radicals. The schematic of various reactions happening on the surface is shown in Fig. 5.1. Monte Carlo ansatz is followed as in a ballistic model for stacking methyl radicals. A more realistic scenario is considered, in which particles can arrive at any angle (not restricted to normal incidence only) and stick upon first contact with a dangling bond.

One of the natural effect that arises in the incorporation of thermal radicals into a growing film is the steric effect. This is arising out of the mutual repulsion between H atoms bonded to different carbon atoms in the matrix. The repulsion is parametrized using a distance criteria d_{crit} in such a way that the distance between any two H atoms in the sample must be higher than this cut-off. If the chosen location for the incorporation of the radical can not satisfy this criteria, the attempt of incorporation is rejected and the site is declared as blocked. The value of d_{crit} was chosen from MD simulations (as 1.6 Å) which is discussed in the previous chapter. The numerical details of implementation of the model is discussed in Chapter 2.

One of the key ingredients of the model is the shape and structure of the molecule, a fact which distinguishes it from the conventional models which considers only spherical particles. The a-C:H network we wish to model is more complex because of the presence of two type of hybridization states. The orientation of the molecules about the C–C bond axis is in such a way that the steric repulsion is minimized.

The incoming hydrogen atoms from the vapour phase perform (a) H-abstraction reactions, where the surface a bonded H atom is removed by leaving a dangling bond on the surface and (b) H addition to the available dangling bond locations. The flux of hydrogen atoms (Γ_H) is higher than CH_3 radicals (Γ_{CH_3}) (typical fluxes are: $\Gamma_H \sim 10^{15} cm^{-2}s$ and $\Gamma_{CH_3} \sim 10^{12} cm^{-2}s$). Thus, the time between two consecutive CH_3 bombardment events on the surface is much longer than that for the H atoms. Therefore, the surface is assumed to be in steady-state with respect to the H interactions between two CH_3 incorporation. The rate of change of dangling bonds on the surface between two CH_3 bombardment events can be written as,

$$\begin{aligned} \frac{dn_{db}}{dt} &= \Gamma_H \sigma^H_{abs} n_H - \Gamma_H \sigma^H_{add} n_{db} && (5.1) \\ n_{db} + n_H &= n_{tot} && (5.2) \end{aligned}$$

where n_{db} is the surface density (cm^{-2}) of dangling bonds, n_H is the surface density of H atoms, σ^H_{add} is the cross-section for addition of H atoms to dangling bond location and σ^H_{abs} is the cross-section for hydrogen abstraction from the surface. The values of σ^H_{abs} and σ^H_{add} are taken as $0.05 \times 10^{-16} cm^2$ and $1.3 \times 10^{-16} cm^2$ [19].

At the steady-state, from equations (5.1 and 5.2), the dangling bond population can be deduced as,

$$n_{db} = \frac{n_{tot}}{1+\mu}, \mu = \frac{\sigma^H_{add}}{\sigma^H_{abs}} \qquad (5.3)$$

The hydrogen interactions are not explicitly included in the model and the effects are included by assuming a steady-state dangling bond population on the surface. The probabilities of H abstraction and addition were obtained from the reported data base [19]. A random distribution of dangling bonds on the surface within the roughness scale is assumed. Methyl radical incorporation happens on these dangling bond locations.

Between two radical incorporation, the time elapsed is calculated by considering the flux ratio of hydrogen and CH_3. The number of H atoms incident on the surface of unit area between two CH_3 events are $\frac{\Gamma_H}{\Gamma_{CH_3}}\frac{1}{\pi\lambda_3^2}$, where $\pi\lambda_3^2$ is the area of an incoming radical. If t_{3f} is the time to fill a dangling bond out of n_d bonds, $t_{3f} = \frac{1}{\sigma'_d n_d \Gamma_{CH_3}}$, where σ'_d is the cross-section of a CH_3 radical, which is typically 12 Å^2 [91]. Since $\Gamma_H >> \Gamma_{CH_3}$, many H atoms could have hit within t_{3f} and therefore the dangling bond distribution on the surface could have been changed. The number of dangling bonds changed can be written as, $\Delta n_d = (\frac{\Gamma_H}{\Gamma_{CH_3}})(\frac{\sigma_d}{\sigma'_d})n_d$ where σ_d is the cross-section of H atoms to attach to a dangling bond. Therefore, between two CH_3 incorporation events, the above number of dangling bonds are shuffled randomly on the surface.

The CH_3 radical therefore, observe a steady-state dangling bond population on the surface and stick to the dangling bond locations by any of the following events. The events are (i) bonding of the radical with a dangling bond (sp^3 type), (ii) bonding along with H-abstraction (sp^2 type) and (iii) null event. The reason for incorporating sp^2 type bonding is as follows. In a film, there could be adjacent H abstraction events leading to the formation of double bonded structures (sp^2 type). This possibility has been included in the model by (ii). The events are chosen based on fixed probability.

The selection of target sites is done by calculating the exposed solid angle a given site has from the shadowing calculation. The numerical realization of the model is Film Growth Monte Carlo (FGMC) and the technical details of the implementation is discussed in detail in Chapter 2.

5.3 Validation and Testing of the Code

The results of the code is compared and validated against both MD simulations and continuum models such as ballistic deposition.

5.3.1 Tests using MD Simulations

The films grown in FGMC are tested in MD simulations using HCParCas code (see Chapter 2 for details). The samples formed in FGMC were tested in MD as it is, without any pressure and temperature control. For initial stages of the film there was relatively little ‘temperature’ rise. The temperature in MD is not in the thermodynamic sense, as the kinetic energy is interpreted in the form of temperature. This means, even a single molecule of 4 atoms can have a ‘temperature’ in MD. The rise in temperature can be considered as a measure of the strain in the sample, as the structure relaxes by releasing the excess potential energy which appears as the kinetic energy of the atoms (we will encounter these arguments in Chapter 7).

Thus, for the initial stages of the growth of FGMC film (upto 10-15 Å height) there was no change in the sample temperature and the potential energy of the system was at the minimum. However, with increase in the number of atoms in the film, the strain energy increases and this results in the expulsion of H atoms. This is because the steric configurational energy of the system increases with the number of H atoms and any perturbations are sufficient to expel the excess hydrogen atoms and go to a lower energy configuration.

5.3.2 Comparison with Continuum models

The FGMC samples are compared with non-linear continuum models for growth using ballistic deposition techniques. The details of the ballistic technique is discussed in Chapter 2. Since we have considered a ballistic-like (stick upon first contact) incorporation of the radicals, the evolution of the surface roughness of the film can be compared with the standard ballistic deposition as discussed in [60]. The evolution of the surface roughness (σ) with average height (H) for a sample size of 28×28 Å^2 for standard ballistic as well as FGMC is shown in Fig. 5.2. It can be seen from the figure that both FGMC and 3D ballistics yield similar curves and therefore, the ballistic nature of the code is being qualitatively verified.

The growth exponent on H is found qualitatively by a visual fit of a line ($ln\sigma =$

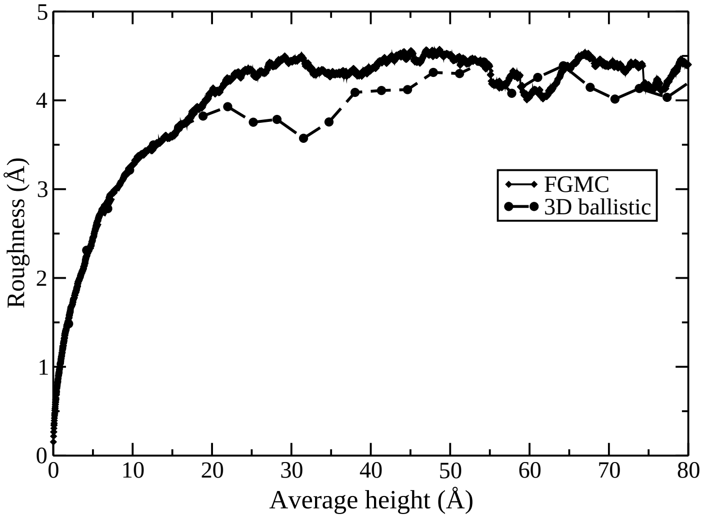

Figure 5.2: Variation of the roughness with mean height.

$C + \beta lnH$). There is an early increase in surface roughness and then a saturation, whose level increases with the sample size as shown in Fig. 5.3. The comparison of the model with Meakin's model is shown in 5.4. In the very early phase ($lnH \ll 1.5$), the growth exponent has the so-called 'trivial' value of 0.5. Later for saturated roughness, ($1.5 \leq lnH \leq 3$), the value is 0.25. From Fig. 5.3, it can be seen that the scaling shows consistency with 3D ballistics.

5.4 Simulations

We consider square sample sizes ($nx \times ny$) ranging from 7×7 to 100×100 Å^2. Periodic boundary conditions were implemented along X and Y directions, which form the plane of the surface on which the co-deposited film is grown. Dangling bonds are randomly associated with the bins on a smooth surface initially, in such a way that a certain surface density is effectively considered. Multiple showers of methyl radicals are then considered so that the film grows to a sufficient thickness. The simulations were performed by varying the parameters,

- d_{crit} (1.2 Å to 3 Å)
- P_{sp23} (0.0-0.9)

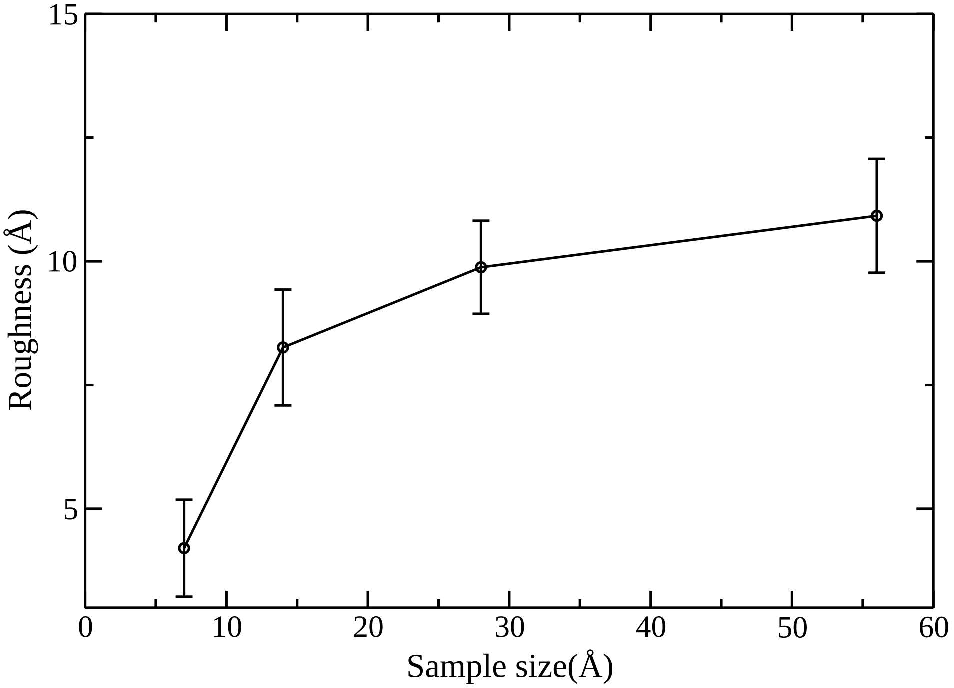

Figure 5.3: Variation of roughness with sample size

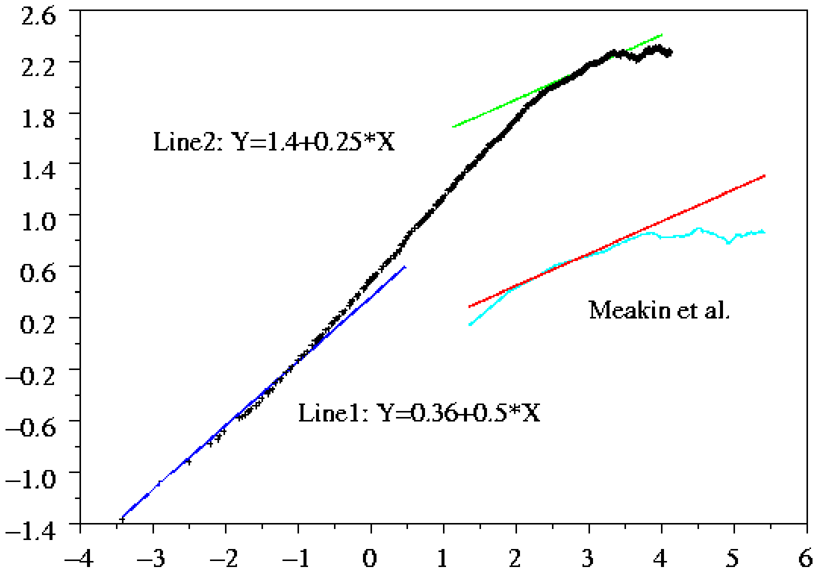

Figure 5.4: Comparison of scaling with ballistic model

- Sample size (7×7 Å^2 to 100 $\times$100 Å^2)
- initial surface density (*'rad'*) of radical sites (0.01-0.1)

The aim of the parametric variation was to obtain the general trend of the quantity with the parameter. Later on, simulations were done with fixed parameters for d_{crit}, P_{sp23}. The hydrogen abstraction probability was calculated from cross-section (0.05 Å^2).

The value of d_{crit} was actually varied from $0.4-3$ Å, but films with unrealistically large densities (greater than 3.2 gm/cc) were formed for values of $d_{crit} < 1.2$. We therefore present results only for $d_{crit} \geq 1.2$. Later on it was fixed at 1.65 Å by using the data from MD simulations. Porosity is defined as the ratio of total volume in voids to the total volume occupied by the film (with the height taken as a sum of mean height and twice the roughness, for 95% accuracy). A void volume is computed by counting the number of empty $1 \times 1 \times 1$ Å^3 bins for a connected region and subtracting out of it a volume numerically equivalent to its surface area in Å^2. We characterize the porosity of the grown films by finding out how much void-fraction can be attributed to different void-sizes, and parametrically study the variation of these quantities with hydrogen abstraction rates, sp^2/sp^3 ratios, radical site densities and the parameter d_{crit}. It is seen that d_{crit} is the most important parameter influencing the porosity and surface roughness at the micro-scales. Ten sets of simulations have been done for each parameter for obtaining the statistical error in the estimation.

Simulation with linear sample size 100 Å can takes about 2 days on a dedicated 3.1 Giga-flops machine with 8 Gb RAM. The main time consuming part in the simulation is the calculation of shadowing effects which goes at least as square of the sample size (since shadowing from far off growths are also considered). Note that the number of radical sites for which the shadowing probability must be calculated also rises as the height of the film grows. However, shadowing algorithm is less time consuming than actual ballistic, where lot of trials are wasted since the site selection is totally random among all species (C atoms, H atoms or dangling bonds) in the

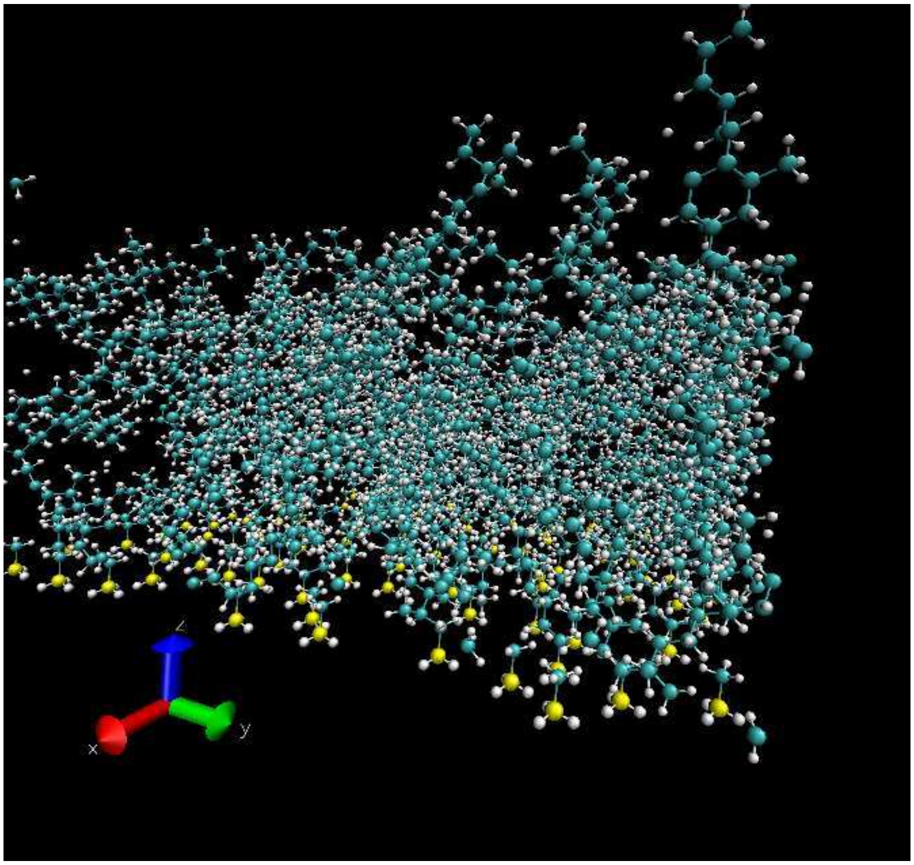

Figure 5.5: The film grown in FGMC for 56 × 56 Å^2 sample. The height of the structure is 20 Å. Blue: Carbon, White: Hydrogen, Yellow: Base C atoms.

system.

5.5 Results

The film grown in FGMC is shown in Fig. 5.5 with various atomic arrangements. The Radial Correlation Function (RDF) of the film was calculated as discussed in Section (2.3.1.2) of Chapter 2. The RDF was compared with the data from neutron scattering experiments and MD simulations are shown in Fig. 5.6. The additional peaks at 3 Å of FGMC film shows the presence of linear 3 carbon connections, which is an indication of polymeric chains.

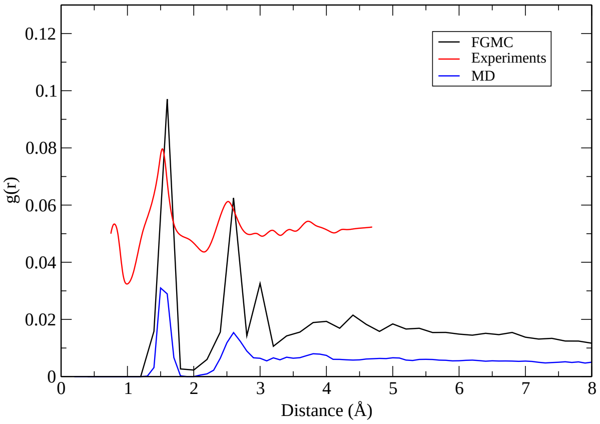

Figure 5.6: The radial correlation function of FGMC film compared with neutron scattering experiments and MD samples.

5.5.0.1 Variation of d_{crit}

The variation of density and porosity of the film with d_{crit} is shown in Fig. 5.7. It can be seen that the density of the film decreases with d_{crit} where as porosity increases. As d_{crit} increases, the distance between H atoms bonded to different C atoms increases and hence each radical occupies effectively more 'volume'. This results in the reduction of carbon density and consequently the porosity increases which also shows that the porosity and density have an inverse relationship with respect to each other.

The variation of roughness and H/C ratio of the film with d_{crit} is shown in Fig. 5.8. It is seen that the saturated roughness does not change significantly for values of $d_{crit} > 2$ (hitherto we mean saturated roughness wherever we state roughness). This is because, the role of d_{crit} is to enhance separation, which becomes less effective once it is of the order of the molecule itself. The H/C ratio of the film stays more or less constant for $d_{crit} < 2$. In all other simulations the value of d_{crit} has been set at 1.65 Å.

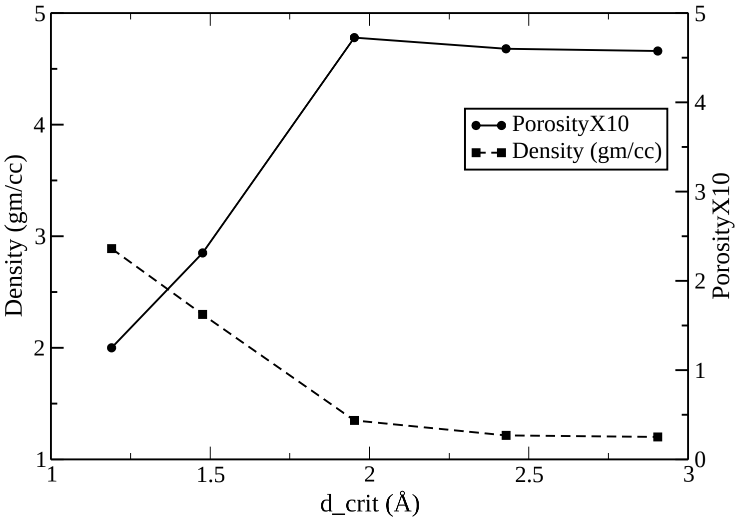

Figure 5.7: Trend of density and porosity of the film with d_{crit}. Sample size 14×14 Å^2, $P_{sp23} = 0.5$

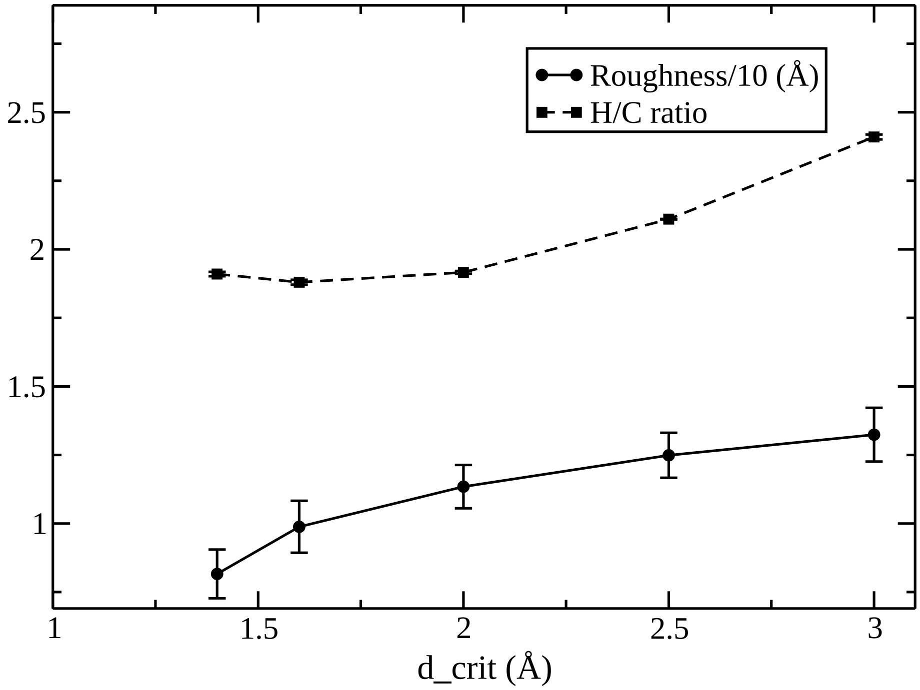

Figure 5.8: Variation of roughness and H/C ratio with d_{crit}.

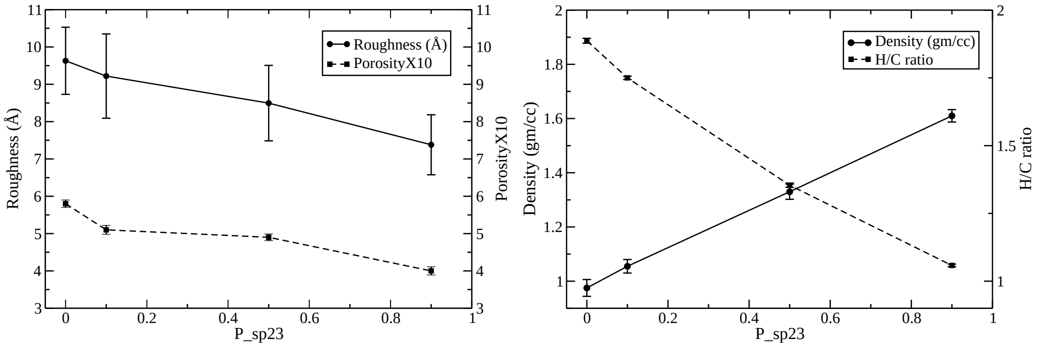

Figure 5.9: Variation quantities with P_{sp23}: (left) roughness and porosity, (right) density and H/C ratio. Sample size 28 × 28 Å^2, d_{crit} = 1.65 Å

5.5.0.2 Variation of P_{sp23}

The variation of roughness and porosity with P_{sp23}, for a fixed d_{crit} is shown in Fig. 5.9. It can be seen that both roughness and porosity reduces with increase in P_{sp23}. This is because, as P_{sp23} increases, the fraction of sp^2 incorporation to the film increases which needs effectively less 'steric-volume' compared to sp^3 due to the less number of H atoms. Consequently as porosity reduces the density increases (right hand side of 5.9). The surface roughness also reduces because the size of the molecule reduces (total size of the molecule) with sp^2 fraction and as a consequence of that, the molecules can be more closely packed. This reduces the fluctuations in height, which is related as the roughness.

5.5.0.3 Variation of Sample Size

The quantities also shows variation with sample sizes and the variation of roughness has used as the validation of the code with continuum models, which has been shown in Fig. 5.10. The density (∼ 1 gm/cc)and H/C ratio (∼ 1.85) of the film did not show any significant variation. However, the porosity of the film is varied between and is shown in Fig. 5.3. The variation of void size distribution with the sample size is shown in Fig. 5.11. As the sample size increases, the contribution of bigger voids increases and therefore, the total porosity increases.

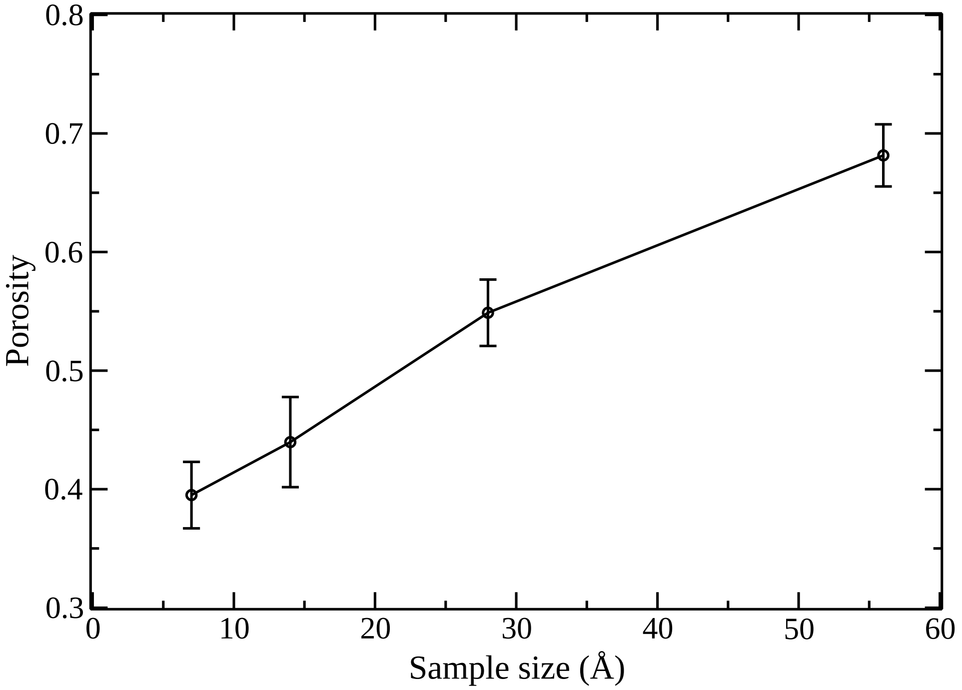

Figure 5.10: Variation of porosity with *Sample size* for $P_{sp23} = 0$ and $d_{crit} = 1.65$ Å

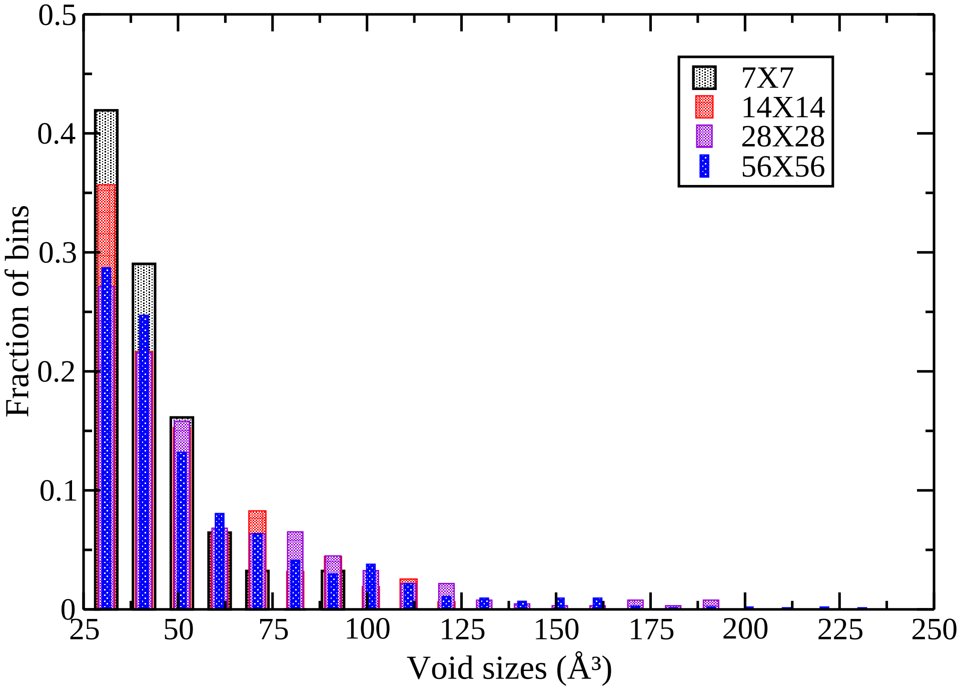

Figure 5.11: Fractional contribution of different void sizes to the total void-volume, variation with *Sample size* for $P_{sp23} = 0$ and $d_{crit} = 1.65$ Å

5.5.0.4 Variation of Initial Radical Density *rad*

The bulk and saturated properties of the film (density, H/C ratio and surface roughness) found to have little dependence on the initial radical density. However, the distance at which the surface roughness saturates is found to have dependence on the initial radical density. The correlation properties of the surface becomes important only after this 'cross-over height', which is a function of the initial available locations for the growth. The further significance of this result is discussed in Section 5.6.

5.6 Discussion

The film properties show significant variation with d_{crit}. It can be seen from Fig. 5.7, that the d_{crit} values from 1.5 to 2 Å shows a sharp change in the density and porosity values of the films. The density values of interest for soft polymer like films lies in this range. This is in agreement with the calculated value of d_{crit} from MD simulations discussed in the previous chapter, where d_{crit} value lies between 1.6 Å to 1.7 Å. The steric repulsion factor along with the rotational freedom about C–C bond axis, gives the amorphous nature of the film. The steric repulsion factor leads to the microporosity of the film.

Another important factor which contributes significantly to the total porosity of the film is the shadowing effects. Shadowing affects both the void size distribution and the total porosity of the film. It can be seen from Fig 5.12 that with shadowing the fraction of voids increases. Without shadowing the total porosity of the film was 0.29 ± 0.14 and with shadowing this became 0.36 ± 0.12. This is because many of the sites are not selected due to their relatively less probability of being accessible as a consequence of shadowing from the structures which are taller than the given site. This results certain dangling bonds get unoccupied within the film and consequently the void fraction of the film increases.

The surface roughness of the film however, found to have rather strong dependence on the steric effects than shadowing. This can be seen from Fig. 5.8 and Fig.

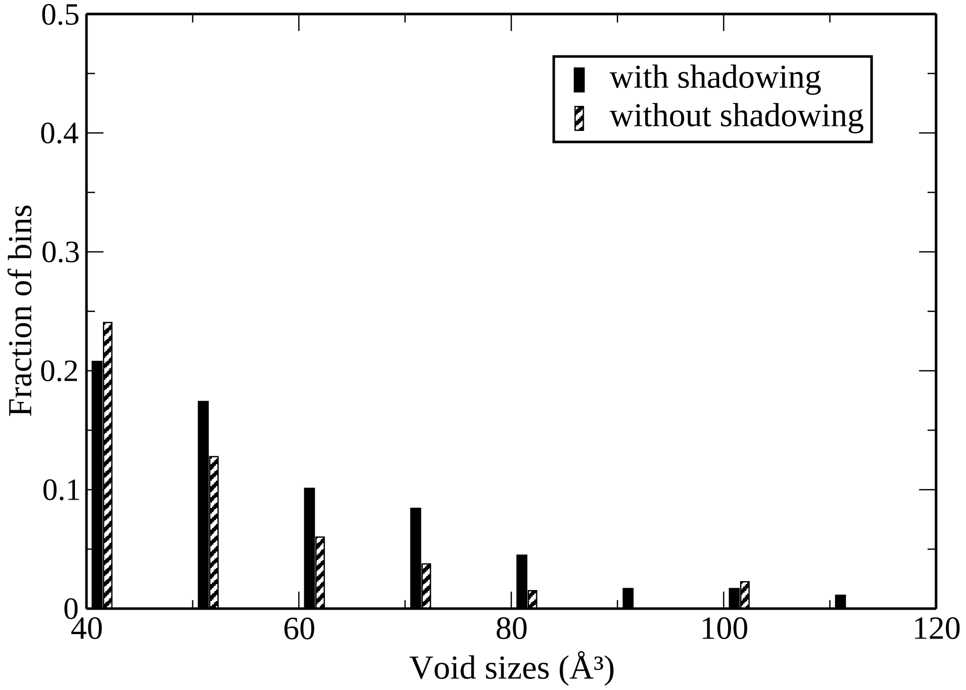

Figure 5.12: Fractional contribution of different void sizes to the total void-volume with and without shadowing effects. Sample size 14 × 14 Å^2, $P_{sp23} = 0.0$ and $d_{crit} = 1.65$ Å .

5.13. Though the fluctuations in the roughness is higher in the shadowing case, the mean value of the saturated roughness did not show much significant variation. The saturation occurs as a consequence of the correlations developing in the system.

The cross-over time (height) at which these correlations exist in the system is a function of the initial dangling bond distribution of the system. The saturation occurs due to the finite system dimensions and therefore, the cross-over height also depends on the sample size. For a finite system, when the correlation length equals the system size, the entire interface becomes correlated and this results in the saturation of the width of the interface (roughness). In Fig. 5.14 the dependence of this height on the sample size is shown. However, the dependence of cross-over height on the initial dangling bonds is more complicated due to the combined effect of steric effects and shadowing. With the increase in the number of dangling bonds, the cross-over height reduces and the details can be seen in Table. 5.1. Most of the initial sites were not used for further growth due to the steric effects or shadowing. Thus, the actual number of sites on which incorporation happened will be less than

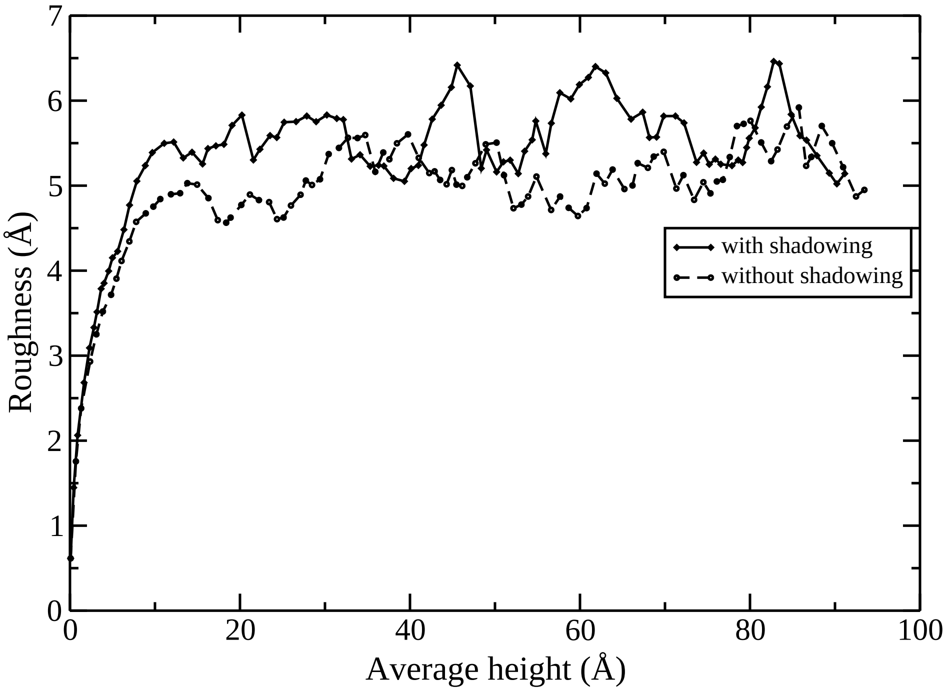

Figure 5.13: The roughness evolution of the film with and without shadowing. Sample size 28 × 28 $Å^2$, $P_{sp23} = 0.0$ and $d_{crit} = 1.65$ Å

.

the initial sites. This is what column 3 of the Table. 5.1. From the table it can be seen that, the distribution of sites rather than the number of sites, which signifies the further growth. Though the number of sites are less, if they are sufficiently sparse (at least equal to 4 Å), then those sites can contribute to further growth and quick saturation of the roughness.

Table 5.1: The table of the dependence of cross-over height on the initial dangling bond population

.

No. of initial radical sites	Radical density ($Å^{-2}$)	No. of actual initial sites	Cross over height (Å)
1	0.005	1	10
2	0.010	2	9
9	0.0459	8	6.5
25	0.128	5	10
34	0.178	6	6

Though the sites are getting selected by shadowing, the steric effects at the

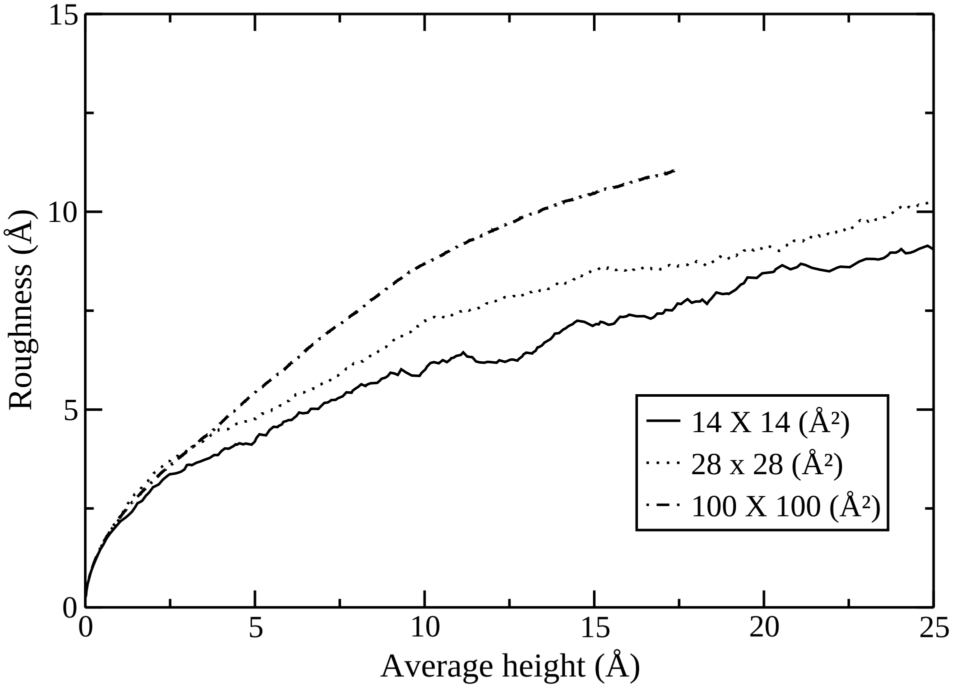

Figure 5.14: The roughness evolution of the film with and without shadowing. Sample size 28 × 28 Å^2, $P_{sp23} = 0.0$ and $d_{crit} = 1.65$ Å
.

microscopic level reject a fraction of them due to the proximity of other atoms less than d_{crit}. Hence the combined effect of both the shadowing and the steric repulsion results in the total porosity of the film. Though the hydrogen abstraction reactions create uniform number of dangling bonds on the surface, a small of fraction of which is only being selected for incorporation due to these effects. As a consequence, a fraction of dangling bonds remain within the film. This can be seen from Fig. 5.15. It was calculated by normalizing the number of dangling bonds to the surface area at 3 Å height intervals of the sample (in the Z direction) at the end of the simulation. Thus, it shows that at each height a fixed number of dangling bonds remain unfilled. These dangling bonds can recombine later to form more cross-linked structures.

The density of the films was found to vary with the sp^2 content. The density of the film when all C atoms are in sp^3 configuration was found to be $\sim$ 1 gm/cc (Fig. 5.9). This is in agreement with the reported values of density of hydrocarbon films grown under floating potential conditions from methane plasma discharges [122]. The films formed under such conditions are expected to be free of sp^2 type bonding

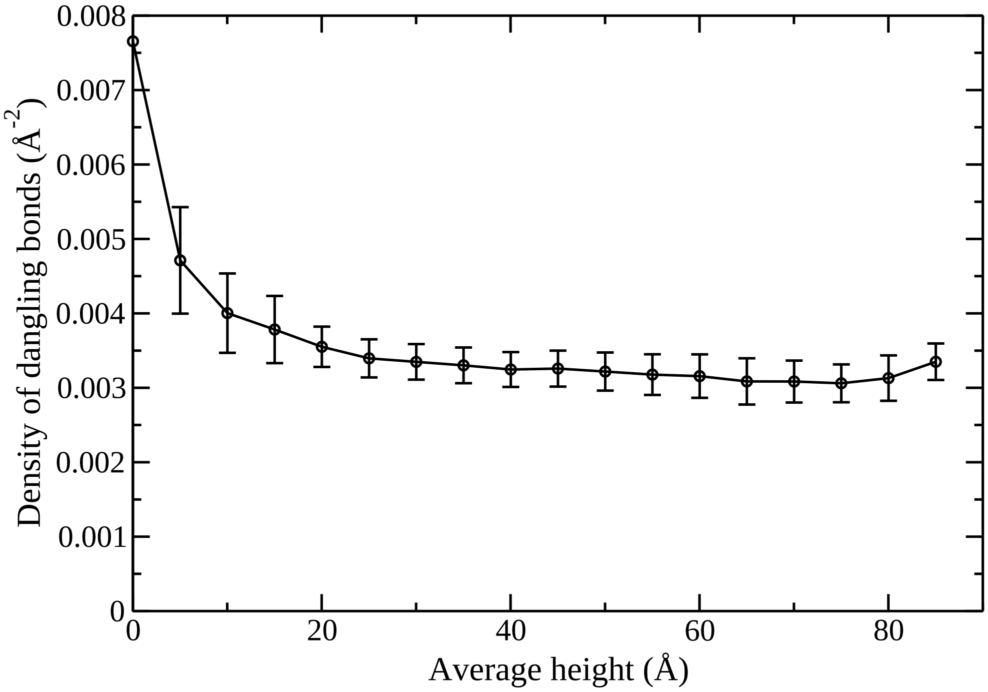

Figure 5.15: The distribution of dangling bonds within the film. Sample size 28 × 28 Å^2, $P_{sp23} = 0.0$ and $d_{crit} = 1.65$ Å
.

[69]. As the sp^2 fraction increases density also increases since more atoms can be arranged in a given volume due to the small volume of sp^2 bonded carbon atoms. This is consistent with the reported values [122] where the density increases with the reduction in hydrogen atoms of the radical in the gas phase (for pure ethene discharges, the reported density values are 1.1 gm/cc and for ethyne it is 1.4 gm/cc).

The H/C ratio of such films are in the range of ≤ 1 and the hydrogen content is < 0.5 [69,72,77,122]. However, the films obtained from FGMC shows high hydrogen content and H/C ratio (≤ 2) for zero sp^2 fraction. This indicates that there exist additional H elimination mechanisms which leads to the cross-linking of hydrocarbon chains.

5.7 Conclusions

The Film Growth Monte Carlo (FGMC) code is found to be capable of growing hydrocarbon films from thermal methyl radicals and hydrogen atoms. The surface roughness of these films shows consistent scaling with standard ballistic models. The initial stages of these films are extremely stable in MD simulations. The typical film density is in the range of 1 gm/cc to 1.6 gm/cc.

The steric repulsion is found to be one of the important parameter in deciding the structure (atomic arrangement) and the microporosity of the films. The steric repulsion and shadowing effects together decide the structure and porosity of the films. They also cause the deep burial of dangling bonds within the film. This can be understood as follows:

- Atomic hydrogen creates open bonds on the surface within its penetration range (twice the roughness)
- Shadowing prevents certain sites being selected for CH_3 incorporation
- Steric repulsion forbids the incorporation on these sites unless steric-clearance is achieved

Hence the combination of both these effects create unfilled dangling bonds in the bulk of the films. These dangling bonds can be further recombined or hydrogenated.

The hydrogenation of the dangling bonds is studied by studying the dynamics of hydrogen within the films. This is done by a time dependent Monte Carlo model, details of which is discussed in the next chapter.

Chapter 6

KMC Simulations for H Dynamics

`In this chapter we discuss the reaction-diffusion model for H dynamics within the co-deposited layers using Kinetic Monte Carlo simulations.`

6.1 Introduction

In the previous chapter, we have seen that, though the dangling bonds are created uniformly on the surface, steric effects prevent CH_3 incorporation at certain bonds. The co-deposits continue to grow and the diffusion of the background hydrogen can contribute to the filling of these 'buried' dangling bonds. Hence, the dynamics of hydrogen within the co-deposits is important for estimating the total hydrogen content. The reactivity of molecular hydrogen with the a-C:H films is very negligible and hence does not contribute to the retention. However, atomic hydrogen reacts with the film and can get trapped at the dangling bond locations.

The H-dynamics within graphite and other graphite-like co-deposits was studied in the past [5, 22, 23, 144, 145] using an adsorption-desorption model for particle transport. The atoms were assumed to be trapped within the potential energy wells on the surface. Due to the surface temperature (T) the atoms get out of the wells (de-trapping) at a rate $\omega = \omega_0 e^{(-\frac{E_m}{kT})}$, where ω_0 is the attempt frequency for transition and E_m is the depth of the potential well. It is known as Migration Energy (ME). The inherent assumption which goes into the model is that the events follow a Poisson distribution (see Section 2.5 for details).

The atoms move along the internal porosities of the deposits due to adsorption-desorption processes. During the transport they can recombine with either other H atoms or dangling bonds [5, 22]. The recombination is based on Smoluchowski boundary condition, where the atoms recombine if the distance between two atoms is less than a critical distance r_0 [146]. Such a boundary condition is valid for when reflection becomes a rare event once the atom are closer than the cut-off distance. The hydrogen atoms are considered as desorbed out permanently once they are above the top surface of the sample.

The above scheme is extended for the study of hydrogen dynamics within co-deposits created from FGMC simulations. The key factor which decides the H-dynamics is the migration energy, E_m. It depends on the local neighbourhood of the H atom. In the case of crystalline graphite this was estimated as 0.5 eV [144]. In amorphous materials there can be a variety of atomic arrangements and therefore, ME will be a distribution depending on the neighbourhood. Ideally this will have to calculate from the trajectories of hydrogen atoms within the co-deposits using MD simulations. But, this is nearly impossible due to the limitation of total simulation time (upto several nano seconds), within which the hydrogen will not be able to access most of the possible paths.

Therefore, we propose an alternate scheme based on the Potential Energy Surface (PES) analysis of the sample to derive the ME distribution. Here, instead of tracking the trajectories of H atoms, we use an ensemble of identical neighbourhoods at a given instant of time. Thus, the model overcomes the inherent time limitation of MD simulations. In the first part of this chapter, Section (6.2), we discuss this scheme. In Section (6.3), the simulations are discussed for constant migration energy (of graphite) and the distribution. The results are presented in Section (6.4) and the discussion is given in Section (6.5).

6.2 Migration Energy of H Atoms

To calculate the energy barriers in the co-deposits for hydrogen transport, a method is developed based on the Potential Energy Surface (PES) analysis. The potential energy surface of the hydrogen atoms within the film was calculated using Brenner potential [100]. To calculate the PES a method similar to what is discussed in Chapter 4 is adopted. The hydrogen atom is placed at the corners of the bin and the potential energy is calculated at each grid point.

The samples used for calculating ME were of two types: one from MD simulations as discussed in Chapter 3 (Section 3.2.1), with a density of 1.8 gm/cc. It consisted of 572 carbon atoms and 344 hydrogen atoms in $14 \times 14 \times 32$ Å^3 volume. The properties are close to intermediate type hydrocarbon layers [122]. The second one was developed from FGMC code as discussed in the previous chapter, with a density of 1.2 gm/cc (corresponds to soft films [122]) . The sample had the same dimension consisted of 620 atoms (211 C atoms and 409 H atoms). The dimensions are so chosen in both the cases such that they can be a representative case of real situation, as there exists enough number of local neighbourhoods.

The samples were binned in X, Y and Z directions with 0.2 Å bin size and each location is defined by a unique bin index. The atoms in the samples were considered to be in fixed locations (‘frozen’), while taking the measurements. A test H atom was kept at each bin locations (corners of the bin) and the potential energy of that location due to the neighbouring atoms (many body interaction) was calculated. Thus, a 3D matrix of potential energy values were obtained.

The local minima locations within the film were identified by calculating the potential difference at each grid point. In 3D, a given bin has 26 neighbours and if the potential energy of all these locations are higher than the grid point, then that location is considered as a minimum. In such a way, 1826 minima were found for the first sample and 1513 for the second one. The H atoms are residing at local minima and therefore, they have to overcome the energy barriers during their transport.

In order to calculate the barriers, 1000 particles were initialized at each minima.

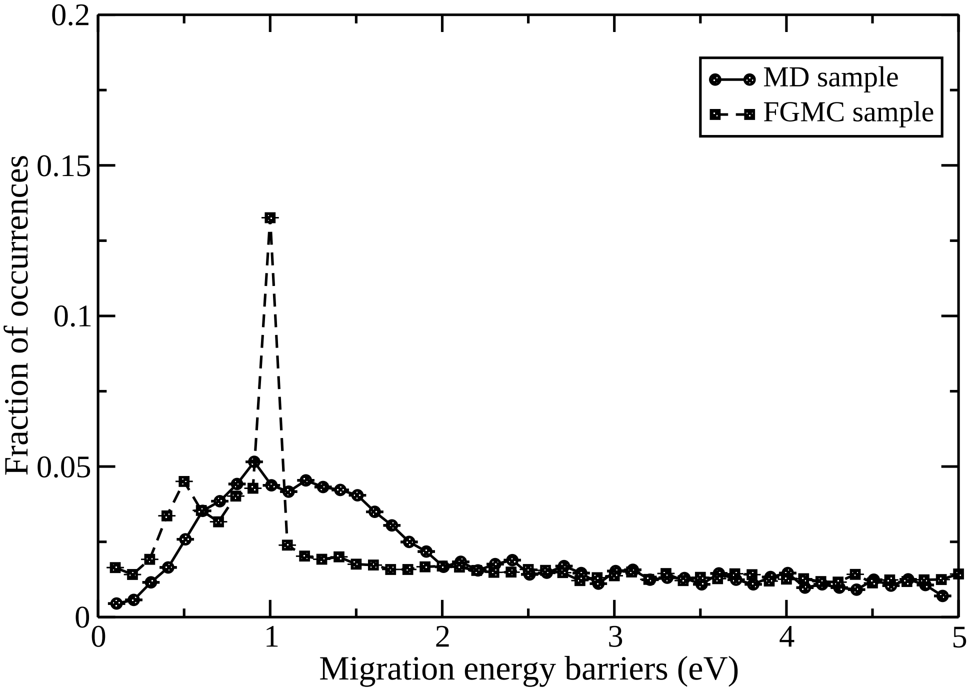

Figure 6.1: Distribution of migration energy of MD generated sample and FGMC sample.

They were moved from their locations in random directions with uniform probability. Thus the particles performed 3D random walk and their paths were tracked until they reached the next minima. The same procedure was repeated for all the particles initialized at all the minima. The migration energy is difference in between the initial energy of the minimum location and the maximum energy the particle encountered while its transport to another minimum. This was calculated for each trajectory and its distribution gives the migration energy for the a-C:H film. The ME distribution for MD generated sample and FGMC sample is shown in Fig. 6.1. The distribution is broader in the case of MD sample, where as the mean energy remains more or less same for both the case (close to 1 eV) (for explanation see the Section (6.5)).

The above scheme used a frozen sample while calculating the potential energy. In reality, when the hydrogen atom moves in space, the local neighbourhood would slightly re-adjusts slightly. Such an analysis requires a time dependent study and this is not expected to change the energy distribution drastically. However, such a study is not the scope of the present thesis.

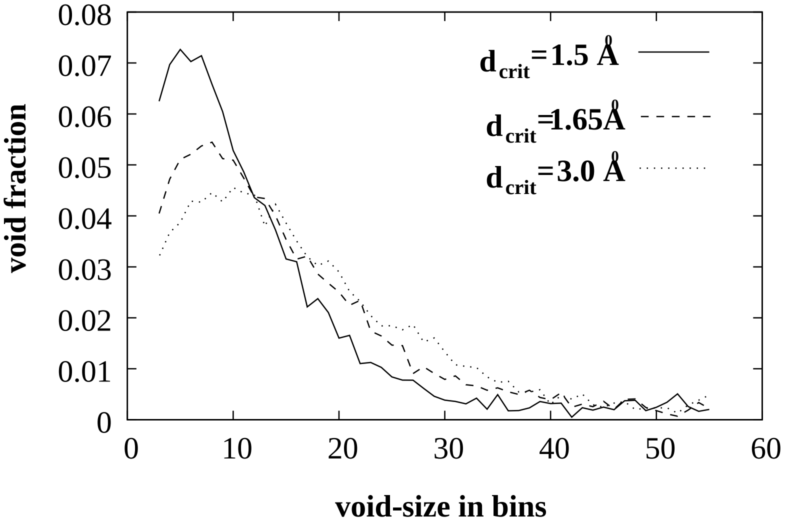

Figure 6.2: Voidsize distribution of samples

6.3 Setting Up Simulations

6.3.1 Creation of the FGMC Sample

The hydrogen dynamics is studied on samples generated from FGMC code, which is discussed in Chapter 5. We consider 3 types of samples with different density, H/C ratio, trap content and void size distribution. The sample properties are given in Table. 5.1. These samples are generated for steric repulsion parameter d_{crit} values at 1.65 Å (set1) 1.5 Å (set2) and 3.0 Å (set3) with different sp^3 to sp^2 ratio (P_{sp23}). The sample size in all the cases were 56 × 56 × 70 Å^3. The void size distribution of the sample was calculated and is shown in the Fig. 6.2.

Table 6.1: Properties of different co-deposited layers used in the simulation. The sample size was 56 × 56 × 70 Å^3 for all the cases.

Data sets	d_{crit} Å	P_{sp23}	Density (gm/cc)	Porosity	H/C	n_{db}/C
set1	1.65	0.0	0.960	0.480	0.119	0.903
set2	1.5	0.5	1.681	0.331	0.187	0.546
set3	3.0	0.0	0.856	0.501	1.957	0.065

6.3.2 KMC Simulations of Hydrogen Dynamics

The KMC algorithm needs the locations of atoms, the dangling bonds (db) and the void-size distribution present in the sample. The surface is defined as the interface between the voids and the bulk of the material which is the atom locations. The surface is considered to possess traps of different energies. The trap sites can be dangling bond locations as well. The hydrogen atoms jump between the trap sites in random directions. The maximum jump length in any direction was taken to be 30 Å which is greater than the size of any void in the sample. The simulations were performed for 10,000 time steps within which the system has reached steady-state in all the cases. The steady-state is defined as a particle balance condition, where the fraction of surface recombination processes did not change with time. The chance of breaking a C–H bond by thermal excitations is negligibly less at 300 K (since the bond energy is $\sim$ 2 eV). Hence, once the hydrogen is bonded its dynamics is not tracked further. The simulations in all the cases were repeated for ten sets with different random seeds. The simulations are:

- <u>Constant ME</u>

  <u>`case 1`</u>: Four hundred H atoms were initialized on the sample surface.

  <u>`case 2`</u>: Four hundred H atoms were initialized through out the internal surface of the sample.

- <u>ME distribution</u>

  <u>`case 1`</u>: Variation of ME distributions with different peak and width of the distribution.

  (a) Peak: 0.5 eV; Width = 0.45 eV (peak corresponds to graphite)

  (b) Peak: 1.0 eV; Width = 0.01 eV (corresponds to FGMC sample)

  (c) Peak: 1.15 eV; Width = 0.45 eV (corresponds to MD generated sample)

  For all the simulations of `case 1`, four hundred H atoms were initialized on the top surface of the sample.

  <u>`case 2`</u>: Variation of incident flux between $\times 10^{14} m^{-2} s^{-1}$ to 1 $\times 10^{30} m^{-2} s^{-1}$. These simulations were performed with ME distribution corresponds to (c).

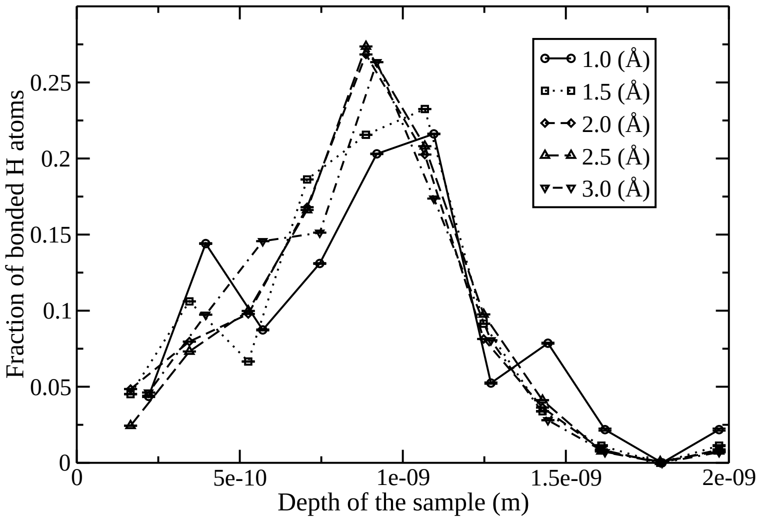

Figure 6.3: Depth profile of bonded H atoms as a function of the recombination distance. Both H–H and H–db distance were the same.

- Estimation of Diffusion Coefficient

  The simulations were performed for both constant ME and distribution cases. Five thousand hydrogen atoms were initialized on the sample surface for three different constant ME values (0.5 eV, 1.0 eV and 1.5 eV) and three different distributions (0.5 ± 0.45 eV, 1.0 ± 0.01 eV and 1.15 ± 0.45 eV)

Apart from that, a parametric scan on H–H and H–db recombination cut-off (r_0) distances were performed between 0.5 Å to 3.0 Å for 0.5 eV constant ME value for 400 particles initialized within the samples. The simulations were performed for a fixed number of particles initialized on the top surface of the sample. The depth profile of the bonded hydrogen within the sample remained similar for the all the distances above 1 Å and is shown in Fig. 6.3. Hence for all other simulations described in this chapter, we used 2.0 Å cut-off.

6.4 Results

The variation of the trapped and desorbed fraction of H atoms as a function of H/C ratio and n_{db}/C ratio at the steady-state is shown in Table. 6.2. It can be seen that, the trapped fraction increases with the number of dangling bonds and decreases

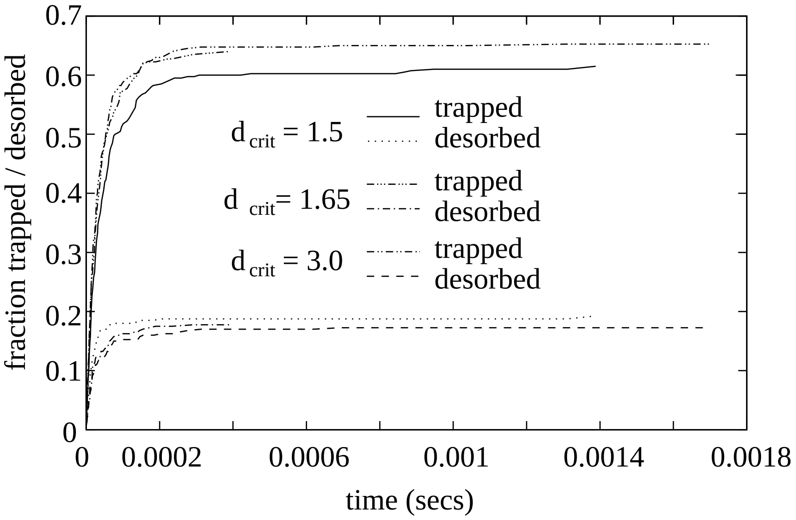

Figure 6.4: Fraction of hydrogen trapped as a function of time at 300 K for different values of d_{crit} (in Å) for 0.5 eV migration energy. The particles were initialized throughout the sample volume.

with H/C ratio. The results are for the particles initialized on the top layer of the film. In comparison with the initialization throughout the sample, the fraction of H desorption was nearly zero and the bonded fraction was upto 0.65 with a reduced H_2 molecule fraction close to 0.3. The fraction of various species as a function of time for the latter case is shown in Fig. 6.4.

Table 6.2: The fraction of bonded and desorbed atoms at the steady-state as a function of the $\frac{n_{db}}{C}$ for 0.5 eV migration energy.

Data sets	n_{db}/C	H bonded	H desorbed	H_2 formed
set1	0.903	0.22 ± 0.007	0.215 ± 0.05	0.565 ± 0.05
set2	0.546	0.1525 ± 0.014	0.75 ± 0.025	0.2675 ± 0.018
set3	0.065	0	0.3 ± 0.014	0.7 ± 0.014

The difference in the quantities in both the cases is because of the availability of more dangling bond sites in the internal surfaces of the sample than on the top surface. Also due to the large internal surface area, the distance between H atoms were less, which reduces the H–H recombination. The fraction of atoms which are initialized on the top surface were less (< 0.1%) and this resulted in a very low fraction of desorbed atoms. In the case of sample 3, which corresponds to the n_{db}/C ratio of 0.065, the bonded H fraction was negligible.

In the case of ME distribution, the fraction of bonded and desorbed H atoms is given in Table. 6.3. It can be seen that, the steady-state fractions depend on the width of the distribution rather than the peak. Comparing with the constant ME distribution given in Table. 6.2, the bonded H fraction increases with the decrease in the width of the distribution. The H_2 molecule formation reduces with the increase in the width of the distribution. This is because a notable fraction of the traps are having ME values greater than the mean. Hence, the H atoms trapped at those locations will take more time to adsorb, whereas the ones which are in the lower wells will easily come out. Hence, the chance of meeting another H atom is reduced. Also, the traps are having lower ME are not close to each other therefore, during its transport there is a high chance that they either get desorbed or get attached to a dangling bond location. This becomes more clear from data set 3 (for both 0.5 eV and 1.15 eV peak), where the number of dangling bonds were negligibly less and a significant fraction was desorbed as H atoms from the surface. If we compare with this with the case of 1.0 eV peak, H_2 molecule formation was high.

However, the time to reach the steady-state ('cross-over time') depends on the peak and width of ME. For data set1, in the case of constant ME (see Fig. 6.4) this time was fraction of milli-seconds, where as for 0.5 eV distribution, it took $\sim 10^{13}$ seconds to reach the steady-state. This is because of the higher ME values of the distribution. However, for 1.0 eV case with a narrow width (0.01 eV), the crossing-over time was $\sim 10^4$ seconds. Similar results were obtained for other data sets as well.

The steady-state fraction of bonded hydrogen with the incident flux for data set2 corresponds to the ME distribution of 1.15 eV with 0.45 eV width is shown in Fig. 6.5. It can be seen that the number of bonded H atoms increases with the flux upto $10^{20} m^{-2} s^{-1}$ and then reduces afterwards. This is because, at very low fluxes, the chance of both H–H and H–db re-combinations are less as the total number of H atoms incident within the given time was less. As the flux increases, initially the chance of H–db recombination is higher than H–H recombination. At higher fluxes H–H recombination overtakes the H–db recombination. Thus, the total number of

Table 6.3: The fraction of bonded and desorbed atoms at the steady-state as a function of $\frac{n_{db}}{C}$ for different ME distributions.

Data sets	n_{db}/C	ME values (eV)	H bonded	H desorbed	H_2 formed
set1	0.903	0.5 ± 0.45	0.4025	0.485	0.1125
		1.0 ± 0.01	0.55	0.32	0.125
		1.15 ± 0.45	0.4025	0.485	0.1125
set2	0.546	0.5 ± 0.45	0.2175	0.58	0.205
		1.0 ± 0.01	0.2275	0.575	0.195
		1.15 ± 0.45	0.2175	0.58	0.205
set3	0.065	0.5 ± 0.45	0	0.71	0.2875
		1.0 ± 0.01	0	0.665	0.335
		1.15 ± 0.45	0	0.71	0.2875

hydrogen atoms added to the sample shows a peaked profile.

The fraction of bonded (normalized to the total number of incident particles) reduces monotonically with the flux. This is because, after reaching the steady state, the incident H atoms either desorbed as H itself or H_2. At lower fluxes, the number of H atoms incident over the simulation time was less and therefore, though the actual H bonding was less, the fraction remained high. With flux, the number of incident H-atoms in the time of simulation increases and hence the fraction reduces.

The depth profile of the bonded H atoms within the sample is shown in Fig. 6.6. It can be seen that, the depth profile is limited upto 20 Å and remains the same for all the incident fluxes.

The diffusion co-efficient of hydrogen atoms within the films were calculated for both constant ME and distribution. Diffusion coefficient is defined as the mean square displacement of the atoms per unit time. The values of the mean diffusion coefficient as a function of migration energy is given in Table. 6.4. It can be seen that the diffusion coefficient reduces with the increase in migration energy as well as the increase in the width of the distribution.

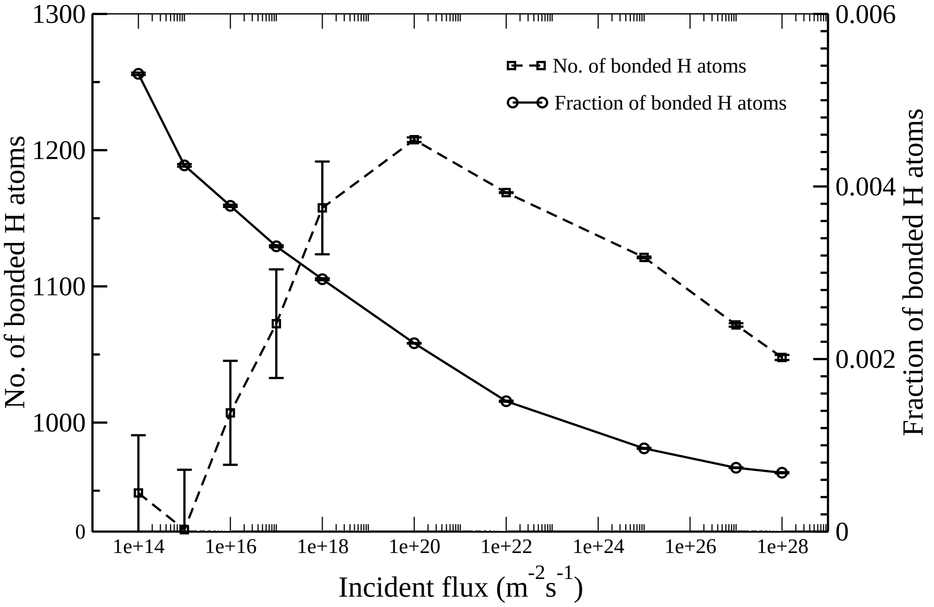

Figure 6.5: The number and fraction of bonded H atoms as a function of the incident flux

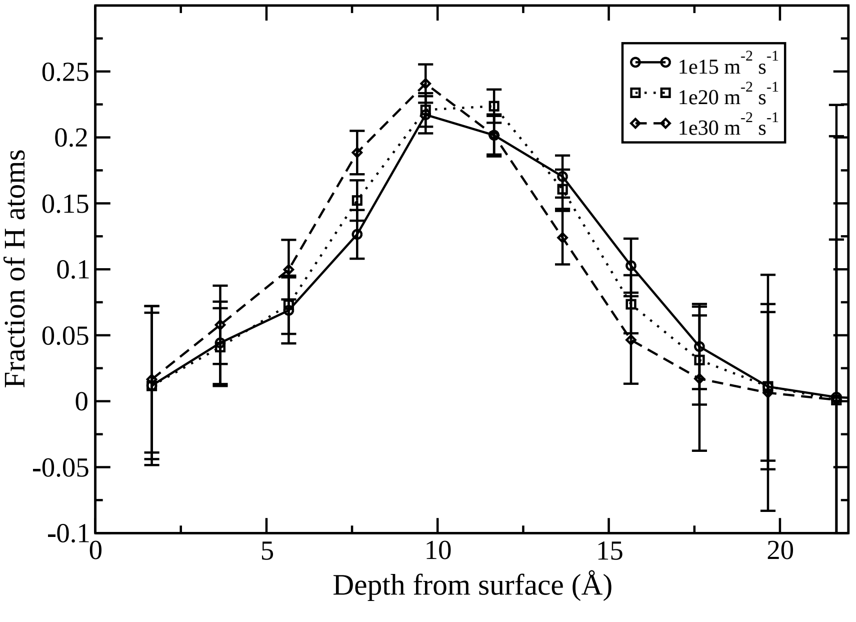

Figure 6.6: Depth profile of trapped H atoms for different incident flux.

Table 6.4: The diffusion co-efficient of H atoms as a function of ME.

Energy (eV)	Diffusion coefficient (m^2s^{-1})
0.5	$5.87\times10^{-14} \pm 1.108 \times 10^{-15}$
1.0	$2.34\times10^{-22} \pm 4.42\times10^{-24}$
1.5	$9.33\times10^{-31} \pm 1.76\times10^{-32}$
0.5 ± 0.45	$1.08\times10^{-16} \pm 6.72\times10^{-18}$
1.0 ± 0.01	$2.26 \times10^{-22} \pm 3.82\times10^{-24}$
1.15 ± 0.45	$1.31 \times10^{-27} \pm 8.09 \times10^{-29}$

6.5 Discussion

The ME distribution of the sample showed that there exists a peak around 1 eV for both the types of samples (see Fig.6.1). However, the width of the distributions were different. For soft (polymer-like) films, there was a low intensity peak around 0.5 eV and a dominant peak around 1 eV. Both the peaks were narrow and therefore, it is possible to assume that there exist mainly two types of energy barriers in the system. Due to the abundance of bonded hydrogen and the long polymeric chains in the film (H/C $\sim$ 2), the test hydrogen atom experiences relatively similar environment between two minima at short distances. The mean distance between two minima is 1.6 Å and within which the neighbourhood looked more or less alike. This results in the narrow 1 eV peak. The lower energy peak corresponds to the jumps on the top surface.

In the case of a-C:H layers generated in MD simulations, the distribution was rather broad (increases upto 1 eV and then gradually falls off). This is due to the non-polymeric nature of the film where the test hydrogen atoms can sample vastly different neighbourhood. This difference can also be seen from the pair correlation function of the sample discussed in Chapter 5 (see Fig. 5.6), where the FGMC sample showed chain-like features where as MD sample was more amorphous in character.

The fraction of bonded and desorbed atoms depends crucially on the width of the distribution. This is because as the width increases the fraction of trap sites having higher ME also increases. The trapped fraction also depends on the number

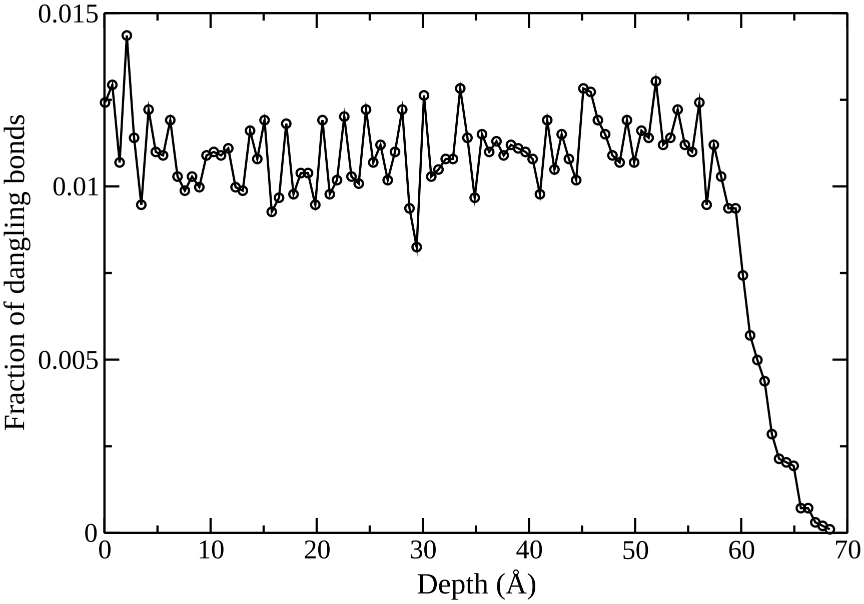

Figure 6.7: Depth profile of trap locations for the sample

of dangling bonds available as can be seen from Table. 6.3. This can also be understood from the diffusion coefficients given in Table. 6.4, where for 0.5 eV, the diffusion coefficient reduces by two orders of magnitude.

Independent of the incident flux, the depth profile of added H (see Fig. 6.6) was limited to 20 Å.This profile is nearly independent of the peak energy of the distribution. However, the depth profile of dangling bonds within the film (see Fig. 6.7) is extended upto 60 Å. Initially the incoming atoms attach to the dangling bonds on the near surface region (within the roughness scale). This results in the reduction of the number of dangling bonds on the surface. The atoms in the traps on the surface can also The atoms which are already occupying the traps perform surface jumps and have a high chance of meeting each other than diffusing in to the bulk. This makes the added hydrogen to reside mostly in the near surface region. This is in agreement with the reported values of thermal hydrogen profile in a-C:H layers of $\sim$ 1-2 nm [77].

The diffusion coefficient of hydrogen is relatively small in a-C:H layers (maximum $\sim 10^{-14}$ m^{2}s^{-1}) at room temperature, which is seven orders of magnitude lower than that reported in graphite [22]. This is because of the large inter-planar spacing

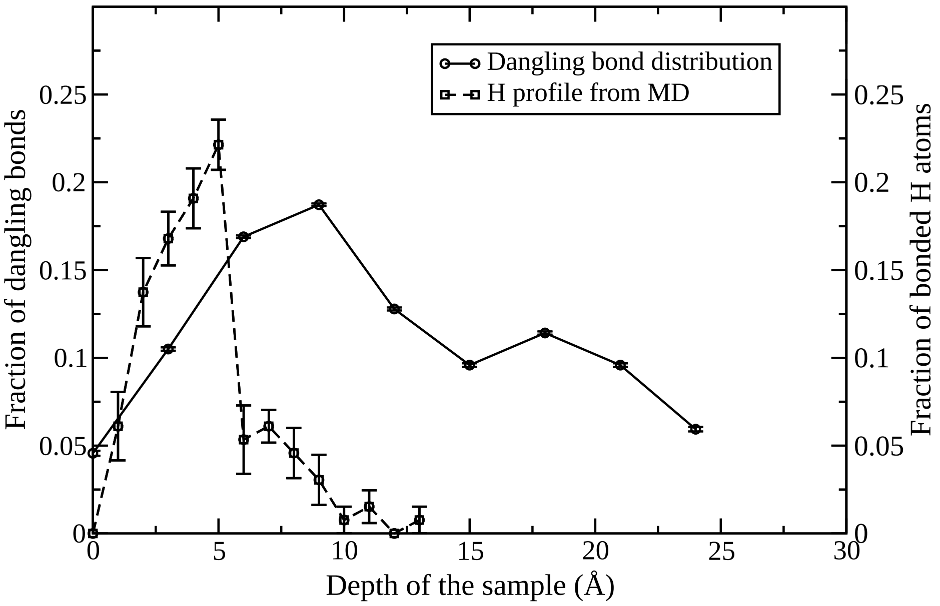

Figure 6.8: Depth profile of trap locations of MD sample.

between graphene layers in the graphite, where the H atoms can perform long jumps. For a film of 20 Å thickness, considering a diffusion coefficient of 10^{-14} m^2s^{-1}, the time for diffusion is, 0.0004 sec. Comparing this with the case of 0.5 eV simulation (from 6.4), it can be seen that the time to reach a depth profile is about 0.0002 sec. In the diffusion coefficient calculation, we have not considered the H–H and H–db recombination reactions. This could account the difference in the time between calculated and observed values of saturation time.

The hydrogen depth profile obtained in KMC simulations is compared with MD results and it was observed that the depth profile in MD also limited to 10-15 Å. The distribution of dangling bonds and the hydrogen profile is shown Fig. 6.8. The profile was generated by calculating the potential energy values of H atoms within the MD sample. Here also the H atoms attached to the dangling bonds on the surface and the further added H atoms are either reflected or formed H_2 molecules. The MD results are for 2000 H bombardment at 5 ps interval. Thus it can be seen that the mechanism which limits the profile of thermal H upto a few nanometers is the surface recombination of H atoms due to the adsorption desorption jumps.

6.6 Conclusions

In this chapter we discussed the reactive-diffusive dynamics of atomic hydrogen within the co-deposited layers using Kinetic Monte Carlo simulations. The migration energy distribution for hydrogen atoms was calculated by developing a technique based on the Potential Energy Surface analysis of the sample. The main insights from the study are the following.

The migration energy values depends on the type of the co-deposits. For soft polymer-like films the distribution found to have two peaks, one corresponds to 0.5 eV and other at 1 eV. This is due to the relatively similar neighbourhoods the H atoms experiences in a polymer-like deposit. The 0.5 eV peak corresponds to the surface of the film. For intermediate density amorphous films, the distribution found to have a broad peak due to the dissimilar neighbourhoods the hydrogen atom encounters.

The fraction of added and desorbed hydrogen found to have a strong dependence on the width of the distribution function. The diffusion coefficient of atomic hydrogen within the sample at 300 K is found to be of the order of 10^{-14} m^2s^{-1}. This is at least seven orders of magnitude less than that in graphite which is due to the lack of large scale porosity in the film.

The depth profile of added H atoms found to limit within 20-25 Å within the surface. This can be understood as a consequence of the adsorption and desorption processes. Once the deeper potential wells are occupied the remaining H atoms jumped and recombined on the surface. Thus they desorbed as H_2. Hence, though there are dangling bonds throughout the material, the hydrogen addition is limited to the near surface region.

The dangling bonds beyond the range of atomic hydrogen are potentially active sites and therefore, can recombine by thermal excitations. The excitations can arise from the bombardment of H atoms on the surface. This can result in the further H elimination from the deposits and consequently can lead to cross-linking between carbon atoms. These aspects are discussed in Chapter 7.

Chapter 7

Analytical Model for H Retention

`In this chapter we discuss a multi-region analytical model for film growth using the insights gained from atomistic as well as Monte Carlo simulations.`

7.1 Introduction

In the previous chapters we have investigated the microscopic aspects of how the film growth takes place and what are its characteristic features with respect to hydrogen and carbon composition. This was done using MD (for small space and time scales), then using KMC (for intermediate times scales) and using MC (long time scales). Therefore, there exists some integrated understanding of how the co-deposits form. One can notice that the structure of the film is very closely connected to hydrogen retention or rather its composition in terms of hydrogen and carbon contents. In this chapter we want to look at a different problem, namely the ultimate capacity to retain hydrogen. The problem is essentially motivated by the observations of relatively low H/C ratio (~ 1) observed in tokamaks compared to what one obtains in the FGMC simulations (~ 1.8).

While we developed the MC code, which is essentially a stacking of CH_3 radicals over each other, we also noticed the formation of chains consisting of few molecules (CH_2) of polymer type. The aspect of how these chains behave in the ultimate formation of the film could not be addressed because of the inherent complexity. Because these insights are available from the MD and the MC simulations, it is possible to make credible speculations on how the hydrocarbon chains will interact with each other and lead to the formation of the ultimate structure of the film.

We saw how important is the role played by the steric effects in the structure of the film. However, the feature of steric effect that has not been addressed so far is the mutual repulsion of H-atoms attached to the neighbouring chains. This is like a long-range repulsive force which cannot be captured in the interaction of a molecule and its immediate neighbourhood. In fact, as the radicals stick to each other, they most probably lead to the formation of chains before they can interlock with each other. So we expect to find chains in a real film in the regions of active growth.

We now wish to speculate on a reasonable mechanism which can explain the build up of the film in terms of the chains which interact with each other in a systematic process to bring down the H/C ratio to values that were observed in tokamaks. (One may note that, if we simply add CH_3 radicals in a polymeric fashion, the H/C ratio will approach 2, a number which is far higher than what was observed in tokamaks).

If we imagine the physical picture of the growth process, then CH_3 radicals attach themselves to the bound ones and the freshly attached radical itself becomes the host for the potential new addition. One of the interesting property that was investigated in previous chapters is the ability of the CH_3 molecule to rotate around the symmetry axis of the radical. These rotations allow it to explore configurations of lower potential energy, even at temperatures corresponding to 300 K. Extrapolating this argument further, a chain which is built up by CH_3 radicals can have a larger ‘sweeping area’. So we would like to propose a model for the film structure in which chains grow upto some extent, then lock and the network of the chains undergoes a relaxation.

The rest of the chapter is organized as follows. In Section (7.2) the model is discussed with supporting evidence from atomistic simulations. The Section (7.2.5) is devoted to the mathematical description of the model. Results are given in Section (7.3) and the discussion is in Section (7.4). The conclusions from the model is given

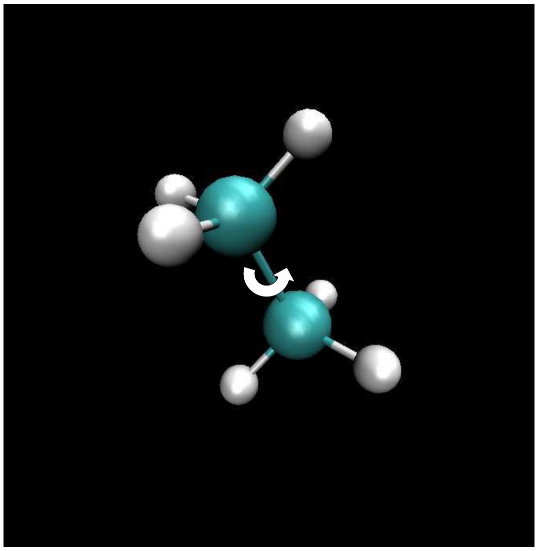

Figure 7.1: Rotation of CH_3 radical about C–C bond axis

in Section (7.5).

7.2 Model Description

In this section we propose a multi-species-multi-region model for the film growth by taking the insights gained from MD and MC studies discussed in the previous chapters. In the following section, we discuss the physical basis of the model.

7.2.1 Basis of the Model

7.2.1.1 Chain Formation and Locking

Recall that an attached CH_3 molecule (see Fig. 7.1) perform rotations about the C–C bond axis due to temperature and explore lower energy configurations. One key aspect of steric effect, namely the rotation of hydrocarbon chains, is not addressed so far in the previous chapters or by any other models [72]. However, MD simulations show the clear indication of this effect and as presented in Fig. 7.2.

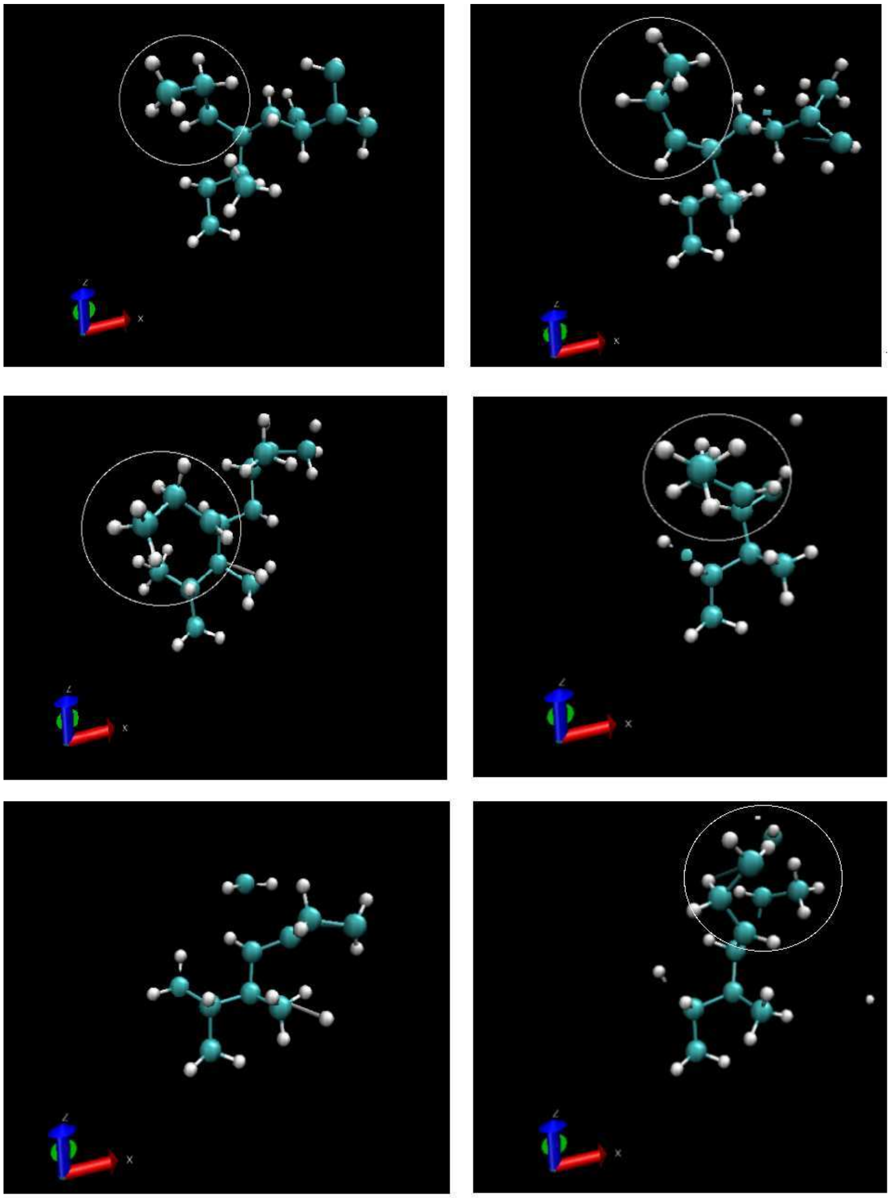

Figure 7.2: MD simulation of rotation of hydrocarbon chains on the surface. Blue: carbon, white: hydrogen

The rotating chains have a larger sweeping area and they may locked with other chains having dangling bonds. A schematic of the locking of chains is shown in Fig. 7.6. The dangling bonds are created by H abstractions due to the background hydrogen.

7.2.1.2 Long-Range Steric Effects

While developing the Monte Carlo model (as discussed in Chapter 5), we have seen that there must exist additional H elimination mechanisms to explain the reported values of H/C ratio. We propose that they are the consequence of long-range steric effects between hydrocarbon chains.

Let us consider a collection of hydrocarbon chains present in the film. The fast shower of hydrogen atoms on the top layers of the film can create perturbations in the system, which displaces the bound H atoms locally. The displacement of C atoms due to perturbation is not as significant due to its heavy mass. Once in a while when the displacements become in-phase (the atoms move away from each other) the potential energy of the system (see Fig. 7.3) may reduce so as to be able to eject a hydrogen atom. The MD simulations show that such a collective steric effect can change the potential energy of the system even upto 2 eV, which is sufficient to break the bound H atom from the surface.

This effect becomes prominent when the increase in the length of the chain. Thus, the chains should have sufficient length to experience this long-range effect. We have observed this effect while relaxing the FGMC films as discussed in Chapter 5.

7.2.1.3 Volume Steric Effects

The long-range (chain-chain) steric effects results in the compaction of the chains due to hydrogen eliminations and subsequent dangling bond recombination. This results in the cross-linking of chains and consequently reduces hydrogen content of the film. As the matter adds to the top layer, further compaction happens due to

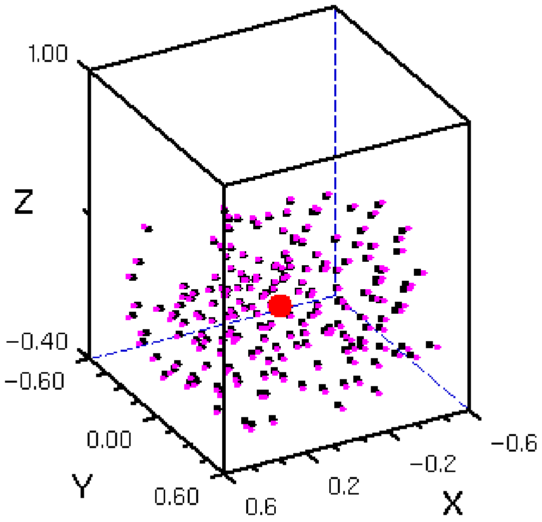

Figure 7.3: The displacement of H atoms due to constant perturbation of magnitude 0.04. Red: centre of mass, black: initial H atom locations, pink: H atom locations after perturbation.

the proximity of other atoms. We propose that this can lead to higher order steric effects namely, volume steric effects, results in additional H elimination. This effect becomes prominent between cross-linked carbon atoms and results in the further compaction of the film.

Considering the above discussed effects, it is possible to assume that there exists various regions in the film.

7.2.2 Description of Various Regions

We define four region of the film depending on the mechanism of growth and H elimination. They are:

- **h3-region**: In this region both the flux of atomic hydrogen and CH_3 radicals co-exist. It is also called 'top layer'. The hydrogen abstraction reactions create the dangling bonds and the incoming CH_3 radicals attaches to these locations resulting in the formation of linear hydrocarbon chains. The height of this layer is h_3 which is of the order of surface roughness of the film. We consider that the density and height of this layer are constant.

- **h2-region**: In this region chain-chain steric effects cause the hydrogen elimination and cross-linking. It is also called as 'middle layer' and the hydrogen flux penetrates into this layer. The height of this layer is h_2. The height and the density of the layer are assumed to be constant. Typically h_2 is of the order of few nanometers (as can be seen from Chapter 6, where we discussed the penetration range of atomic hydrogen).
- **h1-region**: Volume steric effects and subsequent H elimination happens in this layer. This region is called as 'intermediate layer'. We consider this also a region of fixed height h_1 and a fixed density. Energetic ion-bombardment can also cause additional H-eliminations in this region. Since there is no H flux in this region, the additional impacts results in the further compaction of the chains.
- **h0-region**: This is the bulk of the film which grows as a function of time. As the matter gets added into the top layer, the height of this layer h_0, increases, whereas the upper layers keeps their height constant. Hence after sufficient time, $h_0 >> h_1 + h_2 + h_3$. Subsequently, the retention is mainly decided by this region.

The schematic of various regions considered in the model is shown in Fig. 7.4.

7.2.3 Description of Various Species

The initial condition for the growth is that there already exists a thin layer of hydrocarbon film with dangling bonds. The CH_3 addition to the dangling bonds is the mechanism of the growth. This, along with H abstractions results in the formation of various species within the film.

Let C_0, C_1, C_2, C_3, D_1, D_2, D_3, D_4 and D_5 be the densities of various species considered in the model. They can be described as follows: (1) C_3: carbon with three

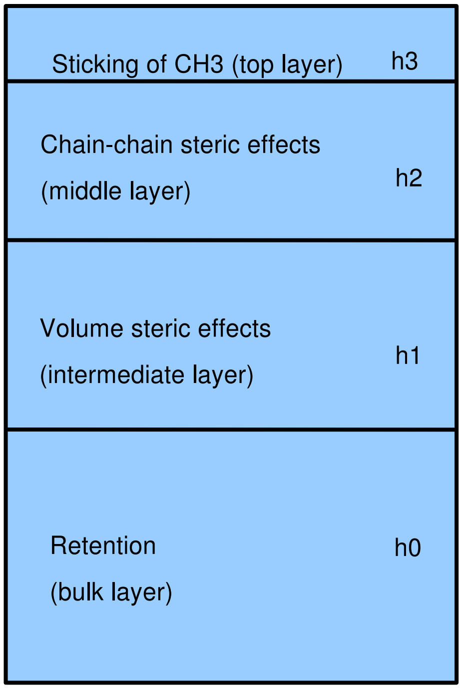

Figure 7.4: Schematic of the multi-layers considered in the model. At the steady-state, $h0 >> h1 + h2 + h3$

hydrogen, (2) C_2: carbon with two hydrogen, (3) C_1: carbon with one hydrogen, (4) C_0: carbon with no hydrogen, (5) D_1: chain with one C_2, (6) D_2: chain with two C_2, (7) D_3: chain with three C_2, (8) D_4: chain with four C_2 and D_5: chain with five C_2. The chains D_1,D_2,D_3 and D_4 are free ones whereas D_5 is locked. The schematic of various species considered can be seen in Fig.7.5.

7.2.4 Generic Analysis of the Growth

In this section we discuss the generic picture of growth and mass balance in the system. For simplicity let us consider a two-region model where, a top region of height h_1 (of unit exposed area) and density n_{kt} and a bottom region of height h_0 and density n_{kb}. The height and density of the top layer is assumed to be constant for simplicity. As the matter gets added , the height of the bottom layer increases.

The mass balance for such a system can be derived from the generic continuity equation of the form,

$$\frac{\partial n_k}{\partial t} = S_k - L_k \tag{7.1}$$

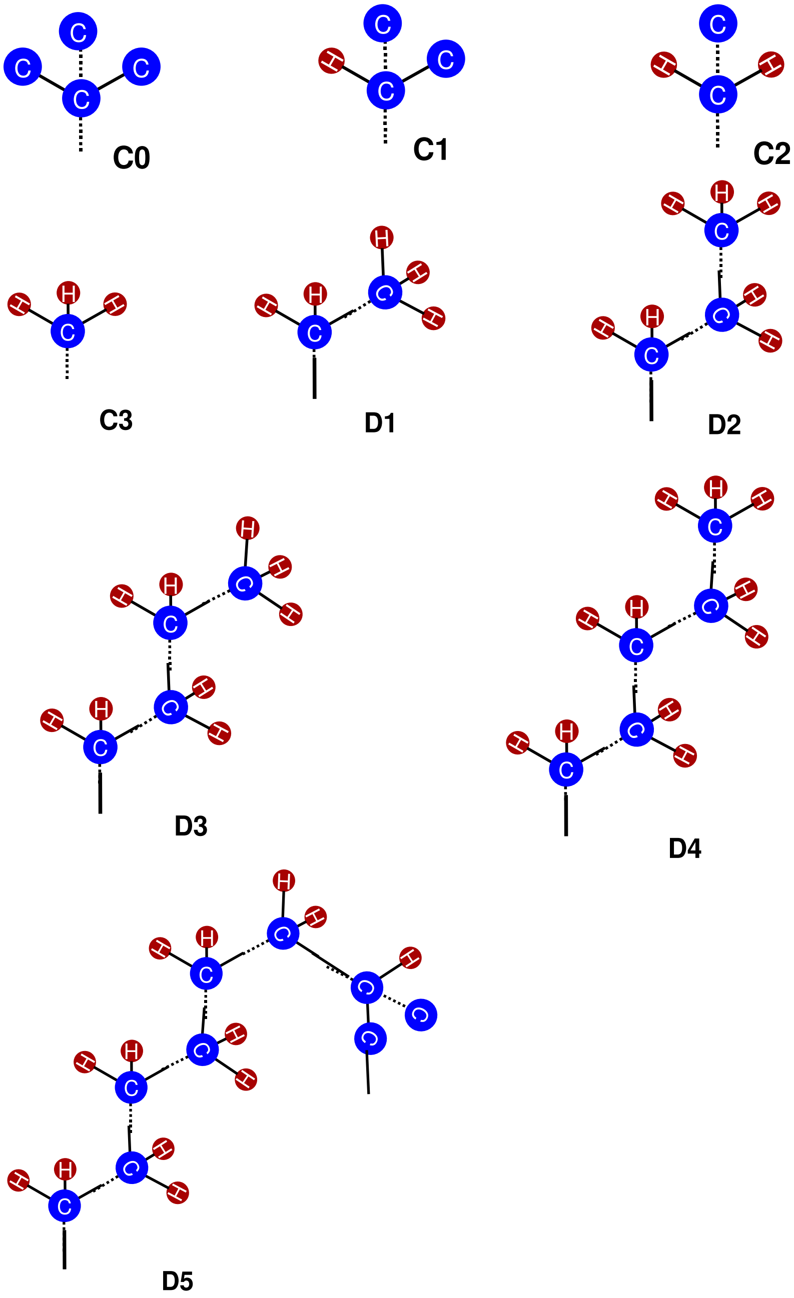

Figure 7.5: Schematic of various hydrocarbon species considered in the model

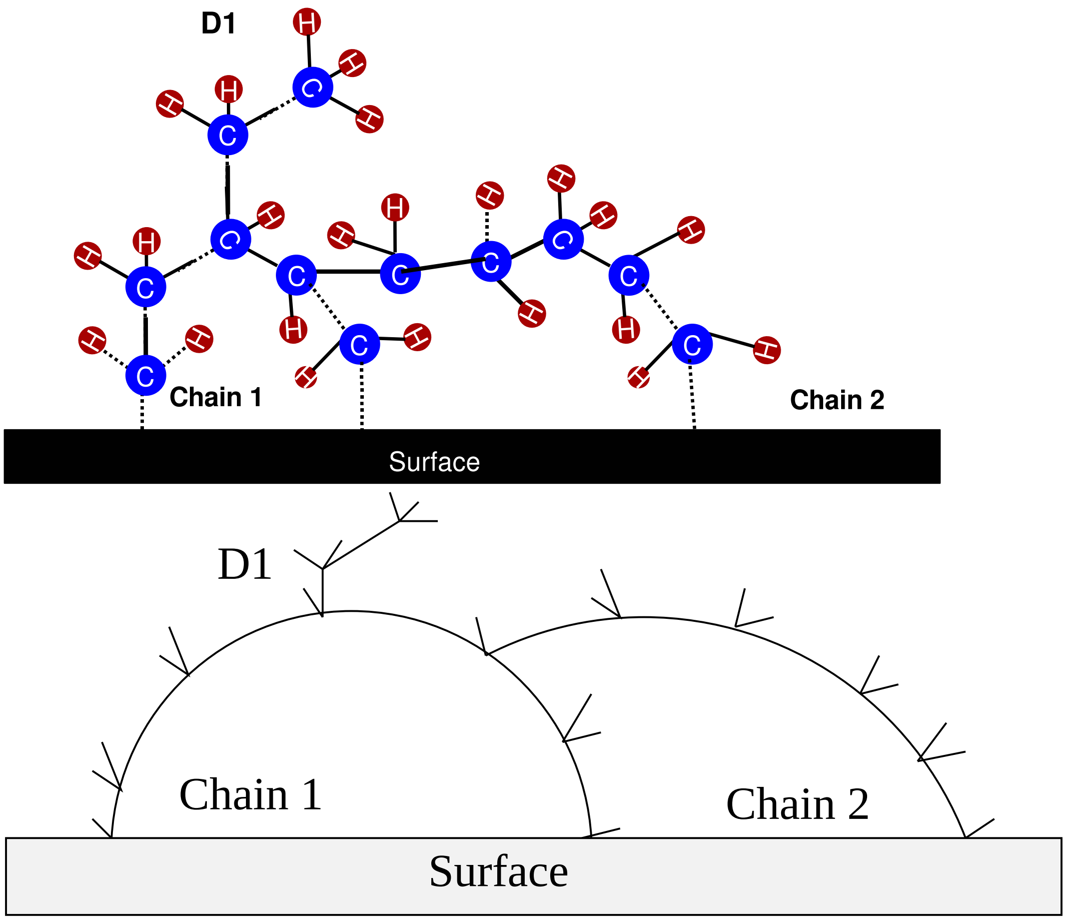

Figure 7.6: Schematic of locking of chains considered in the model. The second figure represents the simplified representation

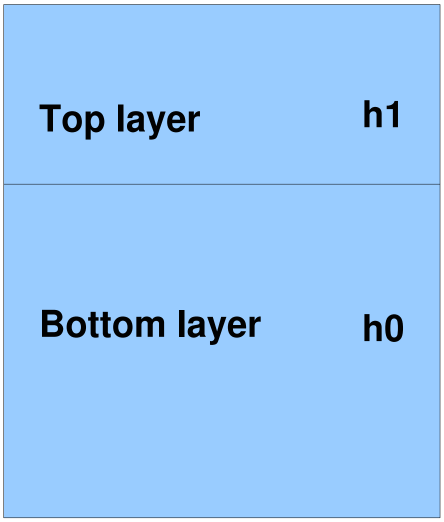

Figure 7.7: Schematic of the two-layer model of the film growth

where, S_k is the rate at which mass is added to the system and L_k is the rate of loss of mass for the layer of density n_k. Let $n_{kb}\Delta h_0$ be the number of particles added to the bottom region in Δt causing a change in height Δh_0. There is no physical movement of species across the region (also no other additional loss of particles) and hence L_k is zero. We also make an assumption that the density of the layer is a constant, which makes $\dot{n}_k$ is zero. The change in height of the bottom layer, can be obtained by integrating the equation (7.1) for a distance Δh_0 as follows.

$$n_{kb}\Delta h_0 = S_{kt}h_1\Delta t \tag{7.2}$$

where, the mass addition in the top layer increases the height of the bottom layer. Thus the rate of change of height of this layer is

$$\dot{h}_0 = \frac{S_{kt}h_1}{n_{kb}} \tag{7.3}$$

which is the rate of growth of the film. This concept is used in the present multi-region model discussed in the next section for different species and regions.

7.2.5 Model Equations

We consider a zero dimensional time dependent system of equations for describing the time evolution of the species listed above in each region. In each region different processes are considered which lead to the hydrogen elimination from the film. Let us consider a unit cross-sectional area so that the volume of the respective regions are h_3, h_2, h_1 and h_0 from the top to the bulk layers respectively. The addition of CH_3 on C_2 species results in the generation of C_1. The original C_2 type atom becomes C_1 type and the chain starts growing from this location. CH_3 additions to the chain results in the formation of D_1. Further CH_3 additions to D_1 results in D_2, D_3 and D_4 (see Fig. 7.5). All the chains start with C_1 and end with C_3.

We make a very important assumption that, the chain represented by D_4 has enough energy to explore its neighbourhood and get attached (locked) with another

C_2 atom. This can happen due to the presence of background hydrogen which keeps creating dangling bonds. The reason for considering the growth only upto D_4 is that, the average distance between dangling bonds on the surface, calculated from FGMC was about 10 Å. Considering all the bonds will have equal probability to grow chains, the maximum chain length one can grow on average is 5 Å, which corresponds to D_4 structure.

The locking of the chain is shown in Fig. 7.6 where one can see that D_4 is locked with C_2 of another locked chain. This results in the formation of C_1 and D_5. Apart from the chains, we also consider the reactions between C_2 and C_2, C_2 and C_1 and C_1 and C_1 in the model.

In the model equations, we use the following notations to indicate the species in a specific layer. For example, C_{2t} implies C_2 species in the top layer. Similarly, the subscripts for the remaining layers are: '*m*' for the middle layer, '*i*' for intermediate layer and '*b*' for bottom layer.

7.2.5.1 Top Layer

Let Γ_{CH_3} be the flux of incoming radicals and ν_g be the growth rate (rate of addition of CH_3) of the chains, which is assumed to be equal for simplicity for all the chains upto D_4.

The reactions considered in this layer are as follows:

- Growth: this term is written as ν_g which is as follows:

  $$\nu_g = 3 f_{db} \sigma_{db} \Gamma_{CH_3} \tag{7.4}$$

  where f_{db} is the fraction of dangling bonds and σ_{db} is the cross-section of dangling bonds on the tri-hydride locations (The factor 3 indicates three hydrogen attached to the carbon). The fraction of dangling bond is obtained from the hydrogen abstraction probability.

- Locking: D_4 is assumed to lock with C_2, which can be written as follows:

  $$S_l = 2f_{db}\sigma_{chain}v_{chain} \tag{7.5}$$

  where, S_l is the rate of locking and v_{chain} is the chain velocity with which it explores the neighbourhood by rotation. The cross-section for sticking is given by σ_{chain}. The rate of locking also depends on the dangling bonds on C_2 which has two hydrogens and this is indicated by factor 2.

The time evolution of the densities in this region are as follows:

$$\begin{aligned} \dot{C}_1 &= S_l D_4 C_2 + \nu_g C_2 && (7.6) \\ \dot{C}_2 &= S_l D_4 C_2 - \nu_g C_2 && (7.7) \end{aligned}$$

where, $S_l D_4 C_2$ represents the locking of D_4 creates C_1 and $\nu_g C_2$ represents the growth on C_2 to form C_1.

$$\begin{aligned} \dot{C}_3 &= \nu_g \left(C_2 - C_3\right) && (7.8) \\ \dot{D}_1 &= \nu_g \left(C_3 - D_1\right) && (7.9) \\ \dot{D}_2 &= \nu_g \left(D_1 - D_2\right) && (7.10) \\ \dot{D}_3 &= \nu_g \left(D_3 - D_4\right) && (7.11) \\ \dot{D}_4 &= \nu_g D_3 - S_l D_4 C_2 && (7.12) \end{aligned}$$

In the steady-state the LHS is zero and the solutions are $C_2 = C_3 = D_1 = D_2 = D_3$ which is taken to be a constant D. Substituting in equation (7.12), D_4 can be written as,

$$D_4 = \frac{\nu_g}{S_l} \tag{7.13}$$

From equations (7.4 and 7.5) D_4 can be written as

$$D_4 = \frac{3}{2}\frac{\sigma_{db}}{\sigma_{chain}}\frac{v_{CH_3}}{v_{chain}}n_{CH_3} \tag{7.14}$$

Thus D_4 relates the vapour phase density to the surface density of the film. The velocity of the chain $v_{chain} \ll v_{CH_3}$ and $\sigma_{chain} \ll \sigma_{db}$. Thus, $D_4 \gg n_{CH_3}$ and D_4 approaches the surface density of the film. Substituting D in equation (7.6), $\dot{C_2}$ becomes zero and C_2 is a constant.

After the locking we imagine that five C_2 atoms are added into the film. Since the growth and locking had consumed two C_2 atoms, we retain two C_2s (to maintain the mass balance of the top layer) and three are considered to be added in the region below. The three C_2s generated in the top region are transferred to the middle layer and on the two further growth takes place. Thus, C_2s in this region is kept constant.

7.2.5.2 Middle Layer

In the middle layer, long-range steric repulsion causes H eliminations. This results in the formation of C_1 out of C_2. This can be represented by the following equation:

$$\dot{C_{2m}} h_2 = 3\nu_g C_{2t} h_3 - 2\alpha_2 C_{2m}^2 h_2 = x_2 \tag{7.15}$$

where, α_2 is the rate of recombination of C_2. The first term in the RHS of equation (7.15) represents the source from the top layer. The second term is the recombination of C_2 to form C_1. We assume that these two terms will not balance each other. If they remain unbalanced, the excess C_2 of this region will be transferred to the intermediate layer. This is represented by x_2, which is zero or positive. Similarly for C_1,

$$\dot{C_{1m}} h_2 = 2\nu_g C_{2t} h_3 + 2\alpha_2 C_{2m}^2 h_2 = y_2 \tag{7.16}$$

where, y_2 is the net addition of atoms in the middle region of C_1 type. This becomes the source for intermediate region. The first term in the RHS of equation (7.16) represents the C_1 passed from the top layer and the second term is from C_2 recombination resulting in C_1 formation.

7.2.5.3 Intermediate Layer

In the intermediate layer, therefore exists C_1, C_2 from the upper layers and C_0, generated by the recombination of C_1 species. C_2–C_1 recombination also generates C_0.

The rate of change of C_2 in this region can be written as,

$$\dot{C_{2i}}h_1 = x_2 - \beta C_{1i} C_{2i} h_1 = x_1 \tag{7.17}$$

where, β represents the rate of recombination of C_2 and C_1 to create C_0 from volume steric effects and x_2 represents the mass addition from the middle layer. The second term represents the C_1–C_2 recombination which is generating C_0 and the C_1 is retained. Thus it will not appear as a source in C_1 equation. When the terms remain unbalanced, the excess C_2 will be transferred to the bulk layer, which is represented by x_1, which can have be either zero or positive.

The evolution of C_1 can be written as,

$$\dot{C_{1i}}h_1 = y_2 - 2\alpha_1 C_{1i}^2 h_1 = y_1 \tag{7.18}$$

where, α_1 is the C_1–C_1 recombination rate to form C_0 and y_2 represents the addition of C_1 from the middle layer. The second term represents the C_0 generation from C_1 recombination. The excess C_1 passing to the bulk layer is y_1, which will also be either zero or positive.

The recombination reactions generate C_0, which is given by equation (7.19). The C_0 transferred to the bulk is given by z_1.

$$\dot{C_{0i}}h_1 = 2\alpha_1 C_{1i}^2 h_1 + \beta C_{1i} C_{2i} h_1 = z_1 \tag{7.19}$$

7.2.5.4 Bulk Layer

In the bulk of the film, all the three components C_2, C_1 and C_0 are present. The height of the layer h_0 increases with the addition of these mass into the bulk layer.

The steady-state mass addition to the bulk can be written as follows.

$$C_{2b}\dot{h}_0 = x_1 \tag{7.20}$$

$$C_{1b}\dot{h}_0 = y_1 \tag{7.21}$$

$$C_{0b}\dot{h}_0 = z_1 \tag{7.22}$$

By substituting for x_1, y_1 and z_1 in the above equations and adding them, the rate of change of height of the bulk layer can be obtained.

$$\dot{h}_0 = \frac{5\nu_g C_{2t} h_3}{(C_{ob} + C_{1b} + C_{2b})} \tag{7.23}$$

Thus it can be seen that at the steady-state, the rate of change of the height of the film is decided by the total mass addition in the top layer which is a constant for a given flux. Equations (7.20) to (7.22) can be normalized and written as follows:

$$\begin{aligned} Z_2 &= \frac{3}{5} - l_2 - l_{12} && (7.24) \\ Z_1 &= \frac{2}{5} + l_2 - l_1 && (7.25) \\ Z_0 &= l_1 + l_{12} && (7.26) \end{aligned}$$

where the substitutions are,

$$\begin{aligned} C &= C_{ob} + C_{1b} + C_{2b} \\ Z_2 &= \frac{C_{2b}}{C}, Z_1 = \frac{C_{1b}}{C}, Z_0 = \frac{C_{0b}}{C} \\ Z_{2t} = \frac{C_{2t}}{C}, Z_{2m} &= \frac{C_{2m}}{C}, Z_{2i} = \frac{C_{2i}}{C}, Z_{1i} = \frac{C_{1i}}{C} \\ q_2 = \frac{2\alpha_2 h_2}{5\nu_g h_3} C, q_1 &= \frac{2\alpha_1 h_1}{5\nu_g h_3} C, q_{12} = \frac{\beta h_1}{5\nu_g h_3} C \\ l_2 = q_2 Z_{2m}^2, l_1 &= q_1 Z_{1i}^2, l_{12} = q_{12} Z_{1i} Z_{2i} \end{aligned} \tag{7.27}$$

The values of Z_2, Z_1 and Z_0 lies between 0 and 1. The H/C ratio of the film is the solution of equations (7.24 to 7.26). Since Z_2 has two hydrogens and Z_1 has one

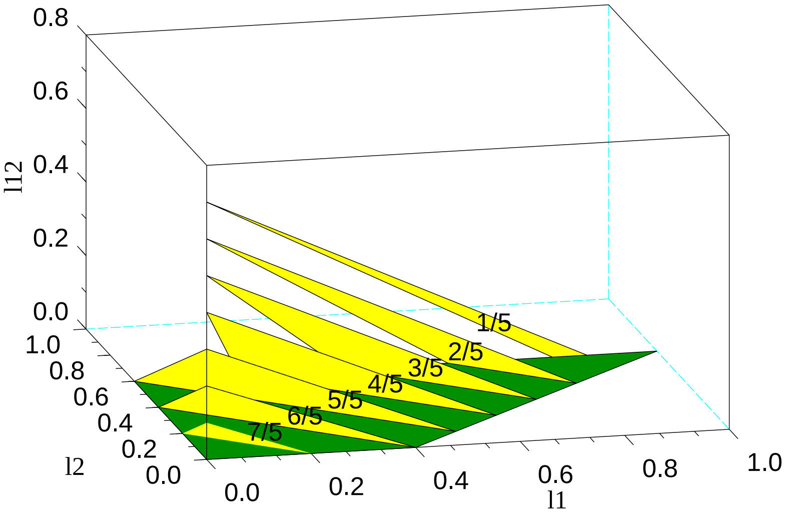

Figure 7.8: Constant H/C planes for different l_1, l_2 and l_{12} values (yellow color). Green represents the region of permissible solutions.

hydrogen, the H/C ratio can be written as $2Z_2 + Z_1$, which can be represented as below.

$$H/C = 8/5 - (l_1 + l_2 + 2l_{12}) \tag{7.28}$$

The values of l_1, l_2 and l_{12} are varied as independent parameters in such a way that sum of the three can be maximum of 8/5. The values of l_1 vary between 0 to 1, whereas l_2 and l_3 lie between 0 to 0.6. Accordingly it can be seen that extreme values of H/C ratio are 0 and 1.6.

7.3 Results

The solutions of the equations (7.24 to 7.26) gives H/C values as a function of the parameters l_1,l_2 and l_{12}. Fig. 7.8, shows the constant H/C planes as a function of these parameters. It can be seen that, the permissible solutions (where z_2, z_1 and z_0 are either zero or positive) are limitted to a narrow range of l_1, l_2 and l_{12}. For H/C values greater than 1 (5/5 in the plot), the constant H/C planes are complete triangles with $l_1 \leq \frac{2}{5}$, $0 \leq l_2 \leq \frac{3}{5} - l_1$ and $l_{12} = \frac{3}{5} - l_2$. For lower H/C values, the

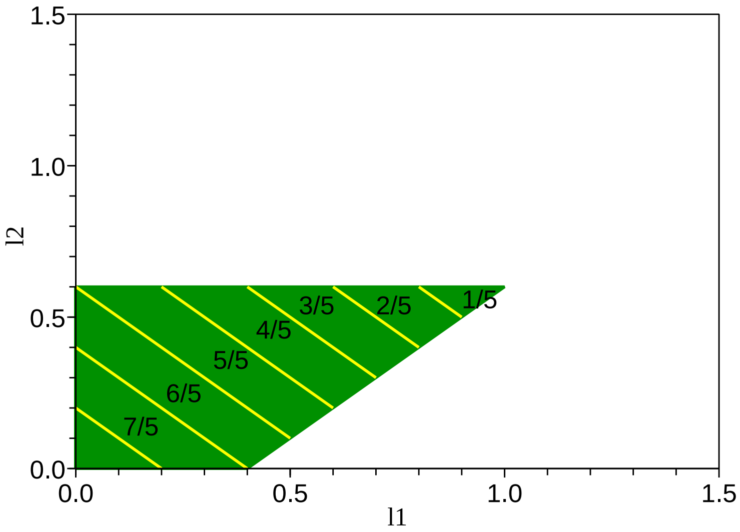

Figure 7.9: 2D projection of the constant H/C contours for different l_1 and l_2 values (yellow color). Green represents the region of permissible solutions.

triangle is cut by the plane passing through $(\frac{2}{5}, 0, 0)$.

The 2D projection (into l_1-l_2 plane) of the constant H/C planes is shown in Fig. 7.9. It can be seen that the parametric range is getting narrower for lower H/C values.

7.4 Discussion

There exists a restricted region of parameter space, where the possible solutions exist for the equations (7.24 to 7.26) (see Fig. 7.8). The H/C ratio calculated from the model found to show a variety of values depending on the choice of the parameters l_1, l_2 and l_{12}. The maximum H/C ratio obtained from the model is 1.6, which is slightly higher than the reported H/C values of co-deposits (1.5). This corresponds to a condition where, middle (`h2-region`) and intermediate (`h1-region`) layers do not contribute, and the film grows only from the chains. There is no additional compaction occuring during the growth. This results in a very loosely packed film of high porosity. Such films are typically generated by FGMC code (with density $<$ 1 gm/cc), where there are no additional compaction reactions.

If $l_2 = 0$, then there is no C_2 to C_1 conversion by chain-chain recombination. However, there can be C_2–C_1 and C_1–C_1 recombination. This indicates diffused middle and intermediate layers. The H/C ratio of the films varies between 0 and $\frac{8}{5}$. However, if l_2 does not exist, then l_{12} will be small since there is no additional source of C_1 formation. This makes l_1 a still smaller quantity. Thus, in reality H/C ratio will not approach zero, unless ion-bombardment causes additional abstraction.

If there exist a dense middle layer, then, $l_2 = \frac{3}{5}$ and therefore l_{12} has to become zero. This corresponds to a condition, where l_1 varies between 0 and 1. Accordingly H/C ratio varies between 1 and 0. If there is no intermediate layer (`h1-region`), then the film will be of completely C_1 and thus H/C ratio becomes one. This corresponds to the observed stoichiometric limit of polymer-like films (~ 1). The density of such films is typically between 1–1.5 gm/cc.

On the otherhand if there is a dense intermediate layer, then there will be a complete conversion of C_1 to C_0 and H/C drops down to 0. This corresponds to pure carbon films generated by ion-bombardment such as Diamond Like Carbon (DLC) films with density close to 3 gm/cc.

7.4.1 Comparison with Tokamak Observations

Though the limits are known, the nature of the film and the H/C ratio are decided by the conditions under which the films are grown. Different tokamaks have reported different H/C ratio, depending on the vapour phase and physical conditions. In the case of hydrogen rich co-deposits reported in JET (H/C $\sim$ 1.5), ASDEX ($\sim$ 1.4) *etc.*, these films are observed in the remote regions of tokamak, where there is no ion-bombardment [25, 26, 30, 32]. This results in the absence of the term α_1 and consequently l_1. Thus, even if there is a dense middle layer, the minimum H/C ratio could be observed is 1. Depending on the density of middle layer, H/C ratio varies between 1 and less than 1.6 ($l_2 < 3/5$). This is typically observed in the remote regions of the devices.

On the other hand, if we consider the reports from TORE SUPRA, DIII-D, TEXTOR *etc.*, the co-deposits were observed in mainly the plasma-exposed regions where there is a flux of energetic particles [**?**, 26, 43, 147]. This results in the elimination additional hydrogen from the intermediate layer and α_1 becomes significant. This results in the formation of hydrogen-less films with very low H/C ratio (upto 0.1).

7.5 Conclusions

In this chapter we have discussed a simple analytic multi-region multi-species model for the growth of co-deposited layers. The model is based on the insights derived from MD and MC simulations and the idea that short polymeric chains grow, lock with each other and compactify. It is interesting to note that, one can arrive at a more realistic (~ 1) H/C as observed in some of the tokamaks. The model brings out the importance of long-range steric effects in the structure formation. Constraints for achieving small H/C ratio is also brought out.

Chapter 8

Conclusion

In this thesis, the studies on the fundamental processes leading to the erosion and growth of hydrogenated carbon films have been reported, which are of particular interest considering the overall inventory of fuel in fusion reactors.

The role of steric effects in the growth and erosion of films is clearly brought out in the present study. The steric effects arise from the mutual repulsion between H atoms attached to different carbon atoms within the film. One of the most important conclusion from the study is that, the steric effects play a crucial role right from the radical incorporation, which is the very initial step of the growth at the atomistic level, all the way upto the ultimate structure and the hydrogen retention capacity of the film.

In the atomistic picture, the CH_3 radicals are added to the dangling bond locations of the film in a way to minimize the steric repulsion. The molecule performs rotation about C–C bond axis during its incorporation. The incorporation is possible only if the distance between H atoms attached to the CH_3 and the surface bound H atoms are above a critical distance called d_{crit}, which is typically 1.6 Å. The surface irregularities shadow the dangling bond locations locally and hence reduces the sticking probability.

How this atomic level picture of steric effects lead to the final structure of the film is also brought out in the study with the help of Monte Carlo simulation. The soft hydrocarbon films are formed in a background of atomic hydrogen and hydrocarbon radicals. The atomic hydrogen creates dangling bonds on the surface. However, steric effects prevent the radical incorporation on certain dangling bond locations. This makes some dangling bonds unoccupied and hence leads to the microporosity of the film. Apart from the microscopic steric effects, the far-neighbour-shadowing (non-local) created by the tall structures also contributes to the structure of the film. The far-neigbour-shadowing results in the formation of bigger pores. Thus, steric effects and shadowing together lead to the structure of the film. This model is able to show the formation of a-C:H layers of a wide variation of densities (between 1 to 1.6 gm/cc) which are typical of soft hydrocarbon films.

Other than the local steric effects arising from the interaction of the molecule and its immediate neighbourhood, the present study also addresses the effect of long-range steric effects arising in the film. The stacking molecules on the top of each other leads to the formation of linear hydrocarbon chains. The chains also perform rotations with a larger sweeping area. The hydrogen atoms attached to the chains will experience repulsion, which can lead to additional hydrogen eliminations from the film. This reduces the hydrogen content of the film and the structure becomes compact. Consequently, one can arrive a more realistic H/C ratio (~ 1) which is typical of soft polymer-like films.

The role of steric effects in the chemical sputtering of films is also understood. Based on this a new mechanism is identified for the synergistic erosion of hydrocarbon films due to energetic ions and thermal hydrogen atoms. The mechanism, namely, *Hydrogen Enhanced Physical Sputtering (HEPS)*, can be explained as a consequence of successive bond breaking due to energetic ions and passivation due to the thermal H atoms. The steric repulsion arising from bound H atoms prevents the re-attachment of the broken bonds within the film. The subsequent ion bombardment cause the ejection of energetic, unsaturated molecules from the top layers of the film. The resulting erosion yield is much higher than the yields for pure chemical erosion due to thermal H atoms and pure physical sputtering due to energetic ions. The role of chemical and momentum transfer process in the erosion yield is also clearly understood from the study. This model is found to be capable of explaining the enhanced erosion yields observed in radical beam experiments.

Another conclusion from the present study is that the dynamics of hydrogen within the film depends strongly on the structure of the film which in turn depends on the Migration Energy (ME) of the film. A method based on Potential Energy Surface (PES) analysis of the film shows that for a-C:H films migration energy is a distribution peaked around 1 eV. The width of the distribution depends on the atomic arrangement in the film. For soft polymer-like films (of density 1.2 gm/cc, the long hydrocarbon chains makes nearly similar environment everywhere and consequently ME distribution has a narrow peak (0.01 eV). Whereas, for intermediate density (1.8 gm/cc) films, the distribution was rather broad (0.45 eV) indicating a variety of atomic arrangements. The H dynamics is a sequence of adsorption-desorption processes on the surface of the film (internal surfaces of pores as well). We can conclude that two competing processes, namely hydrogen attachment to the dangling bonds and H–H recombination decides the range of atomic hydrogen within the film (2–3 nm).

The comparison of roughness scaling showed good agreement between the film formed from standard ballistic model of deposition and the Monte Carlo simulations using detailed atomic structure of the molecules. Thus we conclude that the microstructure of the film will not depend on the behavior of roughness in the system.

To summarize, we have investigated the growth and erosion of hydrocarbon co-deposits formed in the remote regions of tokamak using both numerical and analytical methods. The steric repulsion arising from H atoms found to be an important effect in deciding the ultimate structure and hydrogen retention capability of the hydrocarbon films.

8.1 Future Scope

Several points arise from this work, which suggest the extension of the present analysis as follows.

- It will be interesting to extend the present work to higher hydrocarbons as they can also actively participate in the growth.
- In the present Monte Carlo model of the growth, it will be interesting to keep the effects of adjustments arising from neighbouring atoms during the process of radical incorporation.
- A relevant immediate extension is the problem of mixed-material co-deposition where the first-wall will be made up of different materials such as beryllium, tungsten *etc.*

Appendix A

Creation of a-C:H sample in MD

The Hydrocarbon Parallel Cascade code (HCParCas version V3.22) has been used which employs a fifth-order predictor-corrector Gear algorithm to calculate the positions and velocities of particles using adaptive time steps [101]. The a-C:H samples were created by annealing a collection of carbon and hydrogen atoms using the Brenner potential for C–H and C–C interactions [99, 100]. The initial sample contained 1000 randomly positioned atoms separated at a distance greater than 1.1Å, the length of C–H bond.

The sample was annealed several times from 300 K to 4000 K and back to 300 K at a rate of 0.01 K/fs. Berendsen scalings [104] were used for temperature and pressure control, and periodic boundary conditions were applied along the X, Y and Z directions of the sample. After 50 ns annealing at 300 K the periodic boundary along the Z axis was removed, followed by another 7 ns of equilibration time to cure the artificially broken bonds. Atoms within a distance of 3 Å of the bottom of the cell were fixed for mimicking the effect of an underlying bulk layer. Also, the prolonged relaxation helped to identify and remove H_2 molecules formed within the sample during annealing.

As next step of the surface creation, the sample was bombarded with low energy (5 eV) Ar atoms with random impact angles and locations to get rid of loosely bound C atoms on the surface, which arise due to the removal of periodic boundary conditions along the z axis. Finally, to mimic the experimental conditions, the surface was exposed to a flux of thermal H atoms.

Bibliography

[1] P. C. Stangeby. The plasma boundary of magnetic fusion devices. *Plasma Physics series, Institute of physics publishing*, (2000).

[2] M. Mayer, V. Rohde, A. von Keudell, and ASDEX Upgrade Team. Characterisation of deposited hydrocarbon layers below the divertor and in the pumping ducts of ASDEX Upgrade. *J. Nucl. Mater.*, 313-316:429–433, (2003).

[3] C. Brosset, H. Khodja, and Tore Supra team. Deuterium concentration in deposited carbon layers in ToreSupra. *J. Nucl. Mater.*, 337–339:664–668, (2005).

[4] K. Nordlund. Introduction to atomistic simulations. *http://www.acclab.helsinki.fi/∼ knordlun/atomistiset*, (2003).

[5] A. Rai. Dynamic monte-carlo modeling of hydrogen isotope reactive-diffusive transport in porous graphite. *Ph.D thesis submitted to Ernst–Moritz–Arndt University*, (2007).

[6] John Wesson. Tokamaks (third edition), oxford science publishing. *Oxford University Press*, (2004).

[7] J. D. Lawson. Some criteria for a power producing thermonuclear reactor. *Proceedings of the physical society*, B 70(6), (1957).

[8] ITER Organization. http://www.iter.org.

[9] C.M. Bishop. Stability of localized mhd modes in divertor tokamaks- a picture of the h-mode. *Nuclear Fusion*, 26(8):1063–1072, (1986).

[10] D.N. Hill. A review of elms in divertor tokamaks. *J. Nucl. Mater.*, 241–243:182–198, (1997).

[11] B. Lipschultz. Review of marfe phenomena in tokamaks. *J. Nucl. Mater.*, 145–147:15–25, (1987).

[12] J. F. Drake. MARFES: Radiative condensation in tokamak edge plasma. *Physics of Fluids*, 30:2429–2433, (1987).

[13] Shishir P. Deshpande. Ph.d thesis submitted to gujarat university, india. (1992).

[14] G. Federici et. al. Plasma-material interactions in current tokamaks and thier implications for next–step fusion reactors. *Nuclear Fusion*, 41(12R):1967–2137, (2001).

[15] E. Tsitrone. Key plasma wall interaction issues towards steady state operation. *J. Nucl. Mater.*, 363–365:12–23, (2007).

[16] G. Federici. Plasma wall interactions in iter. *Phys. Scr.*, T124:1–8, (2006).

[17] W. Eckstein. Computer simulations of ion–solid interactions. *Springer series in material science 10, Springer-Verlag*, (1991).

[18] W. Eckstein, C. García-Rosales, J. Roth, and W. Ottenberger. Sputtering data. *Rep. IPP 9/82, Max-Planck-Institut für Plasmaphysik, Garching, Germany*, (1993).

[19] J. Küppers. The hydrogen surface chemistry of carbon as a plasma facing material. *Surface Science Reports*, 22:249–321, (1995).

[20] W. Jacob and J. Roth. Chemical sputtering. *Springer-Verlag*, pages 319–375, (2007).

[21] G. Federici and C.H. Wu. Modelling of plasma hydrogen isotope behavious in porous materials (graphites/carbon-carbon composites). *J. Nucl. Mater.*, 186:131–152, (1992).

[22] M. Warrier. Multi–scale modeling of hydrogen isotope transport in porous graphite. *Ph.D thesis submitted to Ernst–Moritz–Arndt University*, (2004).

[23] A. Hassanein, B. Wiechers, and I. Konkashbaev. Tritium behaviour in eroded dust and debris of plasma-facing materials. *J. Nucl. Mater.*, 258-263:295–300, (1998).

[24] W. Jacob. Redeposition of hydrocarbon layers in fusion devices. *J. Nucl. Mater.*, 337-339:839, (2005).

[25] J.D. Elder *et.al.* J.P. Coad, N. Bekris. Erosion/deposition issues at jet. *J.Nucl. Mater.*, 290–293:224–230, (2001).

[26] T. Loarer. Fuel retention in tokamaks. *J.Nucl. Mater.*, 390–391:20–28, (2009).

[27] *Nucl. Fus.*, 47, (2007).

[28] E. Tsitrone, C. Brosset, and J. Bucalossi et. al. Deuterium retention in tore supra long discharges. *Proceedings, 20th IAEA Fusion Energy Conference, Vilamoura, Portugal, 1-6 Nov.*, IAEA-CN-116/EX/10-2, (2004).

[29] M. Mayer, M. Balden, and R. Behrisch. Deuterium retention in carbides and doped graphites. *J. Nucl. Mater.*, 252:55–62, (1998).

[30] V. Rohde, M. Mayer, J. Likonen, and R. Neu *et.al.* Carbon erosion and a:c-h layer formation at asdex upgrade. *J. Nucl. Mater.*, 337–339:847–851, (2005).

[31] W.R. Wampler, S.L. Allen, A.G. McLean, and W.P. West. Measurements of carbon, deuterium and boron deposition in $\mathrm{DIII-D}$. *J. Nucl. Mater.*, 337–339:134–138, (2005).

[32] V. Rohde, H. Maier, K. Krieger, R. Neu, and J. Perchermaier *et.al.* Carbon layers in the divertor of asdex upgrade. *J. Nucl. Mater.*, 290–293:317–320, (2001).

[33] D. Naujoks, R. Behrisch, J.P. Coad, and L.C.J.M. De Kock. Material transport by erosion and redeposition on surface probes in the scrape off layer of JET. *Nuclear Fusion*, 33(4):581–590, (1993).

[34] M. Mayer, P. Wienhold, D. Hildebrandt, and W. Schneider. Erosion and deposition at the alt-ii limiter of textor. *J. Nucl. Mater.*, 313–316:377–382, (2003).

[35] A. Yoshikawa, Y. Hirohata, Y. Oya, and T. Shibahara *et.al.* Hydrogen retention and depth prole in divertor tiles of jt-60 exposed to hydrogen discharges. *Fusion. Engg. Design.*, 81:289–294, (2006).

[36] A. Tabasso, G.F. Counsell, D. Hole, and J.P. Coad. Observations of hydrocarbon lm deposition in the mast tokamak. *J. Nucl. Mater.*, 306:73–77, (2002).

[37] B. Lipschultz, D.G. Whyte, J. Irby, B. LaBombard, and G.M. Wright. Hydrogenic retention with high-z plasma facing surfaces in alcator c-mod. *Nucl. Fusion*, 49:045009–1–18, (2009).

[38] C.H. Skinner, C.A. Gentile, G. Ascione, and A. Carpe *et.al.* Studies of tritiated co-deposited layers in tftr. *J. Nucl. Mater.*, 290–293:486–490, (2001).

[39] K. Sugiyama, T. Tanabe, C. H. Skinner, and C. A. Gentile. Measurement of tritium surface distribution on tftr bumper limiter tiles. *Physica Scripta*, T108:68–71, (2004).

[40] C.H. Skinner, C.A. Gentile, J.C. Hosea, and D. Mueller. Tritium experience in large tokamaks: Application to iter. *Nucl.Fusion*, 39:271–291, (1999).

[41] M. Tokitani, M. Miyamoto, K. Tokunaga, and T. Fujiwara *et.al.* Hydrogen retention properties of co-deposition under high-density plasmas in triam-1m. *J. Nucl. Mater.*, 367–370:1487–1491, (2007).

[42] M. Mayer, V. Rohde, J. Likonen, and E. Vainonen-Ahlgren *et.al.* Carbon erosion and deposition on the asdex upgrade divertor tiles. *J. Nucl. Mater.*, 337–339:119–123, (2005).

[43] C. Martin, M. Richou, W. Saikaily, and B. Pegourie *et.al.* Multiscale study of the porosity of carbon deposits collected in tore supra. *J. Nucl. Mater.*, 363–365:1251–1255, (2007).

[44] V. N. Denisov, L. A. Kuzik, N. Lvova, B. N. Mavrin I. V. Opimach, M. Popov, and W. P. West. Hard diamond-like layers produced during DIII − D tokamak operations. *Physics Letters*, 239(4-5):328–331, (1998).

[45] A. Kirschner, P. Weinhold, V. Philipps, J.P. Coad, A. Huber, U. Samm, and JET EFDA contributors. Modelling of carbon transport in fusion devices: evidence of enhanced re-erosion of in-situ re-depositec carbon. *J. Nucl. Mater.*, 328:62–67, (2004).

[46] G Counsell1, P Coad, C Grisola, and *et.al.* C Hopf. Tritium retention in next step devices and the requirements for mitigation and removal techniques. *Plasma Phys. Control. Fusion*, 48:B189–B199, (2006).

[47] P. Wienhold, H.G. Esser, D. Hildebrandt, and A. Kirschner *et.al.* Investigation of carbon transport in the scrape-off layer of textor-94. *J. Nucl. Mater.*, 290–293:362–366, (2001).

[48] A. Kirschner, S. Brezinsek, H.G. Esser, and A. Huber *et.al.* Modelling of the erosion and re-deposition behaviour in present fusion devices and extrapolations to iter. *30th EPS Conference on Contr. Fusion and Plasma Phys., St. Petersburg.*, 27 A:P–3.196 1–4, (7–11 July 2003).

[49] J.D. Elder, A.G. McLean, P.C. Stangeby, and S.L. Allen *et.al.* OEDGE modeling of the DIII-D H-mode $^{13}CH_4$ puffing experiment. *J. Nucl. Mater.*, 363–365:140–145, (2007).

[50] S.J Tobin, J.T Hogan, C. DeMichelist, and C.C Klepper *et.al.* Global carbon production and transport in ToreSupra. *Plasma Phys. Control. Fusion*, 38:251–263, (1996).

[51] A. Kreter, P. Wienhold, D. Borodin, and S. Brezinsek *et.al.* Study of local carbon transport on graphite, tungsten and molybdenum test limiters in TEXTOR by $^{13}CH_4$ tracer injection. *J. Nucl. Mater.*, 363–365:179–183, (2007).

[52] W. Eckstein. Sputtering, reflection and range values for plasma edge codes. *Rep. IPP 9/117, Max-Planck-Institut für Plasmaphysik, Garching, Germany*, (1998).

[53] W. Eckstein and V. Philipps. Physical sputtering and radiation-enhanced sublimation. *W.O. Hofer, J. Roth eds. Physical processes in the interaction of fusion plasmas with solids (Academic press)*, pages 93–133, (1996).

[54] R. Behrisch. Contribution of the different erosion processes to material release from the vessel walls of fusion devices during plasma operation. *Contrib. Plasma Physics*, 42((2-4)):431–444, (2002).

[55] E. Salonen, K. Nordlund, J. Keinonen, and C. H. Wu. Swift chemical sputtering of amorphous hydrogenated carbon. *Phys. Rev. B*, 63:195415:(1–14), (2001).

[56] K. Nordlund. Atomistic simulation of radiation effects in carbon-based materials and nitrides. *Nucl. Instrum. Meth. B*, 218:9, (2004).

[57] K. Nordlund, E. Salonen, A. V. Krasheninnikov, and J. Keinonen. Swift chemical sputtering of covalently bonded materials. *Pure and Applied Chemistry*, 78:1203–1212, (2006).

[58] J. Marian, L. A. Zepeda-Ruiz, N. Outo, and E. Brings et. al. Formation of ion irradiation induced small-scale defects on graphite surfaces. *J. Appl. Phys.*, 101:044506, (2007).

[59] A.L. Barabasi and H.E. Stanley. Fractal concepts in surface growth. *Press Syndicate of University of Cambridge*, (1995).

[60] L. Sander P. Meakin, P. Ramanlal and R. Ball. Ballistic deposition on surfaces. *Phys. Rev. A*, 36(6):152–164, (1986).

[61] M. Kardar, G. Parisi, and Y. Zhang. Dynamic scaling of growing interfaces. *Phys. Rev. Lett.*, 56(9):889–892, (1986).

[62] Lui Lam. Introduction to nonlinear physics. *Springer-Verlag*, (2003).

[63] Timothy Halpin-Healy and Yi-Cheng Zhang. Kinetic roughening phenomena, stochastic growth, directed polymers and all that. *Physics Reports*, 254:215–414, (1995).

[64] L. Valentini, J. M. Kenny, G. Mariotto, P. Tosi, G. Carlotti, G. Socino, L. Lozzi, and S. Santucci. Structural, morphological, and mechanical properties of plasma deposited hydrogenated amorphous carbon thin films: Ar gas dilution effects. *J. Vac. Sci. Technol. A*, 19(4):1611–1616, (2001).

[65] J. Biener, A. Schenk, B. Winter, C. Lutterloh, U.A. Schubert, and J. Küppers. Spectroscopic identification of c–h species in c:h films using hreels. *Surf. Sci. Lett.*, 291:L725–L729, (1993).

[66] T.M. Burke, R.J. Newport, W.S. Howells, K.W.R. Gilkes, and P.H. Gaskell. The structure of a-c:h(d) by neutron diffraction and isotopic enrichment. *J. Non-Cryst. Solids*, 164–166:1139–1142, (1993).

[67] Liu Dongping, Chen Baoxiang, and Liu Yanhong. The structure of a-c:h(d) by neutron diffraction and isotopic enrichment. *Plasma Sci. Technol.*, 8(3):285–291, (2006).

[68] W. Jacob. Surface reactions during growth and erosion of hydrocarbon films. *Thin Solid Films*, 326:1–42, (1998).

[69] Achim von Keudell. Surface processes during thin-film growth. *Plasma Sources Sci. Tech.*, 9:455–467, (2000).

[70] Wolfgang Jacob, Christian Hopf, Achim von Keudell, Matthias Meier, and Thomas Schwarz-Selinger. Particle-beam experiment to study heterogeneous surface reactions relevant to plasma-assisted thin film growth and etching. *Rev. Sci. Instrum.*, 74(12):5123–5136, (2003).

[71] A. von Keudell, T. Schwarz-Selinger, M. Meier, and W. Jacob. Direct identification of the synergism between methyl radicals and atomic hydrogen during growth of amorphous hydrogenated carbon films. *Appl. Phys. Lett.*, 76(6):676–678, (2000).

[72] Matthias Meier and Achim von Keudell. Hydrogen elimination as a key step for the formation of polymerlike hydrocarbon films. *J. Appl. Phys.*, 90(7):3585–3594, (2001).

[73] Matthias Meier and Achim von Keudel. Temperature dependence of the sticking coefficient of methyl radicals at hydrocarbon film surfaces. *J. Appl. Phys.*, 116(12):5125–5136, (2002).

[74] C. Hopf, A. von Keudell, and W. Jacob. The influence of hydrogen ion bombardment on plasma-assisted hydrocarbon film growth. *Dia. Rel. Mater.*, 12:85–89, (2003).

[75] C. Hopf, A. von Keudell, and W. Jacob. Direct verification of the ion-neutral synergism during hydrocarbon film growth. *J. Appl. Phys.*, 93(6):3352–3358, (2003).

[76] C. Hopf, A. von Keudell, and W. Jacob. Ion-induced surface activation, chemical sputtering, and hydrogen release during plasma-assisted hydrocarbon film growth. *J. Appl. Phys.*, 97:094904–1–6, (2005).

[77] Achim von Keudell. Formation of polymer-like hydrocarbon films from radical beams of methyl and atomic hydrogen. *Thin Solid Films*, 402:1–37, (2002) and references therein.

[78] Y. Miyagawa, H. Nakadate, M. Ikeyama, S. Nakao, and S. Miyagawa. Dynamic mc simulation for a-c:h deposition in methane plasma based on subplantation model. *Diamond Relat. Mater.*, 12:927–930, (2003).

[79] J. Robertson. Diamond-like amorphous carbon. *Mat. Sci. Eng.*, R37:129–281, (2002).

[80] C.C. Battaile, D.J. Srolovitz, and J.E. Butler. Morphologies of diamond films from atomic-scale simulations of chemical vapor deposition. *Diamond Relat. Mater*, 6:1198–1206, (1997).

[81] E.J. Dawnkaski, D. Srivastava, and B.J. Garrison. Time-dependent monte carlo simulations of radical densities and distributions on the diamond 001 (2 × 1) : H surface. *Chem. Phys. Lett.*, 232:524–530, (1995).

[82] E.J. Dawnkaski, D. Srivastava, and B.J. Garrison. Time dependent monte carlo simulations of h reactions on the diamond 001 (2x1) surface under chemical vapor deposition conditions. *J. Chem. Phys.*, 102(23):9401–9411, (1995).

[83] Barbara J. Garrisob, Eric J. Dawnkaski, Deepak Srivastava, and Donald W. Brenner. Molecular dynamics simulations of dimer opening on a diamond 001(2x1) surface. *Science*, 255:835–838, (1992).

[84] D.A. Alman and D.N. Ruzic. Molecular dynamics calculation of carbob/hydrocarbon reflection coefficients on a hydrogenated graphite surface. *J. Nucl. Mater.*, 313-316, (2003).

[85] D.A. Alman and D.N. Ruzic. Molecular dynamics simulation of hydrocarbon reflection and dissociation coefficients from fusion relevant carbon surfaces. *Phys. Scripta.*, T111:145–151, (2004).

[86] E. Neyts, A. Bogaerts, and M. C. M. van de Sanden. Effect of hydrogen on the growth of thin hydrogenated amorphous carbon films from therma energy radicals. *Appl. Phys. Lett.*, 88(141922):1–3, (2006).

[87] Erik Neyts, A. Bogaerts, R. Gijbels, J. Benedikt, and M.C.M. van de Sanden. Molecular dynamics simulations for the growth of diamond-like carbon films from low kinetic energy species. *Diamond Relat. Mater.*, 13:1873–1881, (2004).

[88] E. Neyts, A. Bogaerts, and M.C.M. van de Sanden. Unraveling the deposition mechanism in a-c:h thin-film growth: A molecular-dynamics study for the reaction behavior of c_3 and c_3h radicals with a-c:h surfaces. *J. App. Phys.*, 99(014902):1–8, (2006).

[89] A.R. Sharma, R. Schneider, U. Toussaint, and K. Nordlund. Hydrocarbon radicals interaction with amorphous carbon surfaces. *J. Nucl. Mater.*, 363-365:1283–1288, (2007).

[90] Dominic R. Alfonso and Sergio E. Ulloa. Molecular-dynamics simulations of methyl-radical deposition on diamond (100) surfaces. *Phys. Rev. B*, 48(16):12235–12239, (1993).

[91] P. Träskelin, E. Salonen, K. Nordlund, A.V. Krasheninnikov, J. Keinonen, and C.H. Wu. Molecular dynamics simulations of ch_3 sticking on carbon rst wall structures. *J. Nucl. Mater.*, 313–316:52–55, (2003).

[92] P. Träskelin, E. Salonen, K. Nordlund, J. Keinonen, and C.H. Wu. Molecular dynamics simulations of CH_3 sticking on carbon surfaces, angular and energy dependence. *J. Nucl. Mater.*, 334:65–70, (2004).

[93] D. C. Rapaport. The art of molecular dynamics simulation. *Cambridge university press*, (1995).

[94] D. Frenkel and B. Smit. Understanding molecular simulations: From algorithms to applications. *Academic Press, Computational Science Series, Vol. 1*, (2002).

[95] P. Hohenberg and W. Kohn. Inhomogeneous electron gas. *Phys. Rev.*, 136:B864–B867, (1964).

[96] W. Kohn and L. J. Sham. Self–consistent equations including exchange and correlation effects. *Phys. Rev.*, 140(4A):1133–1138, (1965).

[97] J. Tersoff. New empirical approach for the structure and energy of covalent systems. *Physical Review B*, 37(12):6991–7000, (1988).

[98] G. C. Abell. Empirical chemical pseudopotential theory of molecular and metallic bonding. *Physical Review B*, 31(10):6184–6196, (1985).

[99] D. W. Brenner. Chemical dynamics and bond-order potentials. *Mater. Res. Soc. Bull.*, 21(2):36, (1996).

[100] D. W. Brenner. Empirical potential for hydrocarbons for use in simulating the chemical vapour deposition of diamond films. *Phys. Rev. B*, 42:9458–9471, (1990).

[101] K. Nordlund and J. Keinionen. Formation of ion irradiation induced small-scale defects on graphite surfaces. *Phys. Rev. Lett*, 77(4):699, (1996).

[102] K. Nordlund, J. Keinonen, and T. Mattila. Formation of ion irradiation induced small-scale defects on graphite surfaces. *Phys. Rev. Lett.*, 77:699, (1996).

[103] M. P. Allen and D. J. Tildesley. Computer simulation of liquids. *Oxford science publications*, (1987).

[104] H. J. C. Berendsen, J. P. M. Postma, W. F. Van Gunsteren, A. DiNola, and J. R. Haak. Molecular dynamics with coupling to an external bath. *J. Chem. Phys.*, 81(8):3684–3690, (1984).

[105] W. G. Hoover. Canonical dynamics: Equilibrium phase–space distributions. *Phys. Rev. A*, 31(3):1695–1697, (1985).

[106] H. C. Andersen. Molecular dynamics simulations at constant pressure and/or temperature. *J. Chem. Phys.*, 72(4):2384–2393, (1980).

[107] D.M. Fergusen, J.I. Siepmann, and D.G. Truhlar. Monte carlo methods in chemical physics. *John Wiley and sons*, 105, (1999).

[108] M.E.J. Newman and G.T. Barkema. Monte carlo methods in statistical physics. *Clarendon Press, Oxford*, (2001).

[109] N.G. Kampen. Stochastic processes in physics and chemistry. *Elsevier Science and Technol. Books*, 3, (2007).

[110] C.A. Coulson. The shape and structure of molecules. *Clarendon Press, Oxford*, (1973).

[111] K.A. Fichthorn and W.H. Weinberg. Theoritical foundations of dynamical monte carlo simulations. *J, Chem. Phys.*, 95(2):1090–1096, (1991).

[112] K.A. Fichthorn and W.H. Weinberg. Kinetic monte carlo: Bare bones and a little flesh. *Lecture Notes, University of Illinois*, (2001).

[113] T.R. Waite. Theoretical treatment of kinetics of diffusion-limited reactions. *Phys. Rev.*, 107(2):463–470, (1957).

[114] A. B. Bortz, M. H. Kalos, and J. L. Lebowitz. A new algorithm for monte carlo simulation of ising spin systems. *J. Computational Physics*, 17:10–18, (1975).

[115] E. Vietzke, K. Flaskamp, and V. Philipps. Hydrocarbon formation in the reaction of atomic hydrogen with pyrolytic graphite and the synergistic effect of argon ion bombardment. *J. Nucl. Mater.*, 111–112:763–768, 1982.

[116] C. Hopf, A. von Keudell, and W. Jacob. Chemical sputtering of hydrocarbon films by low-energy Ar^+ ion and H atom impact. *Nucl. Fusion*, 42:L27–L30, (2002).

[117] C. Hopf, A. von Keudell, and W. Jacob. Chemical sputtering of hydrocarbon films. *J. App. Phys.*, 94(4):2373–2380, (2003).

[118] W. Jacob, C. Hopf, and M. Schlüter. Chemical sputtering of carbon materials due to combined bombardment by ions and atomic hydrogen. *Phys. Scripta*, T124:32–36, (2006).

[119] M. Schlüter, C. Hopf, T. Schwarz-Selinger, and W. Jacob. Temperature dependence of the chemical sputtering of amorphous hydrogenated carbon lms by hydrogen. *J. Nucl. Mater.*, 376:33–37, (2008).

[120] J. Roth and J. Bohdansky. Sputtering of graphite with light ions at energies between 20 and 1000 eV. *Nucl. Instrum. Meth. B*, 23:549–551, 1987.

[121] M. Balden and J. Roth. New weight-loss measurements of the chemical erosion yields of carbon materials under hydrogen ion bombardment. *J. Nucl. Mater.*, 280(1):39–44, 2000.

[122] Th. Schwarz-Selinger, A. von Keudell, and W. Jacob. Plasma chemical vapor deposition of hydrocarbon films: The influence of hydrocarbon source gas on the film properties. *J. Appl. Phys.*, 86:3988, (1999).

[123] J.K. Walters and R.J. Newport. The atomic-scale structure of amorphous hydrogenated carbon. *J. Phys.: Condens. Matter*, 7:1755–1769, (1995).

[124] M. Küestner, W. Eckstein, V. Dose, and J. Roth. The influence of surface roughness on the angular dependence of the sputter yield. *Nucl. Instrum. Meth. B*, 145:320–331, (2000).

[125] P. Träskelin, K. Nordlund, and J. Keinonen. He, Ne, Ar-bombardment of carbon first wall structures. *Nucl. Instr. Meth.Phys.Res.B*, 228:319–324, (2005).

[126] W. Jacob. Redeposition of hydrocarbon layers in fusion devices. *J. Nucl. Mater.*, 337–339:839–846, (2005).

[127] Marco A R Alves, Edmundo S Braga, Jaime Frejlich, and Lucila Cescato. An mis diode employing a-c: H film as the insulator. *Vacuum*, 46(12):1461–1463, (1995).

[128] Hsiao chu Tsai and D.B. Bogy. Characterization of diamondlike carbon films and their application as overcoats on thin-film media for magnetic recording. *J. Vac. Sci. Technol. A*, 5(6):3287–3312, (1987).

[129] Lifang Dong, Boqin Ma, and Guoyi Dong. Diamond deposition at low temperature by using ch_4/h_2 gas mixture. *Dia. Rel. Mater.*, 11:1697–1702, (2002).

[130] P. Gupta and E.I. Meletis. Tribological behavior of plasma-enhanced cvd a-c:h lms. part ii: multinanolayers. *Tribology International*, 37:1031–1038, (2004).

[131] G. Cicalaa, P. Brunoa, A. Dragoneb, A.M. Losaccoc, C. Sadund, and A. Generosie. Pecvd a-c:h films for stw resonant devices. *Thin Solid Films*, 482:264–269, (2005).

[132] Thomas Schwarz-Selinger, Christian Hopf, Chao Sun, and Wolfgang Jacob. Growth and erosion of amorphous carbon (a-c:h) lms by low-temperature laboratory plasmas containing h and n mixtures. *J. Nucl. Mater.*, 363–365:174–178, (2007).

[133] Joungchel Lee, R. W. Collins, V. S. Veerasamy, and J. Robertson. Analysis of the ellipsometric spectra of amorphous carbon thin films for evaluation of the sp^3 bonded carbon components. *Dia. Rel. Mater.*, 7:999–1009, (1998).

[134] Kungen Teii. Soft ion impact for surface activation during diamond chemical-vapor deposition on diamond and silicon. *Phys. Rev. B*, 64:125327–1–9, (2001).

[135] A.R. Sharma, R. Schneider, U. Toussaint, and K. Nordlund. Hydrocarbon radicals interaction with amorphous carbon surfaces. *J. Nucl. Mater.*, 363–365:1283–1288, (2007).

[136] A. von Keudell, M. Meier, and C. Hopf. Growth mechanism of amorphous hydrogenated carbon. *Dia. Rel. Mater.*, 11:969–975, (2002).

[137] Z. Huang, Z.Y. Pan, W.J. Zhu, Y.X. Wang, and A.J. Dua. Energy dependence of methyl-radical adsorption on diamond (001)-(2x1) surface. *Surf. Coat. Technol.*, 141:246–251, (2001).

[138] Wolfhard Möller, Wolfgang Fukarek, Klaus Lange, and Achim von Keudell. Mechanisms of the deposition of hydrogenated carbon films. *Jpn. J. Appl. Phys.*, 34:2163–2171, (1995).

[139] M.M. Clark, L.M. Raff, and H.L. Scott. Kintetic monte carlo studies of early surface morphology in diamond film growth by chemical vapor deposition of methyl radical. *Phys. Rev. B*, 54(8):5914–5919, (1996).

[140] H.U. Jäger and A.Yu. Belov. ta-c deposition simulations: Film properties and time-resolved dynamics of film formation. *Phys. Rev. B*, (2003.

[141] Michael Frenklach and Hai Wang.

[142] Karl E. Spear and Michael Frenklach. High temperature chemistry of cvd (chemical vapor deposition) diamond growth. *Pure and Appl. Chem.*, 66(9):1773–1782, (1994).

[143] Y. Miyagawa, S. Nakao, and S. Miyagawa. Dynamic monte carlo simulations of diamond-like carbon film synthesis by ion-assisted deposition. *Surf. Coat. Technol.*, 128-129:85–88, (2000).

[144] A. A. Haasz, P. Franzen, J. W. Davis, S. Chiu, and C. S. Pitcher. Two-region model for hydrogen trapping in and release from graphite. *J. Appl. Phys.*, 77(1):66–86, (1995).

[145] Ahmed. Hassanein. Hydrogen and helium recycling at plasma-facing materials. *NATO science series*, 54, (2001).

[146] M.V. Smoluchowski. *Z. Physik Chem.*, (1917).

[147] Pascale Roubin. Raman spectroscopy and x-ray diffraction studies of some deposited carbon layers in ToreSupra. *J. Nucl. Mater.*, 337-339:990–994, (2005).